Monthly Notices
of the
ROYAL ASTRONOMICAL SOCIETY

Mon. Not. R. Astron. Soc. **418,** 1452–1490 (2011) doi:10.1111/j.1365-2966.2011.19283.x

Near-infrared atlas of S0-Sa galaxies (NIRS0S)

E. Laurikainen,[1,2⋆] H. Salo,[1] R. Buta[3] and J. H. Knapen[4,5]

[1]*Department of Physics/Astronomy Division, University of Oulu, FI-90014, Finland*
[2]*Finnish Centre of Astronomy with ESO (FINCA), University of Turku, Väisäläntie 20, FI-21500 Piikkiö, Finland*
[3]*Department of Physics and Astronomy, University of Alabama, Box 870324, Tuscaloosa, AL 35487, USA*
[4]*Instituto de Astrofísica de Canarias, E-38200 La Laguna, Tenerife, Spain*
[5]*Departamento de Astrofísica, Universidad de La Laguna, E-38205 La Laguna, Tenerife, Spain*

Accepted 2011 June 17. Received 2011 June 16; in original form 2011 April 21

ABSTRACT

We present an atlas of K_s-band images of 206 early-type galaxies, including 160 S0-S0/a galaxies, 12 ellipticals and 33 Sa galaxies (+ one later type). The majority of the atlas galaxies belong to a magnitude-limited ($m_B \leq 12.5$ mag) sample of 185 Near-InfraRed S0 Survey galaxies. To ensure that misclassified S0s are not omitted, 25 ellipticals from the Third Reference Catalogue of Bright Galaxies classified as S0s in the Carnegie Atlas were included in the sample. The observations were carried out using 3–4 m class telescopes with subarcsecond pixel resolution (∼0.25 arcsec), and were obtained in good seeing conditions (full width at half-maximum ∼1 arcsec). The images are 2–3 mag deeper than Two-Micron All-Sky Survey images, allowing the detection of faint outer discs in S0s. Both *visual* and *photometric* classifications are made, largely following the classification criteria of de Vaucouleurs. Special attention is paid to the classification of lenses, which are coded in a more systematic manner than in any of the previous studies. A new lens type, called a 'barlens', is introduced, possibly forming part of the bar itself. Also, boxy/peanut/x-shaped structures are identified in many barred galaxies, even though the galaxies are not seen edge-on, indicating that vertical thickening is not enough to explain these structures. Photometric classification includes detection of exponential outer discs or other structures not directly visible in the images, but becoming clear in unsharp masking or residual images in decompositions. In our photometric classification, nuclear bars are assigned for 15 galaxies, which are overshadowed by bulges in visual classification. The mean Hubble stage in the near-infrared is found to be similar to that in the optical. We give dimensions of structure components, and radial profiles of the position angles and ellipticities, and show deviations from perfect elliptical isophotes. Shells and ripples, generally assumed to be manifestations of recent mergers, are detected only in six galaxies. However, multiple lenses appear in as much as 25 per cent of the atlas galaxies, which is a challenge to the hierarchical evolutionary picture of galaxies. Such models need to explain how the lenses were formed and then survived in multiple merger events that galaxies may have suffered during their lifetimes.

Key words: galaxies: elliptical and lenticular, cD – galaxies: evolution – galaxies: structure.

1 INTRODUCTION

In the early classification by Hubble (1936), the S0s were an enigmatic group of galaxies between the ellipticals and the early-type spirals, and since then they have been subject to many kinds of interpretations. The classification of S0s depends on recognizing the presence of a disc, but having no spiral arms. The interface between E and S0 galaxies was somewhat obscured by the detection of boxy and discy ellipticals (Bender 1988), based on deviations of the outer isophotes from simple elliptical shape. Earlier, kinematic observations by Dressler & Sandage (1983) had already shown that the lower luminosity ellipticals are more rotationally supported than the bright ellipticals. Bender et al. (1989) then discovered that both galaxy luminosity and the degree of rotational support correlate with the isophotal shapes of the elliptical galaxies. A similar sequence of increasing dominance of rotational support towards the lower luminosity galaxies was also found for the S0s (Dressler & Sandage

⋆E-mail: eija.laurikainen@oulu.fi

1983). However, as the amount of rotation is significantly larger in S0s, this kinematically links the S0s to the spiral galaxies. All this caused some early-type galaxy observers to question the morphological classification of S0s, an attitude which culminated in 1990 when King (1992) and Djorgovski et al. (1992) announced that the Hubble sequence was breaking down, and should be replaced by a classification based on measured physical parameters. Despite the early discovery of S0s, new kinematic observations have put them once again at the forefront of research. Recent IFU kinematic observations by Emsellem at al. (2007) have shown that the fast rotators are morphologically assigned to a mix of E and S0 galaxies, which leads to further questions about the meaning of their morphological classification.

On the other hand, there are morphological structures in S0s which can be connected successfully to real dynamical processes. Inner, outer and nuclear rings can be either bar-induced resonance rings or accretion rings related to the accumulation of external gas into the galactic discs (see the review by Buta 2011). Recently, new theories of ring formation have also been presented, like the 'manifold orbits' emanating from Lagrangian points in barred potentials (Romero-Gómez et al. 2006; Athanassoula et al. 2010). Merger-built structures, such as shells, ripples (Malin & Carter 1980) and polar rings (Schweizer, Whitmore & Rubin 1983; in 2 per cent of S0s), appear in S0 galaxies, but they are not very common. The first attempt to include bar morphology, for example, boxy, peanut or x-shaped structures, into galaxy classification was made by Buta et al. (2010). Bar morphology is an important characteristic of galaxy morphology, which in theoretical models has been associated with the secular dynamical evolution of galaxies (Athanassoula & Misioritis 2002; Athanassoula 2003).

Lenses formed part of the early classification scheme of S0s (Sandage 1962; Sandage & Tammann 1981), but were not initially assigned any classification symbols. Inner and outer lenses in barred S0s were discussed by Kormendy (1979), and Laurikainen et al. (2009) showed that a large majority of S0s, both barred and non-barred, have lenses. Moreover, some S0s have complicated multilens systems, which have not yet been theoretically explained. Overall, the origin of lenses is not well understood: they can form as part of the disc formation process (Bosma 1983) or be triggered by bars (Kormendy 1979) or by the accretion of small companions. In fact, lenses and other fine-structures of S0s might be important imprints of possible secular evolution of galaxies. The only major galaxy atlas that recognizes lenses in the classification is the de Vaucouleurs atlas of galaxies (Buta, Corwin & Odewahn 2007, hereinafter dVA).

In this paper, we present the Near-InfraRed S0 Survey (NIRS0S) atlas in the K_s band and use it for detailed morphological classification. To our knowledge, this is the first attempt of detailed classification of S0s using deep near-infrared (near-IR) images. The 2.2 μm wavelength used traces the old stellar population of galaxies and is relatively free of internal extinction, which makes it ideal for the classification of structures. The sample was selected from the Third Reference Catalogue of Bright Galaxies (RC3; de Vaucouleurs et al. 1991). In order to study the interfaces of S0s with ellipticals and spirals, Sa galaxies in the RC3 and those ellipticals classified as S0s in the Revised Shapley-Ames Catalogue of Bright Galaxies (RSA; Sandage & Tammann 1981) were also included in the sample. Our images are several magnitudes deeper than the images in the Two-Micron All-Sky Survey (2MASS; Skrutskie et al. 2006), which was the largest near-IR survey carried out previously. Two large mid-IR galaxy surveys using the *Spitzer Space Telescope* are the Spitzer Infrared Nearby Galaxies Survey (SINGS; Kennicutt 2003) and the Local Volume Legacy project (Kennicutt 2007), both providing deep images at 3.6 μm. However, these surveys contain only a few S0s. A more comprehensive nearby galaxy survey is the Spitzer Survey of Stellar Structure in Galaxies (S^4G; Sheth et al. 2010), which consists of 2331 nearby galaxies. This survey exceeds the image depth of the NIRS0S, but the NIRS0S is more complete in respect of the S0s, and the pixel resolution is higher than in the S^4G.

The NIRS0S atlas consists of images of 206 galaxies, a sample which, after our revised classification, has 12 ellipticals, 160 S0-S0/a and 33 Sa galaxies. Section 2 describes the sample and observations, data reductions are explained in Section 3, and the image atlas is given in Section 4. Visual and photometric classifications are presented, starting from the de Vaucouleurs (1959) classification criteria, but going beyond that in classifying the details of structures (Section 5). The dimensions of the structure components are given in Section 6, and the radial profiles of the position angles (PAs), ellipticities and parameter $b4$, describing deviations from perfect ellipticity of the isophotal contours, are shown in the atlas (see Fig. 5 shown later). In this paper, the atlas image is presented, whereas the number statistics and more thorough discussion of the structure components will appear in forthcoming papers.

We find that multiple lenses are common in S0s, appearing even in 25 per cent of the atlas galaxies. However, shells or ripples were detected only in six galaxies. Of the 25 RC3 ellipticals in our original sample, seven were re-classified as S0s by us. Bars and bulges in subsamples of the NIRS0S have been previously discussed by Laurikainen, Salo & Buta (2005), Laurikainen et al. (2006, 2007, 2009) and Buta et al. (2006), the properties of bulges by Laurikainen et al. (2010) and the distribution of bar strengths by Buta et al. (2010).

2 SAMPLE AND OBSERVATIONS

We have carried out a large, magnitude-limited imaging survey, the NIRS0S in the nearby Universe. The sample selection criteria are as follows: morphological type $-3 \leq T \leq 1$, total magnitude of $B_T \leq 12.5$ mag and inclination less than 65°. Applying these criteria to the RC3, and also including 25 ellipticals (indluding late-types E^+) classified as S0s in the RSA, yields a sample of 185 galaxies (marked with an asterisk in Table 3 given later).[1] These ellipticals were included, in order not to miss any potentially misclassified S0s. The sample includes 30 additional galaxies not fulfilling the original selection criteria, mostly S0-Sa galaxies which slightly exceed the magnitude limit or in some cases the inclination limit. These galaxies were observed when it was not possible to observe the primary targets, due to either unsuitable wind direction or no primary targets were visible. Including these galaxies yields a sample of 215 galaxies. In total, after our re-classifications, the full sample includes 13 ellipticals, 139 S0s, 30 S0/a galaxies, 33 Sa galaxies and one later-type spiral. The selection criteria in our magnitude-limited NIRS0S sample are similar to those in the Ohio State University Bright Spiral Galaxy Survey (Eskridge et al. 2002), but going half a magnitude deeper.

The observations were carried out during the period 2003–09 using various ground-based telescopes in the two hemispheres, with

[1] Our current NIRS0S sample differs from that specified by Laurikainen et al. (2005) and Buta et al. (2006) in that we use B_T or the photographic value m_B or the average of these two when both are available. This was done to eliminate contamination of the original sample by total V magnitudes in the RC3, which occupy the same column as B_T in that catalogue.

Table 1. The observing campaigns.

Telescope+instrument	Date	Resolution (arcsec pixel^{-1})	FOV (arcmin)
Near-IR			
NOT(2.5 m)/NOTCam	2003 January 17–20	0.233	4.0 × 4.0
NOT(2.5 m)/NOTCam	2003 September 28 and 29	0.233	4.0 × 4.0
NOT(2.5 m)/NOTCam	2004 January 8–11	0.233	4.0 × 4.0
NTT(3.6 m)/SOFI	2004 December 20–23	0.288	4.9 × 4.9
NOT(2.5 m)/NOTCam	2005 May 19–23	0.233	4.0 × 4.0
WHT(4.2 m)/LIRIS	2006 May 11 and 14	0.250	4.3 × 4.3
NTT(3.6 m)/SOFI	2006 July 17–21	0.288	4.9 × 4.9
WHT(4.2 m)/LIRIS	2007 March 3–5	0.250	4.3 × 4.3
CTIO(4 m)	2007 October 27–29	0.306	5.2 × 5.2
TNG(3.6 m)/NICS	2007 November 17–19	0.252	4.2 × 4.2
TNG(3.6 m)/NICS	2008 June 16 and 17	0.252	4.2 × 4.2
NTT(3.6 m)/SOFI	2008 June 10–14	0.288	4.9 × 4.9
WHT(4.2 m)/LIRIS	2008 December 2 and 3	0.250	4.3 × 4.3
TNG(3.6 m)/NICS	2009 April 10–12	0.252	4.2 × 4.2
KPNO(2.1 m)/FLMN	2009 May 4–7	0.606	19.5 × 19.5

sizes between 2.5 and 4.2 m. The observing campaigns are shown in Table 1, listing the pixel scale and field of view (FOV) of the telescope/instrument setup used. The telescopes used were the 2.5-m Nordic Optical telescope (NOT, La Palma) using NOTCam, the 3.6 m New Technology Telescope [NTT, European Southern Observatory (ESO)] using SOFI, the 4.2-m William Herschel Telescope (WHT, La Palma) using LIRIS, the 3.6-m Telescopio Nazionale Galileo (TNG, La Palma) using NICS, the 2.1-m telescope at the Kitt Peak National Observatory using Flamingos and the 4-m telescope at the Cerro Tololo Inter-American Observatory (CTIO, Chile). Most of the galaxies fitted in the typical 4–5 arcmin FOV, whereas for the largest galaxies the 19.5 arcmin FOV of Flamingos was used. The total on-source integration time was 1800–2400 s, taken in exposures of 3–30 s, depending on the galaxy brightness and telescope/instrument setup. Owing to the high sky brightness in the near-IR, and because the galaxies typically occupied a large fraction of the FOV, an equal amount of time was spent on the target and on the sky. The target and the sky fields were alternated after every 1–2 min using a dithering box of 20 arcsec for the target. Either sky or dome flat-fields were obtained, depending on what was recommended at each telescope. The seeing conditions were generally good (see Table 2), the full width at half-maximum (FWHM) being typically around 1 arcsec. Seeing was worst at the KPNO (for 10 galaxies) where the FWHM was between 2 and 3 arcsec, whereas at the NTT the FWHM was below 1 arcsec for most of the time (57 galaxies). As the flux calibrations were done using 2MASS images, flux calibration standards were observed only occasionally.

In total, 206 galaxies were observed, including 172 galaxies of the magnitude-limited sample of 185 galaxies. Of the non-observed 13 galaxies, ESO 137−34 is most probably a distant galaxy having two bright stars in the field. Two of the late-type ellipticals (NGC 147 and 185) appeared to be dwarf galaxies, and NGC 404 could not be observed due to the bright star in the immediate vicinity of the galaxy. NGC 205, 1808 and 5128 were too large to be observed with our typical FOV, and at Kitt Peak these galaxies were not visible during the period when time was allocated. IC 5250/5250A is an advanced merger and therefore not useful for our analysis. Four of the galaxies, NGC 1291, 1316, 1546 and 1947, were not observed because of a lack of observing time. However, for NGC 1291 and 1316, SINGS images at 3.6 μm are available (Kennicutt 2003). In conclusion, in our magnitude-limited sample, there are only five galaxies of interest (NGC 205, 1808, 5128, 1546 and 1947) for which we lack near-IR observations. Of these, NGC 205 is a low surface brightness galaxy, most probably an S0 with a central lens. NGC 1808 is a dusty Sa-type spiral, whereas NGC 5128, 1546 and 1947 have strong dust lanes in a nearly featureless spheroidal component and are classified as $T = -2, -1$ and -3, respectively. Of the S0-S0/a galaxies in the magnitude-limited sample, observations for only four galaxies are missing, which means that the completeness of our observations is 98 per cent.

3 DATA REDUCTION

3.1 Combining the images

The images were combined using IRAF routines.[2] The main reduction steps consisted of subtracting the sky from each science image, flat-fielding the difference image, combining the images after correcting the shifts between the images and fine-tuning the sky subtraction. The sky images taken immediately before and after the target observation generally worked best for the sky subtraction. For flat-fielding, normalized master flat-fields were used, made as an average of the differences between high- and low-ADU-level images (ADU = digital counts). In the dome flats obtained at the NTT, scattered light sometimes produced a shade pattern which was corrected using the correction frames offered by the ESO. While combining the images a 3σ clipping factor was used to reduce the noise. The images obtained at the WHT, TNG and NTT showed 'crosstalk', appearing as vertical or horizontal stripes in the images. For the ES0/NTT images, the script crosstalk.cl (available at the ESO) corrected the stripes effectively. For the WHT images, this problem was more severe, and the stripes were corrected manually using the IRAF routines IMCOPY and BACKGROUND. For some of the galaxies, bad lines/columns and sky gradients were also corrected. Foreground stars were removed using the DAOPHOT package in IRAF, and the cleaning was completed with the IMEDIT routine. The images were transposed to have north up and west to the right.

[2] IRAF is distributed by the National Optical Astronomy Observatories, which are operated by AURA, Inc., under cooperative agreement with the National Science Foundation.

Table 2. The image quality. Galaxy identifications and telescopes are indicated, together with FWHM and estimated 1σ sky variation ($\sigma_{\rm sky}$). $\Delta\mu_0$ indicates the difference between the zero-points derived for the galaxy based on 2MASS m_{14}, with respect to the campaign mean for the same airmass, and Δk_{20} and $\Delta k_{\rm ext}$ indicate the differences between the measured isophotal magnitudes with respect to 2MASS values.

Galaxy	Telescope	FWHM (arcsec)	$\sigma_{\rm sky}$ (mag arcsec^{-2})	$\Delta\mu_0$ (mag)	Δk_{20} (mag)	$\Delta k_{\rm ext}$ (mag)
(1)	(2)	(3)	(4)	(5)	(6)	(7)
ESO 137−10	NTT	1.25	22.7	0.06	−0.13	−0.15
ESO 337−10	NTT	0.89	22.2	−0.00	−0.02	0.00
ESO 208−21	NTT	0.63	22.2	0.11	−0.03	−0.04
IC 1392	TNG	0.97	22.9	−0.06	−0.04	−0.03
IC 4214	NTT	0.84	21.9	−0.02	−0.02	0.01
IC 4329	NTT	0.79	22.4	−0.01	−0.02	−0.00
IC 4889	CTIO	0.83	21.9	−0.01	0.00	0.03
IC 4991	NTT	0.75	21.9	0.22	−0.08	−0.06
IC 5240	NTT	1.15	22.3	0.14	−0.10	−0.13
IC 5267	CTIO	1.00	21.7	0.06	0.02	0.15
IC 5328	NTT	1.06	23.3	−0.14	−0.05	−0.02
NGC 0439	NTT	0.80	22.6	0.06	0.03	0.12
NGC 0474	CTIO	1.01	21.9	0.01	−0.02	0.08
NGC 0484	NTT	0.72	22.0	−0.00	−0.04	−0.04
NGC 0507	NOT	0.88	21.2	−0.15	0.03	0.07
NGC 0524	NOT	1.16	21.2	−0.14	−0.03	−0.05
NGC 0584	NTT	0.78	21.8	−0.03	−0.04	−0.08
NGC 0718	NOT	1.05	21.5	0.07	0.00	0.04
NGC 0890	NOT	0.82	22.1	0.00	−0.04	−0.05
NGC 0936	NOT	1.26	21.9	−0.02	−0.03	−0.10
NGC 1022	NOT	1.86	21.5	0.06	0.02	0.02
NGC 1079	NTT	0.83	22.2	0.00	−0.05	−0.08
NGC 1161[a]	NOT	0.82	21.4			
NGC 1201	NOT	1.06	21.0	0.06	0.00	−0.00
NGC 1302	NOT	1.16	21.2	0.01	−0.07	−0.06
NGC 1317	NTT	0.67	22.1	0.00	−0.03	−0.05
NGC 1326	NTT	0.72	22.0	−0.00	−0.05	−0.03
NGC 1344	CTIO	0.99	22.1	−0.02	0.03	0.14
NGC 1350	NTT	0.75	22.5	0.13	0.01	0.10
NGC 1351	NTT	0.89	22.3	−0.06	0.05	0.11
NGC 1371	CTIO	1.03	22.0	−0.01	0.00	0.00
NGC 1380	CTIO	1.14	22.0	0.00	−0.01	0.07
NGC 1387	NTT	0.69	21.8	0.01	0.02	0.02
NGC 1389	CTIO	1.08	22.0	−0.01	0.00	0.05
NGC 1400	NOT	1.07	21.7	−0.01	−0.00	0.03
NGC 1411	NTT	0.81	22.2	0.02	−0.00	−0.01
NGC 1415	NOT	1.05	21.5	0.07	0.00	0.00
NGC 1440	NOT	1.00	21.7	−0.06	0.00	0.01
NGC 1452	NOT	1.05	21.8	−0.04	−0.01	0.02
NGC 1512	NTT	0.63	22.2	−0.02	−0.13	−0.10
NGC 1533	NTT	0.70	22.2	0.01	−0.00	−0.03
NGC 1537	CTIO	0.98	21.8	0.03	−0.04	0.01
NGC 1543	CTIO	1.17	21.9	0.01	0.04	0.18
NGC 1553	NTT	1.01	22.7	0.01	0.02	0.07
NGC 1574	NTT	0.75	21.8	−0.00	0.01	0.04
NGC 1617	CTIO	1.01	22.0	−0.04	−0.04	−0.05
NGC 2196	NOT	1.40	21.4	0.00	0.00	−0.00
NGC 2217	NOT	1.23	21.2	−0.05	0.04	0.04
NGC 2273	NOT	1.33	21.9	−0.04	−0.02	0.00
NGC 2292[b]	TNG	1.39	22.5			
NGC 2293[b]	TNG	1.39	22.5			
NGC 2300	TNG	1.92	22.7	−0.01	0.03	0.06
NGC 2380	TNG	1.31	22.6	−0.06	0.03	0.08
NGC 2460	NOT	1.00	21.7	0.04	−0.01	−0.01
NGC 2523	NOT	1.14	21.9	−0.04	−0.13	−0.09
NGC 2549	NOT	1.00	21.2	−0.07	−0.02	−0.00
NGC 2655	TNG	1.16	22.6	−0.03	−0.03	−0.04

Table 2 – *continued*

Galaxy	Telescope	FWHM (arcsec)	σ_{sky} (mag arcsec^{-2})	$\Delta\mu_0$ (mag)	Δk_{20} (mag)	Δk_{ext} (mag)
(1)	(2)	(3)	(4)	(5)	(6)	(7)
NGC 2681	NOT	1.15	21.8	0.01	0.04	0.03
NGC 2685	WHT	0.62	22.4	0.02	−0.07	−0.03
NGC 2768	WHT	0.90	22.7	0.01	−0.09	−0.22
NGC 2781	NOT	0.91	21.8	−0.01	−0.02	−0.04
NGC 2782	WHT	1.12	22.7	−0.09	0.01	0.04
NGC 2787	NOT	1.10	21.3	0.05	−0.02	−0.02
NGC 2855	NOT	0.93	21.7	0.01	−0.03	−0.00
NGC 2859	NOT	0.93	21.7	−0.03	−0.03	0.13
NGC 2880	WHT	0.93	22.9	−0.06	0.03	0.07
NGC 2902	WHT	1.12	22.8	0.14	0.01	0.04
NGC 2911	NOT	0.79	21.0	0.05	0.01	0.04
NGC 2950	NOT	0.98	21.4	−0.02	−0.03	−0.01
NGC 2983	NOT	0.98	21.7	−0.03	−0.03	0.00
NGC 3032	WHT	1.00	23.6	−0.01	0.02	0.05
NGC 3081	NTT	0.63	22.0	−0.00	−0.02	−0.06
NGC 3100J	NTT	0.83	23.0		−0.08	−0.14
NGC 3166	WHT	1.00	22.8	−0.01	−0.02	−0.03
NGC 3169	WHT	1.08	23.1	−0.03	0.01	0.00
NGC 3226[b]	KPNO	2.12	23.0			
NGC 3227[b]	KPNO	2.12	23.0			
NGC 3245	WHT	1.12	22.6	−0.00	−0.01	−0.03
NGC 3358	NTT	0.69	21.8	0.00	−0.04	0.06
NGC 3384	WHT	0.55	23.1	0.02	−0.03	−0.06
NGC 3412	TNG	1.89	22.7	0.04	0.09	0.09
NGC 3414	WHT	0.88	22.3	0.00	0.01	0.03
NGC 3489	WHT	1.25	23.2	0.01	−0.04	−0.06
NGC 3516	NOT	0.91	22.1	−0.05	−0.05	−0.01
NGC 3607	WHT	1.20	22.7	0.11	0.02	−0.03
NGC 3619	KPNO	2.06	21.4	0.03	0.10	0.14
NGC 3626	NOT	0.84	21.8	0.05	0.04	0.07
NGC 3665	NOT	1.12	22.0	0.00	−0.02	0.00
NGC 3706	NTT	0.81	22.2	−0.03	−0.03	0.01
NGC 3718	TNG	1.13	23.2	0.01	0.05	0.08
NGC 3729	NOT	1.33	21.7	0.03	0.00	0.16
NGC 3892	NTT	1.29	22.4	0.03	0.02	0.03
NGC 3900	NOT	0.91	22.3	−0.00	−0.01	−0.01
NGC 3941	NOT	0.89	21.8	−0.01	0.03	0.05
NGC 3945	WHT	1.08	22.9	−0.04	−0.04	−0.07
NGC 3998	WHT	1.02	23.0	−0.03	−0.00	0.00
NGC 4073	TNG	1.46	22.7	−0.03	−0.02	0.02
NGC 4105[b]	NTT	1.12	22.5			
NGC 4106[b]	NTT	1.12	22.5			
NGC 4138	NOT	1.04	21.4	−0.00	−0.01	0.01
NGC 4143	TNG	1.15	23.1	0.04	−0.01	−0.02
NGC 4150	WHT	1.12	23.1	−0.01	0.13	0.17
NGC 4203	WHT	1.33	22.8	−0.02	−0.03	−0.06
NGC 4220	WHT	1.05	22.7	0.02	−0.02	−0.05
NGC 4245	WHT	1.00	23.1	0.00	−0.02	−0.01
NGC 4262	WHT	0.88	22.9	0.01	−0.04	−0.05
NGC 4267	TNG	0.89	23.2	−0.00	−0.02	−0.01
NGC 4281	TNG	1.13	22.8	−0.04	−0.02	−0.03
NGC 4293	WHT	1.52	22.6	−0.03	−0.05	0.01
NGC 4314	WHT	0.82	22.8	−0.03	−0.07	−0.07
NGC 4339	TNG	1.51	22.9	−0.01	0.02	0.05
NGC 4340	NOT	1.05	21.3	0.12	0.02	0.03
NGC 4350	TNG	1.13	22.7	−0.01	0.02	0.05
NGC 4369	NOT	1.05	21.5	−0.11	0.01	0.03
NGC 4371	TNG	1.10	23.4	−0.02	−0.00	0.01
NGC 4373	NTT	1.17	22.3	0.08	−0.07	0.02
NGC 4378	NTT	1.17	22.5	−0.10	−0.01	0.01
NGC 4382	KPNO	1.58	21.3	0.02	0.13	0.22

Table 2 – *continued*

Galaxy	Telescope	FWHM (arcsec)	σ_{sky} (mag arcsec^{-2})	$\Delta\mu_0$ (mag)	Δk_{20} (mag)	Δk_{ext} (mag)
(1)	(2)	(3)	(4)	(5)	(6)	(7)
NGC 4406	KPNO	1.70	21.0	0.02	0.14	0.40
NGC 4424	WHT	1.52	22.4	0.03	0.01	0.04
NGC 4429	WHT	1.17	22.5	0.03	−0.02	−0.02
NGC 4435	WHT	1.62	22.9	−0.01	−0.29	−0.38
NGC 4457	WHT	1.40	22.5	−0.03	−0.04	−0.02
NGC 4459	WHT	0.68	23.0	−0.01	−0.09	−0.09
NGC 4472	KPNO	2.30	21.2	0.04	0.15	0.32
NGC 4474[c]	TNG	1.36	22.1			
NGC 4477	WHT	1.00	23.5	−0.02	0.02	0.04
NGC 4503	TNG	1.26	22.6	0.06	0.01	0.00
NGC 4531	WHT	1.50	22.2	0.02	−0.04	−0.05
NGC 4546	WHT	1.00	23.5	−0.01	−0.01	−0.00
NGC 4552	KPNO	2.12	21.2	0.04	0.13	0.29
NGC 4578	TNG	1.26	22.8	0.01	−0.04	−0.03
NGC 4596	WHT	1.00	22.9	0.02	0.02	0.07
NGC 4608	NOT	1.12	21.8	−0.21	0.02	0.10
NGC 4612	TNG	0.98	23.4	0.01	−0.01	−0.01
NGC 4638	TNG	2.39	22.9	0.02	0.07	0.11
NGC 4643	NOT	0.98	21.5	0.03	−0.03	−0.00
NGC 4649	KPNO	2.12	21.5	0.01	0.14	0.29
NGC 4665	TNG	2.02	23.0	0.02	0.09	0.15
NGC 4691	TNG	1.59	22.9	0.01	0.01	0.06
NGC 4694	WHT	0.97	22.8	−0.02	−0.08	−0.09
NGC 4696	NTT	1.14	22.6	−0.25	−0.01	0.03
NGC 4754	WHT	1.25	22.6	0.01	0.03	−0.03
NGC 4772	WHT	1.55	22.7	0.01	−0.02	0.03
NGC 4880	WHT	1.29	22.7	0.01	−0.09	−0.21
NGC 4914	TNG	1.39	22.6	−0.01	−0.07	−0.07
NGC 4976	NTT	1.02	22.0	0.03	0.06	0.18
NGC 4984	NOT	1.51	21.5	0.06	0.01	−0.01
NGC 5026	NTT	0.83	21.9	0.02	−0.02	0.01
NGC 5078	KPNO	1.82	21.0	−0.00	0.04	0.09
NGC 5087	NTT	1.06	22.5	0.04	−0.01	0.03
NGC 5101	AAT	1.39	20.4		0.02	0.04
NGC 5121	NTT	0.86	22.6	0.00	−0.02	−0.02
NGC 5206	NTT	0.89	22.1	0.05	−0.00	0.16
NGC 5266	NTT	1.03	22.5	0.03	−0.02	−0.01
NGC 5273	TNG	1.49	23.1	0.06	0.01	−0.01
NGC 5308	WHT	1.00	22.5	0.03	−0.03	−0.04
NGC 5333	NTT	0.37	22.1	−0.05	−0.05	−0.05
NGC 5353[b]	TNG	1.26	23.2			
NGC 5354[b]	TNG	1.26	23.2			
NGC 5365	NTT	0.66	22.2	−0.05	0.02	0.12
NGC 5377	TNG	1.18	23.2	−0.00	0.00	0.00
NGC 5419	NTT	1.02	22.3	−0.10	−0.04	−0.02
NGC 5448	WHT	0.95	22.8	−0.02	0.00	−0.01
NGC 5473	NOT	0.82	21.6	−0.14	0.00	0.00
NGC 5485	NOT	0.93	21.5	−0.01	−0.04	−0.04
NGC 5493	WHT	1.36	22.4	−0.00	0.00	0.01
NGC 5631	NOT	0.82	21.9	0.10	0.00	0.00
NGC 5638[b]	WHT	0.80	23.1			
NGC 5701	TNG	1.13	23.2	0.00	−0.06	−0.06
NGC 5728	NTT	0.95	21.8	0.09	−0.04	0.01
NGC 5750	NTT	0.72	22.2	−0.02	−0.04	−0.09
NGC 5838	WHT	1.62	22.8	−0.01	−0.03	−0.02
NGC 5846	NTT	0.72	20.6	0.41	−0.23	−0.36
NGC 5898	NTT	0.81	22.2	−0.06	−0.01	0.03
NGC 5953	WHT	1.12	22.7	0.02	0.01	0.23
NGC 5982	NOT	0.82	21.7	−0.05	−0.13	−0.17
NGC 6012	KPNO	2.42	21.4	−0.06	0.03	0.11
NGC 6340	NOT	0.72	21.6	0.06	0.13	0.23

Table 2 – *continued*

Galaxy	Telescope	FWHM (arcsec)	$\sigma_{\rm sky}$ (mag arcsec^{-2})	$\Delta\mu_0$ (mag)	Δk_{20} (mag)	$\Delta k_{\rm ext}$ (mag)
(1)	(2)	(3)	(4)	(5)	(6)	(7)
NGC 6407	NTT	0.66	22.2	−0.04	−0.00	0.02
NGC 6438[b]	NTT	1.44	22.4			
NGC 6482	KPNO	1.39	21.2	0.01	0.13	0.19
NGC 6646	NOT	0.82	21.9	0.23	0.04	0.08
NGC 6654	NOT	1.00	21.8	0.06	0.11	0.17
NGC 6684	NTT	0.81	22.2	−0.05	−0.11	−0.12
NGC 6703	NOT	1.10	22.0	−0.11	0.06	0.11
NGC 6782	NTT	0.63	22.3	−0.05	−0.05	−0.06
NGC 6861	NTT	0.66	22.4	−0.05	−0.03	−0.00
NGC 6958	CTIO	0.91	22.0	−0.03	0.01	0.06
NGC 7029	NTT	0.69	22.4	−0.07	−0.07	−0.05
NGC 7049	NTT	0.72	22.4	0.06	−0.01	0.07
NGC 7079	NTT	0.66	22.4	−0.07	−0.04	−0.09
NGC 7098	NTT	0.84	21.7	0.01	−0.21	−0.22
NGC 7192	NTT	0.81	22.1	−0.05	0.06	0.11
NGC 7213	NTT	0.75	22.3	−0.03	−0.05	−0.06
NGC 7217	KPNO	2.42	21.2	−0.01	0.13	0.18
NGC 7332	WHT	1.00	22.9	−0.02	−0.02	−0.03
NGC 7339	WHT	0.95	22.1	−0.00	−0.04	−0.05
NGC 7371	NTT	0.60	22.3	−0.05	0.04	0.06
NGC 7377	NOT	0.91	21.0	−0.04	0.00	0.02
NGC 7457	WHT	0.93	22.6	−0.01	−0.06	−0.07
NGC 7585	NTT	1.11	22.7	0.05	0.07	0.15
NGC 7727	NTT	0.90	22.8	0.01	−0.01	0.06
NGC 7742	NOT	0.77	21.1	0.03	−0.01	0.01
NGC 7743	NOT	0.82	20.9	0.24	0.09	0.08
NGC 7796	NTT	0.72	22.3	−0.05	−0.01	0.02

[a]2MASS data missing – use the campaign zero-point.
[b]Interacting – use the campaign zero-point.
[c]2MASS data inconsistent – use the campaign zero-point.

3.2 Flux calibrations

Flux calibrations were done using the $K_{\rm s}$ aperture photometry of galaxies given in the 2MASS.[3] We write

$$\mu = -2.5\log_{10} F/{\rm pix}^2 + \mu_0,$$

where μ is the surface brightness in units of mag arcsec^{-2}, F is the flux in digital units (normalized to 1 s), 'pix' is the pixel size in arcsec and μ_0 is the magnitude zero-point. After sky background subtraction and removal of foreground stars, the total flux within a 14-arcsec (diameter) circular aperture around the galaxy centre was measured and compared to the corresponding 2MASS aperture magnitude, m_{14}, available via the NED. The zero-point μ_0 was calculated from the equation

$$\mu_0 = m_{14} + 2.5\log_{10}\left(\sum_{r_i<7\,{\rm arcsec}} F_i\right),$$

where r_i is the distance from the galaxy centre. In the calculation of the total flux inside the aperture, bilinear interpolation was used for the pixels falling on the aperture border. Also, the images were first degraded to have the same seeing as the 2MASS images, to compensate for the possible leaking of light in the original 2MASS aperture measurements. We thus applied a convolution with a Gaussian point spread function with

$${\rm FWHM_{conv}} = \sqrt{(2.5\,{\rm arcsec})^2 - {\rm FWHM}^2},$$

where FWHM corresponds to the original NIRS0S image, and 2.5 arcsec is the typical value for 2MASS images. In practice, the uncertainties in the photometric zero-point due to sky subtraction, centring of the aperture or the applied bilinear interpolation are all negligible (<0.001 mag). Likewise, the effect of different FWHMs is quite small (<0.02 mag), and thus the formal error of our zero-points corresponds to the accuracy of the 2MASS absolute calibration, ∼2–3 per cent (Jarrett et al. 2000).

As an additional check, and to minimize possible human errors (e.g. use of wrong image, wrong centring, wrong pixel size, etc.), we also used the 2MASS k_{20} and $k_{\rm ext}$ magnitudes to check the consistency of our zero-point calibration. These quantities were loaded from NASA/IPAC Infrared Science Archive (IRSA) via GATOR: k_{20} is the total magnitude inside a $\mu_k = 20$ mag isophotal ellipse and $k_{\rm ext}$ is the extrapolated total magnitude. The IRSA lists the isophotal radius a_{k20}, PA ϕ_{k20}, axial ratio $(b/a)_{k20}$ and the radius $r_{\rm ext}$ corresponding to $k_{\rm ext}$ (isophotal orientation and shape are the same as for k_{20}).

Fig. 1 displays a typical example of flux calibration (similar plots for all galaxies are available at the NIRS0S website[4]), displaying the

[3] 2MASS is a joint project of the University of Massachusetts and the Infrared Processing and Analysis Center/California Institute of Technology, funded by the National Aeronautics and Space Administration and the National Science Foundation.

[4] http://www.oulu.fi/astronomy/NIRS0S_pub/Kcalibration.html

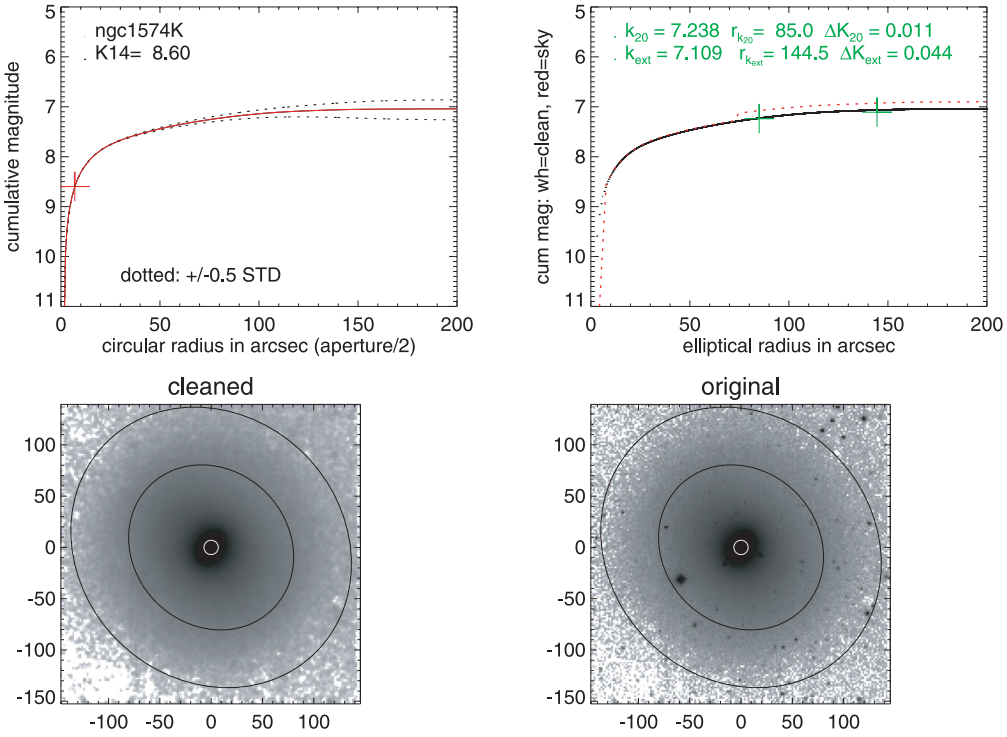

Figure 1. Example of zero-point calibration based on the 2MASS 14-arcsec circular aperture magnitude m_{14}. In the upper row, circular and elliptical isophote cumulative magnitudes are shown, while the lower row displays the original image (right-hand panel) and the cleaned image convolved to FWHM = 2.5 arcsec (left-hand panel). The circular aperture growth curve is adjusted to go through m_{14} at $r = 7$ arcsec. The dotted lines indicate the effect of adjusting the sky background by ± 0.5 times the sky rms variation, being completely negligible on the derived μ_0. The two crosses on the elliptical aperture growth curve mark the 2MASS k_{20} and $k_{\rm ext}$, and their differences from the measured curve are indicated. The black and red elliptical curves correspond to cleaned and original images, illustrating the maximum possible effect of star removal. The 2MASS 14-arcsec aperture (white) and the used elliptical isophotes (black) are displayed on top of the images. Plots for all galaxies are available at the NIRS0S website (http://www.oulu.fi/astronomy/NIRS0S_pub/Kcalibration.html).

cumulative magnitudes using both circular (lower left-hand panel) and elliptical (lower right-hand panel) apertures. Also shown are the NIRS0S images: in the left-hand panel, the cleaned image, convolved to FWHM = 2.5 arcsec, and in the right-hand panel, the original image before the removal of foreground stars. The elliptical aperture plot includes cumulative magnitudes from both the cleaned (black line) and the original images (red dashed line), to illustrate the possible effect of individual bright stars. As described above, the circular aperture growth curve is adjusted to go exactly through the m_{14} point at $r = 7$ arcsec, while the elliptical aperture fluxes measured at r_{k20} and $r_{\rm ext}$ usually deviate slightly from the tabulated k_{20} and $k_{\rm ext}$. We use the deviations of these quantities to control the possible inaccuracy of the flux calibration, and list them in Table 2 for each galaxy. Note that even large deviations do not indicate errors in our calibration, based solely on the m_{14} aperture magnitude: in some cases, the deviations are connected to bright stars near the galaxy or to the presence of a nearby galaxy. For a few cases, where reliable background subtraction was difficult due to the small FOV compared to the galaxy size, we made small adjustments to the sky background based on matching the 2MASS k_{20} value.

In case 2MASS data were not available (NGC 1161), or when there were reasons to believe that the above calibration is not reliable (interacting systems), we adopted the average zero-point value derived for the NIRS0S observing run in question (see Fig. 2). For some interacting pairs, the difference in μ_0, compared to that obtained directly from the 2MASS m_{14} calibration, is less than 0.1 mag (NGC 2292/2293, 4105/4106), but in some cases, the difference is larger (NGC 5353/5354, 5636, 6438). For NGC 4474, for which the 2MASS values m_{14}, k_{20} and $k_{\rm ext}$ were mutually inconsistent, the 2MASS calibration was not used.

For comparison, standard stars were observed during one campaign, at the NTT in 2004. Flux calibration standards of Persson et al. (1998) were used: 10 standards at each night were observed, using an observing block where the star was integrated in the four corners of the frame. The images were combined in a similar manner to the science images. Using the standard star measurements, the following zero-points and extinction coefficients were obtained for the three nights:

$$K_{\rm s} = k_{\rm s} + 22.399 \pm 0.072 - 0.062 \pm 0.061X \text{ (first night)},$$
$$K_{\rm s} = k_{\rm s} + 22.350 \pm 0.036 - 0.020 \pm 0.029X \text{ (second night)},$$
$$K_{\rm s} = k_{\rm s} + 22.392 \pm 0.041 - 0.065 \pm 0.03X \text{ (third night)},$$

where $K_{\rm s}$ is the total magnitude in the photometric system, $k_{\rm s} = -2.5\log_{10}(\sum F_{i,\rm star})$ is the instrumental magnitude of the star and X is the airmass. The zero-points and extinction coefficients are very similar for the first and the third nights, which were photometric. Comparison with the 2MASS-based calibration (Fig. 3) shows very good agreement: at most, there is a marginal 0.02 mag systematic shift, which, however, is comparable to the internal scatter of the two sets of calibrations. Without the convolution to FWHM = 2.5 arcsec, the systematic difference would be clear, about 0.04 mag. Based on this observing campaign, we estimate that any possible systematic error in μ_0 introduced by using the 2MASS-based calibration is less than 0.05 mag.

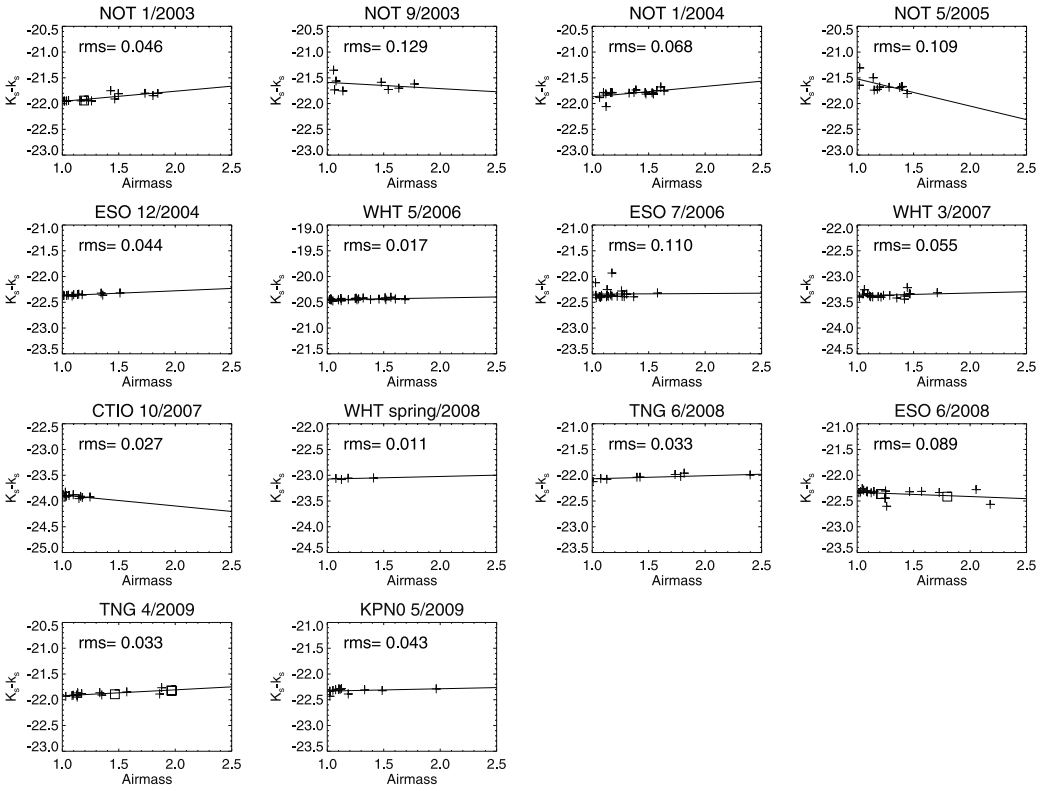

Figure 2. The zero-points derived based on 2MASS 14-arcsec aperture calibration are displayed versus airmass, for the 14 different observing campaigns. The rms scatter for each campaign is indicated. The boxes mark galaxies for which the zero-point was adopted based on fitted campaign values, instead of using 2MASS aperture measurement.

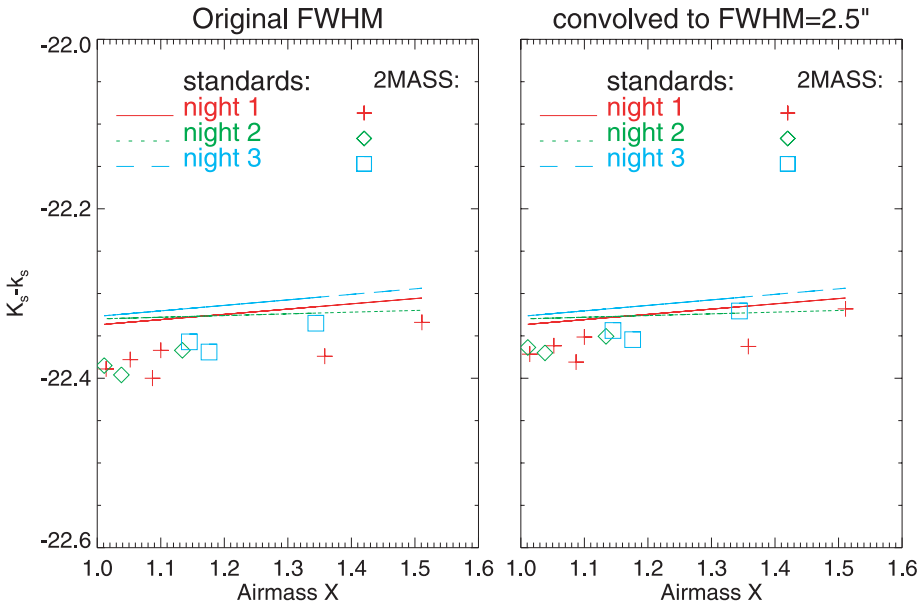

Figure 3. Comparison between 2MASS and standard star calibration based zero-points [$\mu_0 = -(K_s - k_s)$]. The three curves with different colours indicate linear fits for zero-point versus airmass, obtained by observing 10 standard stars per night. The symbols indicate zero-points derived for the galaxies observed during the same nights, based on 2MASS calibrations. In the left-hand plots, applying 2MASS calibration to original images (with typical FWHM $\sim$ 1–2 arcsec), there is about 0.04 mag shift between the calibration methods. However, after allowing for the poorer seeing of 2MASS images (FWHM = 2.5 arcsec), the systematic shift is about 0.02 mag.

The NIRS0S images are deep: Table 2 lists the 1σ sky deviation per arcsec^2, calculated from

$$\sigma_{\rm sky} = -2.5 \log_{10}(\Delta F_{\rm sky}/{\rm pix}) + \mu_0,$$

where $\Delta F_{\rm sky}$ is the sky rms variation, obtained by measuring it at several locations outside the galaxy. Depending on the telescope, exposure time and sky conditions, the values range from 21 to 23 mag arcsec^{-2}, with mean $\langle \sigma_{\rm sky} \rangle \approx 22.2$ mag arcsec^{-2}. However,

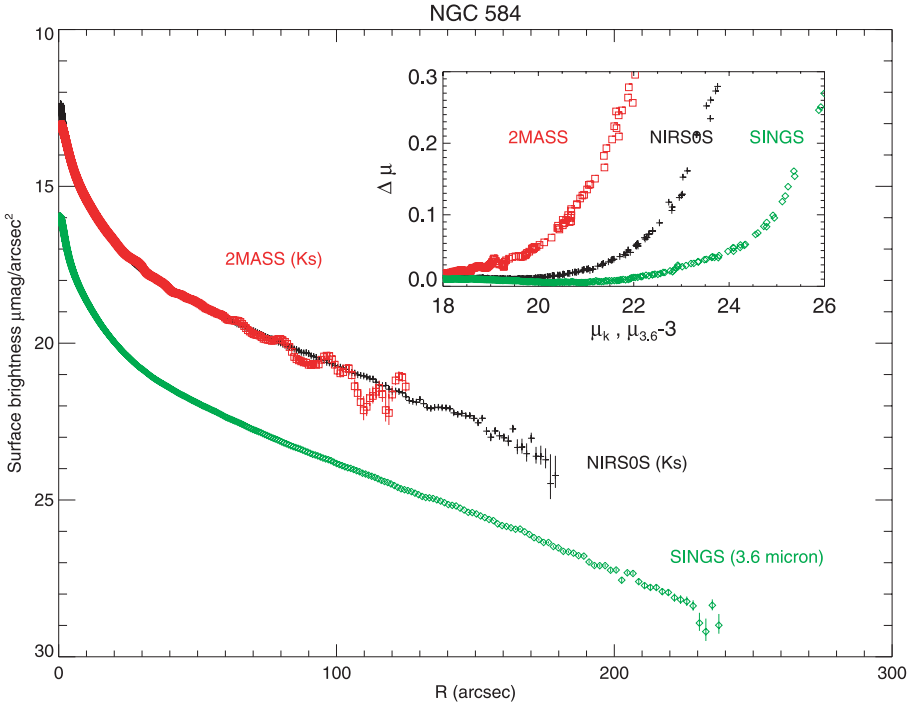

Figure 4. Example of a NIRS0S surface brightness profile for NGC 584. The large figure shows the brightness profile versus isophotal radius, obtained with the IRAF ELLIPSE routine. Fixed orientation and ellipticity are used: PA = 73°.6 and $q = 0.675$ correspond to estimated outer disc orientation. The error bars indicate the uncertainties $\delta\mu$ returned by the ELLIPSE routine. Before calculating the profile, the NIRS0S image was rebinned by a factor of 3, to pixel size 0.86 arcsec. For comparison, also the profiles derived from the 2MASS atlas image (pixel size 1 arcsec) and SINGS (pixel size 0.75 arcsec, 3.6-μm IRAC1 band) are shown: allowing for the ≈3 mag shift between the K_s band and the 3.6 μm AB-system magnitudes. All profiles agree well, except for extending to different depths. The figure in the inset shows $\Delta\mu$ versus μ (taking into account the aforementioned difference between 2MASS/NIRS0S and SINGS magnitude systems), illustrating the ≈2–3 mag differences in depth between the images.

the azimuthally averaged surface brightness profiles are more illustrative than $\sigma_{\rm sky}$ to show the real image depth, extending to 23–24 mag arcsec^{-2}, depending on the galaxy. A typical example is shown in Fig. 4 for NGC 584 (with $\sigma_{\rm sky} = 21.8$ mag arcsec^{-2}), with profiles from the 2MASS atlas image (Jarrett et al. 2000) and from the SINGS 3.6-μm image (Kennicutt 2003) overlaid for comparison. For NGC 584, the useful NIRS0S profile ($\Delta\mu \leq 0.2$) extends to about 23.5 mag arcsec^{-2} or 2–3 mag deeper than the 2MASS profile. Allowing for the difference in the band and magnitude system, it is only about 2 mag shallower than the deep *Spitzer* image (see the inset in Fig. 4). In B magnitudes, 23.5 mag arcsec^{-2} in the K_s band translates roughly to a surface brightness of 27.5 mag arcsec^{-2}. However, not all of the galaxies in our sample are visible at this surface brightness level, for instance, because the FOV is too small, the galaxies are strongly interacting or in a very few cases because the sky background is not stable enough, in which case the sky gradients limit the useful image depth. In radial extent, our example galaxy is 1.4–1.6 times larger than the 2MASS image and 0.8 times that of the extent of the SINGS image.

4 THE IMAGE ATLAS

4.1 The atlas images

The flux-calibrated image atlas appears in Fig. 5. One example of the full layout of the atlas is shown, whereas for 16 of the galaxies discussed in the text, only the images in the top panel are shown. The complete atlas is available in electronic form as Supporting Information with the online version of the article. The images will also be available at CDS (http://cdsarc.u-strasbg.fr/cats).[5] The images are shown in logarithmic form, in units of mag arcsec^{-2}, maintaining the full pixel resolution (upper panel). The magnitude range is given in the right-hand bar, which is selected individually for each galaxy so that the full scale of structures is visible. In order not to add any artefacts due to bad-foreground-star removal, the images before the star removal are shown. Our visual and photometric (in brackets) classifications (see Section 5) are marked in the figures. A drawback of this layout is that it does not do full justice to the real image depth, failing to show the faint outer regions.

These faint outer structures are shown in one of the small panels, where rebinned images cleaned of foreground stars are shown. The galaxies are shown in many different radial and brightness scales, the number of frames depending on the complexity of a galaxy's morphology. In some of the galaxies, faint bars, lenses or dust lanes are overshadowed by prominent bulges. These components were made visible using 2D multicomponent structural decompositions previously given for the atlas galaxies by Laurikainen et al. (2010): the bulge model was subtracted from the original image, leaving the faint structures visible in the residual images. Alternatively, unsharp masked images are shown. They were created by smoothing the images by 5–20 pixels and then subtracting smoothed images from the original images. The upper left-hand small panel shows the image rebinned by a factor that best demonstrates the faint outer structure of the galaxy, whereas the lower right-hand panel generally shows either the residual image or the unsharp masked image. In

[5] The images' in.fits format is available with the PI of the article.

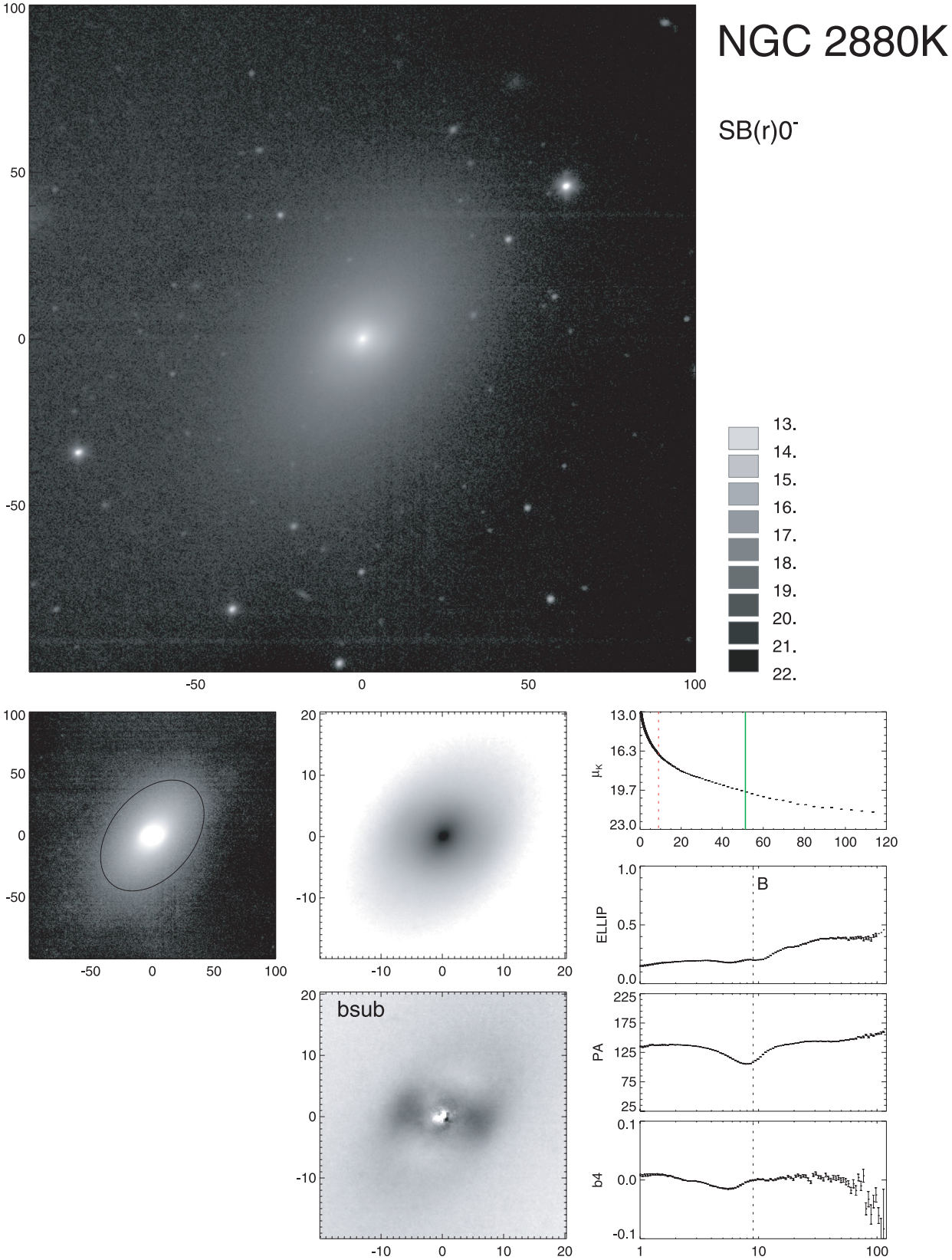

Figure 5. One example, NGC 2880, of the layout of the atlas galaxies is shown, explained in more detail in the text. Also shown are the atlas images for 16 other galaxies, for which only the top panels are presented. The complete atlas is available as Supporting Information with the online version of this article, and at http://www.oulu.fi/astronomy/NIRS0S_pub/atlas.html.

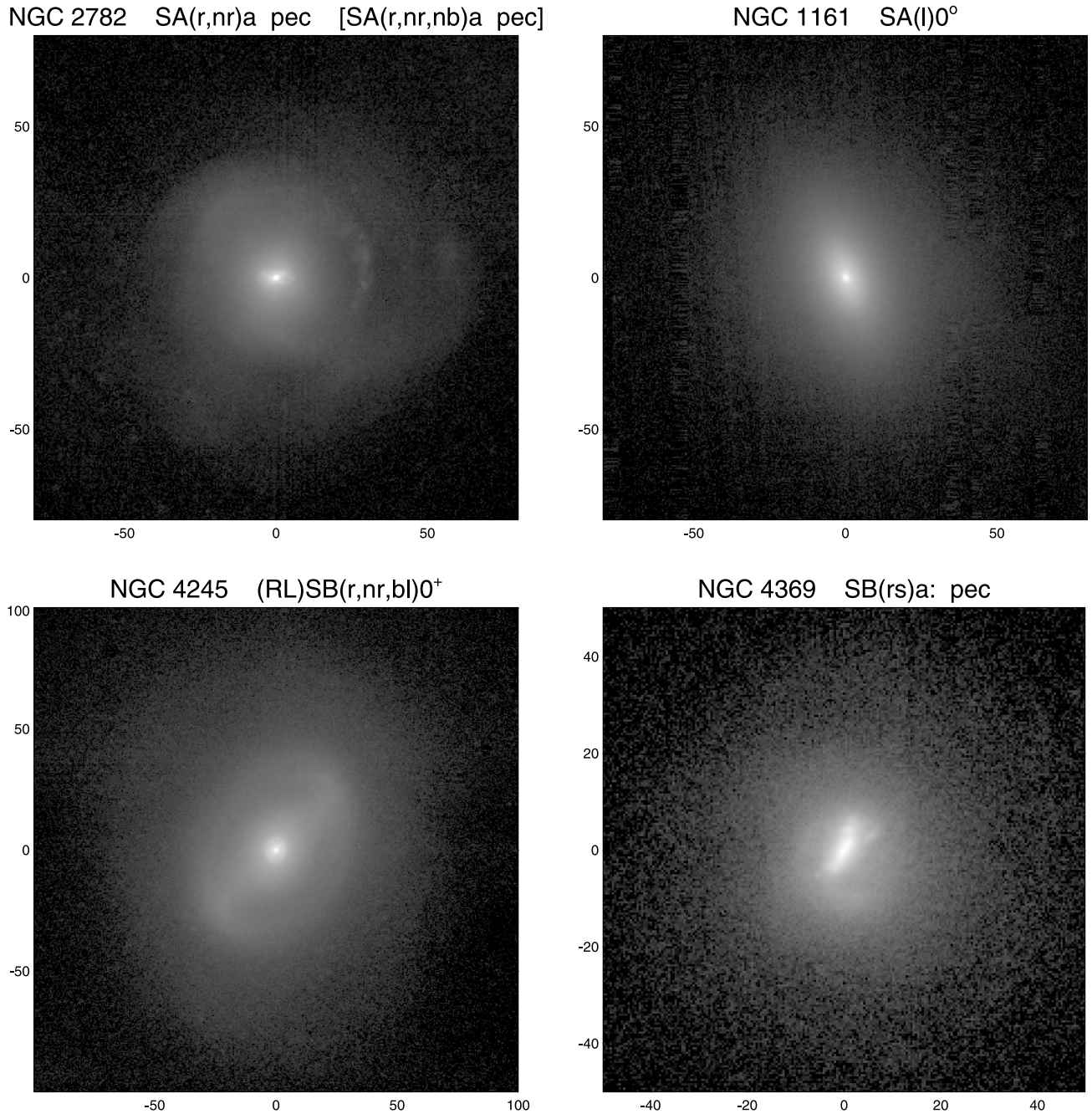

Figure 5 – *continued*

such cases, a text 'bsub' or 'unsharp' is overlaid on the image. The detected faint structures form part of our photometric classification.

4.2 Ellipse fitting

The atlas figures also show isophotal analysis results, which consist of fitting elliptical isophotes to the images using the ELLIPSE routine in IRAF. This routine uses a technique in which Fourier series are fitted to concentric isophotes (Jedrzejewski 1987). The quality of the fit is evaluated by inspecting the 1D brightness distribution as a function of PA, so that the harmonic content of this distribution is analysed. The fourth-order coefficient $b4$ of the best-fitting Fourier series then measures the isophote's deviations from perfect ellipticity. We calculate the radial profiles of the PA, ellipticity $\epsilon = 1 - q$ (where $q = b/a$ is the minor-to-major-axis ratio) and parameter $b4$. Non-rebinned images were used and the centre was fixed to the value estimated by the IMCNTR routine in IRAF. Logarithmic radial spacing was used along the semi-major-axis while fitting the elliptical isophotes. In order to minimize the effects of noise and contamination by bad pixels and cosmic rays, deviant pixels above 3σ were rejected.

The surface brightness profiles and the radial profiles of PA, ϵ and $b4$ are shown in Fig. 5. The full green vertical line shows r_{20}, which is the 2MASS isophotal radius of the 20 mag arcsec^{-2} contour in the K_s band. The radius r_{20} is marked with a black ellipse in the upper left panel, using 2MASS PA ϕ_{k20} and axial ratio $(b/a)_{k20}$. The

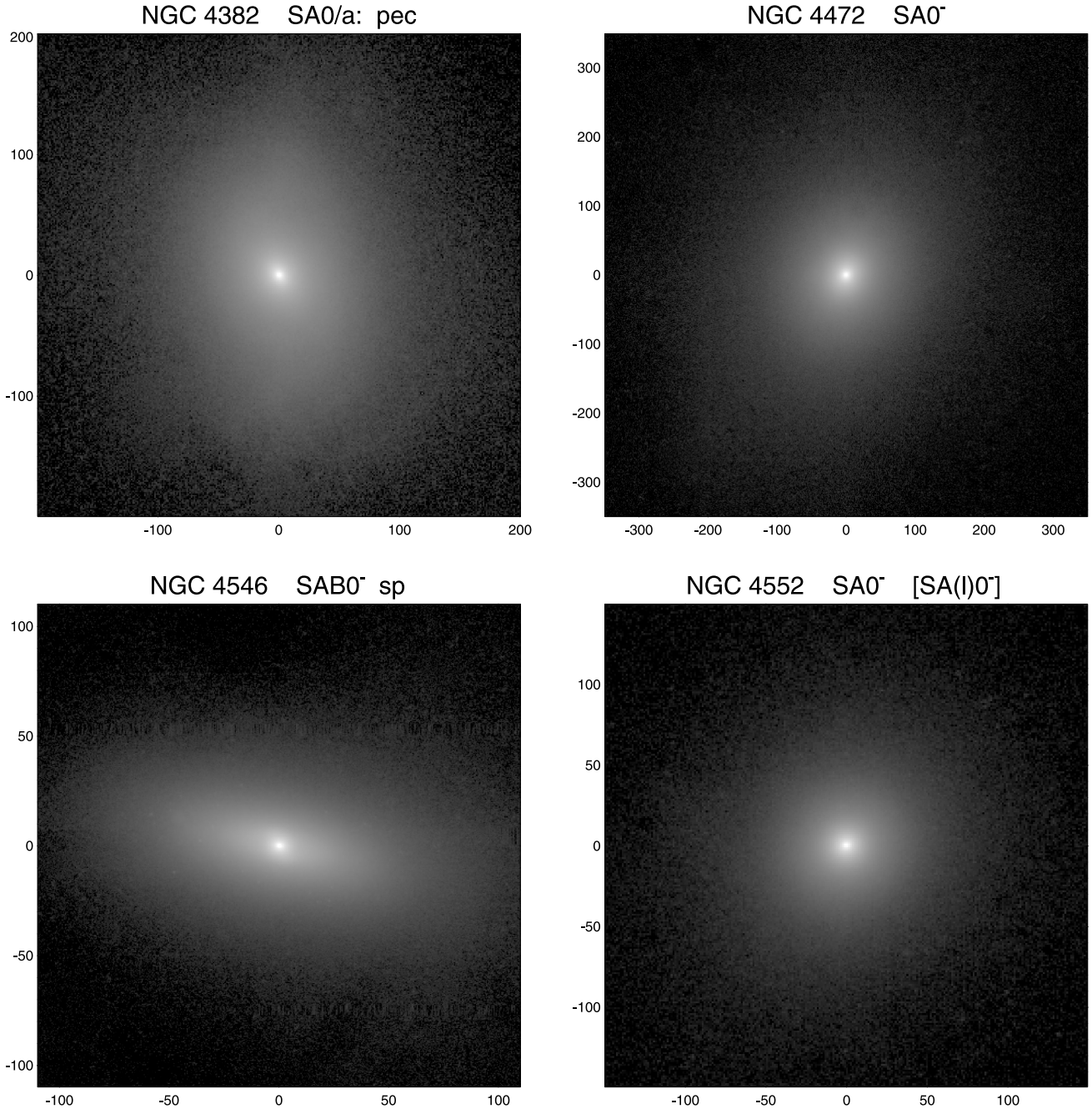

Figure 5 – *continued*

dashed vertical lines show the radii of the bars in our classification (see Section 5). In some cases, the r_{20} isophotal orientations from the 2MASS deviate from the orientations in our images. This is because for these galaxies the 2MASS images trace only the inner components of the galaxies; the outermost components detected by us have different orientations.

5 MORPHOLOGICAL CLASSIFICATION

5.1 Brief history

The identification of S0s traces back to Lundmark (1926) and Reynolds (1927), who recognized a group of amorphous galaxies without any sign of spiral arms, a group of galaxies which form the modern class of E+S0 galaxies. Early-type galaxies were seen as a sequence of increasing flattening towards later types. In *Realm of the Nebulae*, Hubble (1936) described hypothetical S0s, which, based on Hubble's notes, Sandage (1962) included in the Hubble sequence as *transition types between the ellipticals and the spirals*. As a real physical scenario, this idea was abandoned when it was found that S0s have a similar flattening distribution to spirals, which clearly deviates from that for the elliptical galaxies (Sandage, Freeman & Stokes 1970).

De Vaucouleurs (1959) further refined the Hubble/Sandage classification by adding the *stage* ($S0^-$, $S0^0$, $S0^+$), *family* (A, AB, B) and *variety* (s, r), as well as the outer ring/pseudo-ring designation

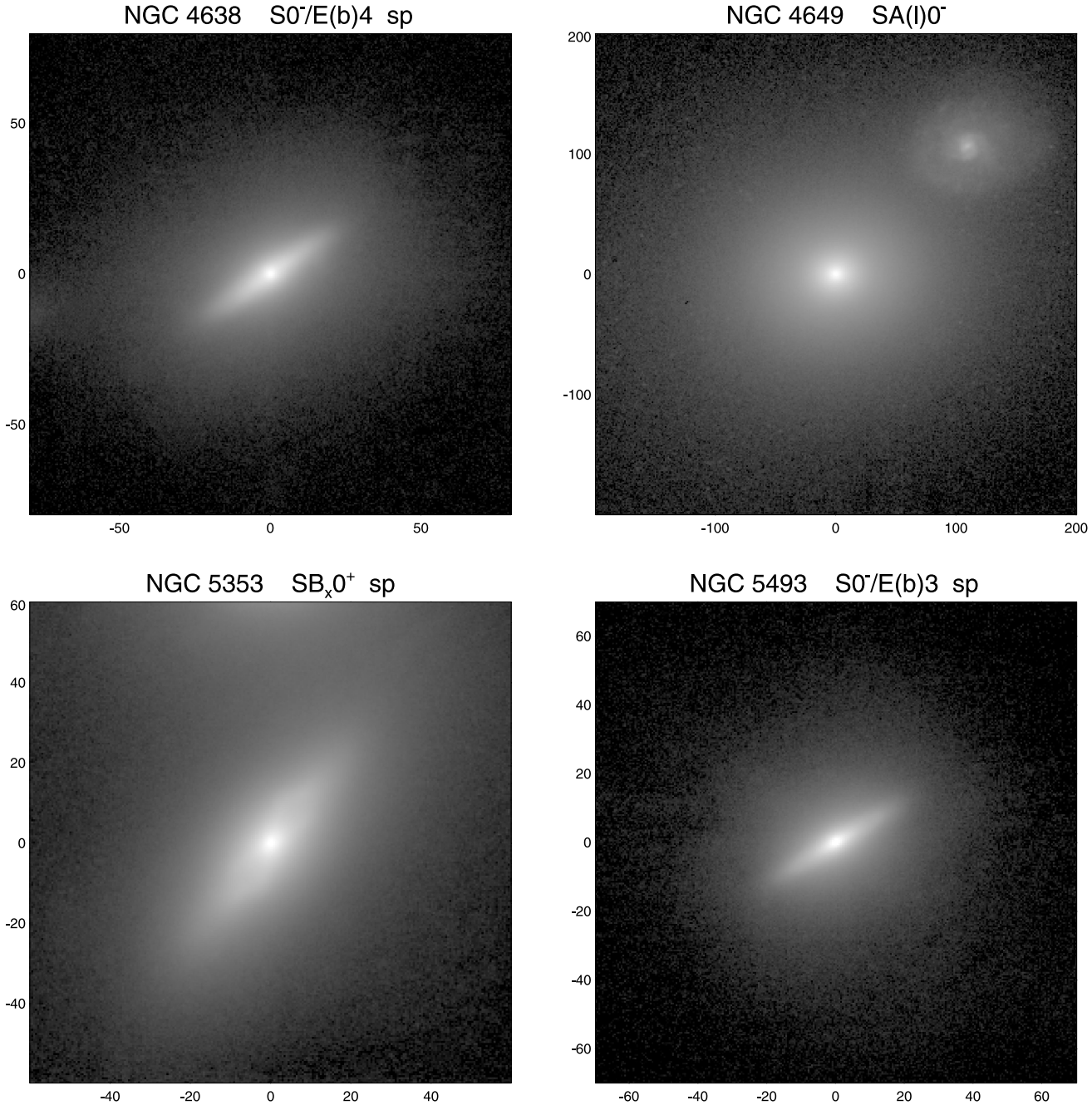

Figure 5 – *continued*

to the S0 class. Concerning spiral arms, he was less restrictive in the sense that the (r) and (s) varieties were carried even into the earliest S0 classification, called $S0^{-}$, although such cases are difficult to recognize. In the classification by Sandage & Tammann (1981), the stage was given in a similar manner to that in de Vaucouleurs' classification, except for different symbols used ($S0_1$, $S0_2$, $S0_3$). They also added flattening of a galaxy into their coding. Outer ring classification was fine-tuned by Buta & Crocker (1991) and Buta (1995). The morphology of bars in terms of boxy/peanut/x-shaped structures was included in the classification by Buta et al. (2010) for 200 galaxies using S^4G *Spitzer* images (Sheth et al. 2010). Buta et al. also suggested a notation 'nb' for nuclear bars and 'nr' for nuclear rings. Kinematic observations for edge-on galaxies (Kuijken & Merrifield 1995; Bureau & Freeman 1999) have shown that boxy/peanut/x-shaped structures are inner parts of bars. Although lenses form part of the classification of S0s, they were not coded into the morphological classification. For lenses, Kormendy (1979) suggested a coding where 'l' stands for an inner and 'L' for an outer lens (as used in dVA), whereas Buta et al. (2010) suggested a notion 'nl' for nuclear lenses.

The classification has been developed along with new ideas of galaxy formation and evolution. That was already the case when Baade (1963) suggested that S0s are stripped spirals formed in galaxy interactions. The idea was developed by van den Bergh (1976), leading to a classification where the S0s form a sequence from early to late types, similar to that used for the spirals

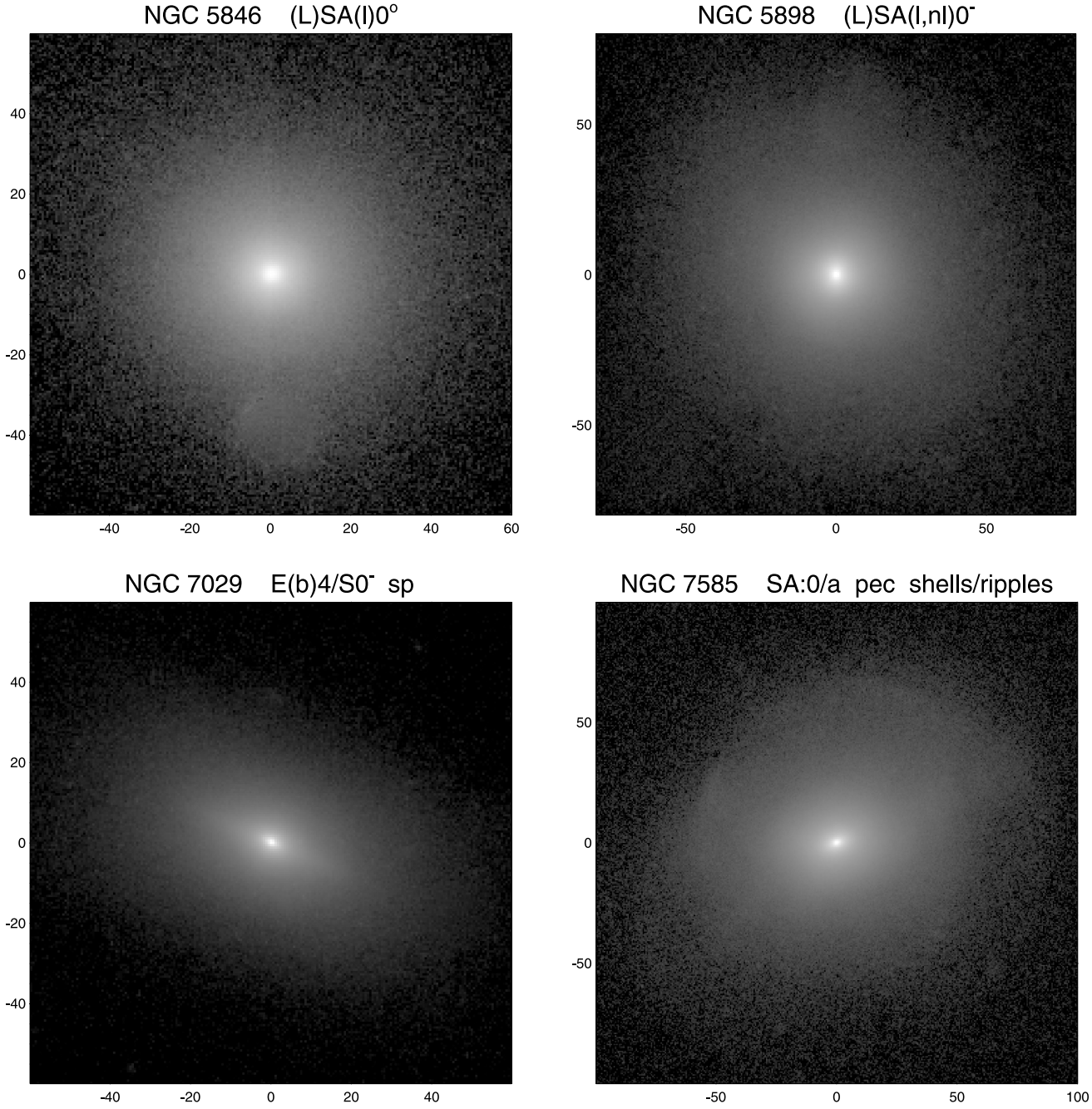

Figure 5 – *continued*

($S0_a$, $S0_b$, $S0_c$). It was based on the supposition that there may exist anemic S0s, which have similar surface brightness distributions to the Sa-, Sb- and Sc-type spirals. In this scenario, small low-luminosity bulges are also expected among S0s. The hypothesis was tested by Sandage & Bedke (1994) for 200 bright S0s, but no such S0s were found. However, multicomponent structure analysis has cast new light on this approach (see Laurikainen et al. 2010). A dust-penetrated classification was suggested by Buta & Block (2001), where a bar-induced torque forms part of the classification. This was based on the idea that bars are a driving force of secular evolution, thus modifying galaxy morphology.

Early-type disc galaxies typically have faint structures that are easily missed in visual classification. In particular, late-type ellipticals and early-type S0s are difficult to distinguish due to the subtle oval or twisted structures or due to faint outer discs in S0s. Indeed, Sandage & Bedke (1994) report many misclassified S0s in the RC3. Therefore, sometimes photometric classification is also used. For example, Kormendy et al. (2009) used isophotal analysis to show the appearance of discs in galaxies in which the discs were not obvious in the direct images. It was assumed that discs are more flattened than bulges.

In this study, both visual and photometric classifications are made, given in Tables 3 and 4. For comparison, in Table 3, we give also the classifications from the RC3 and RSA. Our classification is purely morphological, and no assumptions of possible formative processes of galaxies are made. Although our images do

Table 3. Visual classification in the near-IR, compared with optical classification (RC3 and RSA).

Galaxy (1)	Type (2.2 μm) (2)	Type (RC3) (3)	Type (RSA) (4)	T (2.2 μm) (5)	T (RC3) (6)
IC 1392*	E(b)4/S0$^-$ sp	.L..-*.		−4.0	−3.0
IC 4214* [1]	(R$_1$)S$\underline{\text{A}}$B(r,nr)0$^+$	PSBR2..		−1.0	1.5
IC 4329*	SA0^o shells/ripples	.LXS-..	S01(5)	−2.0	−3.0
IC 4889*	SA0$^-$	.E.5+..	S01/2(5)	−5.0	−5.0
IC 4991* [1]	coreE	.LAR0?P		−5.0	−2.0
IC 5240*	SB$_x$(r)a	.SBR1..	SBa(r)	1.0	1.0
IC 5267* [1]	(RL)SA(l)0/a	.SAS0..	Sa(r)	0.0	0.0
IC 5328*	S$\underline{\text{A}}$B$_a$(l)0$^-$	.E.4...	S01(3)	−3.0	−5.0
ESO 208−21*	E4/S0$^-$ sp	.LX.-..		−4.0	−3.0
ESO 137−10*	SA0$^+$:	PLXS-*.		−1.0	−2.7
ESO 337−10[1]	E$^+$3/SA0$^-$	.L?....		−3.5	
NGC 0439*	SA0$^-$	.LXT-?.	E5	−3.0	−3.3
NGC 0474*	(RL)SAB0/a shells/ripples	.LAS0..	RS0/a	0.0	−2.0
NGC 0484[1]	SA0$^-$	.LA.-..		−3.0	−3.0
NGC 0507* [1]	(L)SAB0$^-$	.LAR0..		−3.0	−2.0
NGC 0524*	(L)SA(l,nl)0^o	.LAT+..	S0$_2$/Sa	−2.0	−1.0
NGC 0584* [1]	SAB(l)0$^-$	.E.4...	S0$_1$(3,5)	−3.0	−5.0
NGC 0718*	(R′)SAB(rs,nl)a	.SXS1..	SaI	1.0	1.0
NGC 0890*	SA0$^-$	.LXR-$.	S0$_1$(5)	−3.0	−3.0
NGC 0936*	SB($\underline{\text{r}}$s,bl)0$^+$	.LBT+..	SB0$_{2/3}$/SBa	−1.0	−1.0
NGC 1022* [1]	SAB(r′l,bl)a	PSBS1..	SBa(r) pec	1.0	1.0
NGC 1079* [1]	(RL)SAB$_a$(rs,bl)0$^+$	RSXT0P.	Sa(s)	−1.0	.0
NGC 1161*	SA(l)0^o	.L.....		−2.0	−2.0
NGC 1201* [1]	SAB$_a$(r′l,bl,nb)0^o	.LAR0*.	S0$_1$(6)	−2.0	−2.0
NGC 1302*	SAB(rl)0$^+$	RSBR0..	Sa	−1.0	.0
NGC 1317*	SAB(r′l,nr$_1$,nr$_2$,nl,nb)0/a	.SXR1..		0.0	1.0
NGC 1326*	(R)SAB$_a$(r,nr,nb,bl)0$^+$	RLBR+..	RSBa	−1.0	−1.0
NGC 1344* [1]	SA0$^-$	.E.5...	S0$_1$(5)	−3.0	−5.0
NGC 1350* [1]	(R$'_1$)SAB$_a$($\underline{\text{r}}$s,bl)a	PSBR2..	Sa(r)	1.0	1.8
NGC 1351	E6	.LA.-P*	S0$_1$(6)/E6	−5.0	−3.0
NGC 1371*	(RL)SAB(rs,l)a	.SXT1..	Sa(s)	1.0	1.0
NGC 1380*	SAB(s)0/a	.LA....	S0$_3$(7)/Sa	0.0	−2.0
NGC 1387*	SB(nrl)0$^-$	.LXS-..	SB0$_2$(pec)	−3.0	−3.0
NGC 1389*	SAB(l,nb)0$^-$	.LXS-*.	S0$_1$(5)/SB0$_1$	−3.0	−3.3
NGC 1400* [1]	E$^+$2/SA0$^-$	.LA.-..	E1/S0$_1$(1)	−3.5	−3.0
NGC 1411*	SA(l,nl)0^o	.LAR-*.	S0$_2$(4)	−2.0	−3.0
NGC 1415	(RL)SAB$_a$(r′l,nr)0$^+$	RSXS0..	Sa/SBa late	−1.0	.0
NGC 1440	(L)SB($\underline{\text{r}}$s,bl)0^o	PLBT0*.	S0$_1$(5)/SB0$_1$	−2.0	−1.9
NGC 1452	(R′)SB$_a$(r,bl)a	PSBR0..	SBa(r)	1.0	.4
NGC 1512*	SB$_a$($\underline{\text{r}}$s,nr,bl)a	.SBR1..	SBb(rs)I pec	1.0	1.0
NGC 1533*	(RL)SB(bl)0^o	.LB.-..	SB0$_2$(2)/SBa	−2.0	−3.0
NGC 1537*	SB(rl)0^o	.LX.-P?	E6	−2.0	−2.5
NGC 1543*	(R)SB(l,nl,nb)0$^+$	RLBS0..	RSB0$_{2/3}$(0)/a	−1.0	−2.0
NGC 1553*	SA(rl,nl,nb)0^o	.LAR0..	S0$_{1/2}$(5) pec	−2.0	−2.0
NGC 1574*[1]	(L)SB(l)0$^-$	.LAS-*.	SB0$_2$(3)	−3.0	−2.7
NGC 1617*	(R′)SAB$_a$(rs)0/a	.SBS1..	Sa(s)	0.0	1.0
NGC 2196*	SA(l)a	PSAS1..	Sab(s)I	1.0	1.0
NGC 2217*	(R)SB($\underline{\text{r}}$s,nl,nb)0/a	RLBT+..	SBa(s)	0.0	−1.0
NGC 2273*	(R)SAB(rs,bl,nb)a	.SBR1*.		1.0	.5
NGC 2292* [1]	E: pec	.LX.0P.		−5.0	−2.0
NGC 2293*	SAB$_a$(bl)0/a	.LXS+P.		0.0	−1.0
NGC 2300*	(R′L)SA(sl)0^o	.LA.0..	E3	−2.0	−2.0
NGC 2380*	SA(l,nl)0$^-$	.LX.0*.		−3.0	−1.7
NGC 2460	S$\underline{\text{A}}$B(rs)a	.SAS1..	Sab(s)	1.0	1.0
NGC 2523[1]	SB(r)ab	.SBR4..	SBb(r)I	2.0	4.0
NGC 2549	SB$_x$0^o sp	.LAR0./	S0$_{1/2}$(7)	−2.0	−2.0
NGC 2655*	S$\underline{\text{A}}$B(s)0/a pec	.SXS0..	Sa pec	0.0	.0
NGC 2681* [1]	(RL)SAB($\underline{\text{r}}$s,ob)0/a	PSXT0..	Sa	0.0	.0
NGC 2685*	S0$^+$: sp polar ring	RLB.+P.	S0$_3$(7) pec	−1.0	−1.0
NGC 2768*	E(d)6	.E.6.*.	S0$_{1/2}$(6)	−5.0	−5.0
NGC 2781*	(RL)S$\underline{\text{A}}$B(rl,nr)0$^+$	.LXR+..	Sa(r)	−1.0	−1.0
NGC 2782* [1]	SA(r,nr)a pec	.SXT1P.	Sa(s) pec	1.0	1.0

Table 3 – *continued*

Galaxy (1)	Type (2.2 μm) (2)	Type (RC3) (3)	Type (RSA) (4)	T (2.2 μm) (5)	T (RC3) (6)
NGC 2787*	SB_a(nrl,bl)0^o	.LBR+..	SB0/a	−2.0	−1.0
NGC 2855	SA(s)0^o	RSAT0..	Sa(r)	−2.0	.0
NGC 2859*	(R)SAB_a(rl,nl,nb,bl)0^+	RLBR+..	$RSB0_2$(3)	−1.0	−1.0
NGC 2880	SB(r)0^-	.LB.-..	SB01	−3.0	−3.0
NGC 2902[1]	SA(rl)0^+	.LAS0*.	$S0_1$(0)	−1.0	−2.0
NGC 2911*	$SA0^-$	.LAS.*P	$S0_3$(2) or S0pec	−3.0	−2.0
NGC 2950*	SB_a(l,nrl,nb)0^o	RLBR0..	$RSB0_{2/3}$	−2.0	−2.0
NGC 2983	(L)SB_a(s,bl)0^+	.LBT+..	SBa SB 1	−1.0	−1.0
NGC 3032	SA(rl_1,rl_2)0^o	.LXR0..	$S0_3$(2)/Sa	−2.0	−2.0
NGC 3081	(R_1)SAB(r,nr,nb)0^+	RSXR0..	SBs(s)	−1.0	.0
NGC 3100*	SAB(s)0^o	.LXS0P.		−2.0	−2.0
NGC 3166*[1]	SAB_a(rl,nl)a	.SXT0..	Sa(s)	−1.0	.0
NGC 3169*	SA0/a: pec	.SAS1P.	Sb(r)I-II (tides)	0.0	1.0
NGC 3226*	$SA0^-$	.E.2.*P	$S0_1$(1)	−3.0	−5.0
NGC 3227*	SAB_x(s)a	.SXS1P.	Sb(s)III	1.0	1.0
NGC 3245*	(L)SAB_a(rs,nl)0^o	.LAR0*$	$S0_1$(5)	−2.0	−2.0
NGC 3358*	(R_2')SAB_a(rl)a	RSXS0..	Sa(r)I	1.0	.0
NGC 3384*	(L)SB(l,nb,bl)0^-	.LBS-*.	$SB0_1$(5)	−3.0	−3.0
NGC 3412*	(L)SB_a0^-	.LBS0..	$SB0_{1/2}$(5)	−3.0	−2.0
NGC 3414*	$S0^-$/E(d)1 sp	.L...P.	$S0_1$	−4.0	−2.0
NGC 3489*	(RL)SB(r,bl)0/a	.LXT+..	$S0_3$/Sa	0.0	−1.0
NGC 3516*	(R)SB_a(l)0^o	RLBS0*.	$RSB0_2$	−2.0	−2.0
NGC 3607*	(L)SAB0^-	.LAS0*.	$S0_3$(3)	−3.0	−2.0
NGC 3619*	$SA0^-$ shells/ripples	RLAS+*.	Sa	−3.0	−1.0
NGC 3626*	(R)SAB_a(rl,nrl,nb)0/a	RLAT+..	Sa	0.0	−1.0
NGC 3665*[1]	E2	.LAS0..	$S0_3$(3)	−5.0	−2.0
NGC 3706*[1]	$SA0^o$	.LAT-..	E4	−2.0	−3.0
NGC 3718*	SAB(rs,l,nl)a:	.SBS1P.	Sa pec?	1.0	1.0
NGC 3729*	SB(r)0/a	.SBR1P.	SB(ring) pec	0.0	1.0
NGC 3892*	(L)SB(rs)0^+	.LBT+..	$SB0_3$	−1.0	−1.0
NGC 3900*	SA(r)0/a	.LAR+..	Sa(r)	0.0	−1.0
NGC 3941*[1]	(R′L)SB_a(s,bl)0^o	.LBS0..	$SB0_{1/2}$/a	−2.0	−2.0
NGC 3945*[1]	(R)SB_a(rl,nl,bl)0^+	RLBT+..	$RSB0_2$	−1.0	−1.0
NGC 3998*	SA(rl,nb)0^o	.LAR0$.	$S0_1$(3)	−2.0	−2.0
NGC 4073*	E^+5/SAB0^-	.E+....	E5	−3.5	−3.8
NGC 4105*[1]	E^+1/$SA0^-$	.E.3...	$S0_{1/2}$(3)	−3.5	−5.0
NGC 4106*	SAB(s,nl)a	.LBS+..	SB0/a (tides)	1.0	−1.0
NGC 4138*	SA(r)0^+	.LAR+..	Sab(r)	−1.0	−1.0
NGC 4143*	(L,R′L)SAB_a(s,nb,bl)0^-	.LXS0..	$S0_1$(5)/Sa	−3.0	−2.0
NGC 4150*[1]	(L)SA(nl)0^-	.LAR0$.	$S0_3$(4)/Sa	−3.0	−2.0
NGC 4203*	(L,R′L)SAB$_a$(l,rl)0^-	.LX.-*.	$S0_2$(1)	−3.0	−3.0
NGC 4220	(RL)SAB_x(r)0^+ sp	.LAR+..	Sa(r) S R1	−1.0	−1.0
NGC 4245*	(RL)SB(r,nr,bl)0^+	.SBR0*.	SBa(s)	−1.0	.0
NGC 4262*	(IOL,OOL)SB_a(s,nl,bl)0^o	.LBS-$.	$SB0_{2/3}$	−2.0	−3.0
NGC 4267*	(L)SAB0^-	.LBS-$.	$SB0_1$	−3.0	−3.0
NGC 4281*[1]	E^+5/$SA0^-$	.L..+*/	$S0_3$(6)	−3.5	−1.0
NGC 4293*	(RL)SB_x(s)0/a	RSBS0..	Sa pec	0.0	.0
NGC 4314*	(R_1')SB(r′l,nr′,bl)a	.SBT1..	SBa(rs)pec	1.0	1.0
NGC 4339*	SA(r,l)0^o	.E.0...	$S0_{1/2}$(0)	−2.0	−5.0
NGC 4340*	SB_a(r,nr,nb,bl)0^+	.LBR+..	$SB0_2$(r)	−1.0	−1.0
NGC 4350*	$S0^-$ sp	.LA.../	$S0_1$(8)	−3.0	−2.0
NGC 4369*	SB(rs)a: pec	RSAT1..	Sc(s)III-IV	1.0	1.0
NGC 4371*	SB_a(r,nr)0^+	.LBR+..	$SB0_{2/3}$(r)(3)	−1.0	−1.0
NGC 4373*	$SA0^-$: (shells/ripples?)	.LXT-*.	E(4,2)	−3.0	−2.9
NGC 4378*	(R′)SA(l)a	RSAS1..	Sa(s)	1.0	1.0
NGC 4382*	SA0/a: pec	.LAS+P.	$S0_1$(3) pec	0.0	−1.0
NGC 4406*[1]	E^+3	.E.3...	$S0_1$(3)/E3	−4.0	−5.0
NGC 4424*	SB0/a: pec	.SBS1*.	S(a?)pec	0.0	1.0
NGC 4429*	SAB_x(r,nl)0^+	.LAR+..	$S0_3$(6)/Sa pec	−1.0	−1.0
NGC 4435*[1]	$S0^o$ sp	.LBS0..	$SB0_1$(7)	−2.0	−2.0
NGC 4457*	(R)SAB(l,nl,nb)0^+	RSXS0..	RSb(rs)II	−1.0	.0
NGC 4459*[1]	E2	.LAR+..	$S0_3$(3)	−5.0	−1.0

Table 3 – *continued*

Galaxy (1)	Type (2.2 μm) (2)	Type (RC3) (3)	Type (RSA) (4)	T (2.2 μm) (5)	T (RC3) (6)
NGC 4472*	SA0$^-$	.E.2...	E1/S0$_1$(1)	−3.0	−5.0
NGC 4474*	S0$^-$ sp	.L...P*	S0$_1$(8)	−3.0	−2.0
NGC 4477*	(RL)SB(r?)a	.LBS.*$	SB0$_{1/2}$/SBa	1.0	−2.0
NGC 4503*[1]	S$\underline{\text{A}}$B(s,bl)0^o	.LB.-*.	Sa	−2.0	−3.0
NGC 4531*	(RL)SA(rs)a	.LB.+*.		1.0	−.5
NGC 4546[1]	SAB0$^-$ sp	.LBS-*.	SB0$_1$/Sa	−3.0	−3.0
NGC 4552*[1]	SA0$^-$	.E.0+..	S0$_1$(0)	−3.0	−5.0
NGC 4578*	SA0$^-$	.LAR0*.	S0$_{1/2}$(4)	−3.0	−2.0
NGC 4596*	(RL)SB(rs,bl)0/a	.LBR+..	SBa(very early)	0.0	−1.0
NGC 4608*	SB(r,bl)0$^+$	.LBR0..	SB0$_3$/a	−1.0	−2.0
NGC 4612*	(RL)S$\underline{\text{A}}$B$_a$(l)0^o	RLX.0..	RSB0$_{1/2}$	−2.0	−2.0
NGC 4638*	S0$^-$/E(b)4 sp	.L..-./	S0$_1$(7)	−4.0	−3.0
NGC 4643*	(L)SB(r$\underline{\text{s}}$,nrl,bl)0$^+$	.SBT0..	SB0$_3$/SBa	−1.0	.0
NGC 4649*	SA(l)0$^-$	.E.2...	S0$_1$(2)	−3	−5.0
NGC 4665*	(R′L)SB(s)0$^+$	.SBS0..	SB0$_{1/3}$/SBa:	−1.0	.0
NGC 4691*	SB(s)dm/SB0/a	RSBS0P.	SBb pec	0.0	.0
NGC 4694*	SA0$^-$(nb)	.LB..P.	Amorphous	−3.0	−2.0
NGC 4696*[1]	E$^+$2	.E+1.P.	(E3)	−4.0	−4.0
NGC 4754*[1]	(L)SB$_a$(s,bl)0$^-$	.LBR-*.	SB0$_1$(5)	−3.0	−3.0
NGC 4772*	(R′)SA(r)a	.SAS1..	Sa:	1.0	1.0
NGC 4880*	(R′)S$\underline{\text{A}}$B(s)a	.LAR+*.	E4/S0$_1$(4)	1.0	−1.0
NGC 4914*	SA0$^-$	.E+....	[S0$_1$(5)]	−3.0	−4.0
NGC 4976*[1]	E$^+$5/SA0$^-$	.E.4.P*	S0$_1$(4)	−3.5	−5.0
NGC 4984*[1]	(R)SAB$_a$(l,nrl)0^o	RLXT+..	Sa(s)	−2.0	−1.0
NGC 5026*	(L)SB(rs,nl,bl)a	PSBT0..		1.0	−.2
NGC 5078*	Sa sp	.SAS1*/		1.0	1.0
NGC 5087*[1]	E2/SA0$^-$ sp	.LA.*..	S0$_3$(5)	−4.0	−3.0
NGC 5101*	(RR)SB(r$\underline{\text{s}}$,nl,bl)0/a	RSBT0..	SBa	0.0	.0
NGC 5121*	(RL)SA(rl)0$^+$	PSAS1..	S0$_1$(4)/Sa	−1.0	1.0
NGC 5206*	dSB0,N	PLBT0P*		−2.0	−2.5
NGC 5266*	SA0$^-$	.LA.-*.	S0$_3$(5) pec (prolate)	−3.0	−3.0
NGC 5273*[1]	SA(s)0^o	.LAS0..	S0/a	−2.0	−2.0
NGC 5308	S0$^-$ sp	.L..-./	S0$_1$(8)	−3.0	−3.0
NGC 5333	(RL)SA(rl,nb)0^o	.LBR0*.		−2.0	−2.0
NGC 5353*	SB$_x$0$^+$ sp	.L..../	S0$_1$(7)/E7	−1.0	−2.0
NGC 5354*	E1	.L..../		−5.0	−2.0
NGC 5365*	(RL)SB$_a$(rs,nr,nb)0^o	RLBS-..	RSB0$_{1/3}$	−2.0	−3.0
NGC 5377*[1]	(R$_1$)SA$\underline{\text{B}}_x$(rl,nl)0/a	RSBS1..	SBa or Sa	0.0	1.0
NGC 5419*	SA(nl)0$^-$	.E.....	S0$_1$(2)	−3.0	−4.7
NGC 5448*	(R′)SAB$_x$(r$\underline{\text{s}}$,nl)a	RSXR1..	Sa(s)	1.0	1.0
NGC 5473*	(L)SB0$^-$	.LXS-*.	SB0$_1$(3)	−3.0	−3.0
NGC 5485*[1]	E(dust lane)/SA0$^-$	.LA..P.	S0$_3$(2) pec (prolate)	−4.0	−2.0
NGC 5493*	S0$^-$/E(b)3 sp	.L...P/	E7/S0$_2$(7)	−3.0	−2.0
NGC 5631*[1]	SA0$^-$	.LAS0..	S0$_3$(2)/Sa	−3.0	−2.0
NGC 5638	SA(l)0$^-$	.E.1...	E1	−3.0	−5.0
NGC 5701*	(R′)SB(rl,bl)0/a	RSBT0..	(PR)SBa	0.0	.0
NGC 5728*	(R$_1$)SB(r$\underline{\text{s}}$,nr,nb)a	.SXR1*.	SBb(s)II	1.0	1.0
NGC 5750	(RL)S$\underline{\text{A}}$B$_a$(r,l,bl)0/a	.SBR0..	SBa(s)	0.0	.0
NGC 5838	(L)SAB(nl,bl)0^o	.LA.-..	S0$_2$(5)	−2.0	−3.0
NGC 5846*	(L)SA(l,nl)0^o	.E.0+..	S0$_1$(0)	−2.0	−5.0
NGC 5898*	(L)SA(l,nl)0$^-$	.E.0...	S0$_{2/3}$(0)	−3.0	−5.0
NGC 5953	SA(rs)a pec	.SA.1*P		1.0	1.0
NGC 5982	SA0$^-$	.E.3...	E3	−3.0	−5.0
NGC 6012	SB(x$_1$r,l)0$^+$	RSBR2*.		−1.0	2.0
NGC 6340*	(RL)SA(l,nl)0/a	.SAS0..	Sa(r)I	0.0	.0
NGC 6407[1]	E$^+$/SA0$^-$	.LA.0?P		−3.5	−2.0
NGC 6438*	S$\underline{\text{A}}$B(l)0$^-$	.RINGA.		−3.0	−2.0
NGC 6482[1]	E(d)2	.E...*.	E2	−5.0	−5.0
NGC 6646	(R′)SAB(rs)a:	.S..1..		1.0	1.0
NGC 6654[1]	(R′)SB$_a$(s,bl)a	PSBS0..		1.0	.0
NGC 6684*	(R′L)SAB(r$\underline{\text{s}}$,nb,bl)0/a	PLBS0..	SBa(s)	0.0	−2.0
NGC 6703*	(RL)SA(l)0^o	.LA.-..		−2.0	−2.5

Table 3 – *continued*

Galaxy (1)	Type (2.2 μm) (2)	Type (RC3) (3)	Type (RSA) (4)	T (2.2 μm) (5)	T (RC3) (6)
NGC 6782	(R)SAB(rl,nr′,nb,bl)0$^+$	RSXR1..	SBab(s)	−1.0	.8
NGC 6861*	E(d)5-6/SA0$^-$ sp	.LAS-*.	S0$_3$(6)	−4.0	−3.0
NGC 6958*	SA(l)0$^-$	.E+....	R?S0$_1$(3)	−3.0	−3.8
NGC 7029*	E(b)4/S0$^-$ sp	.E.6.*.	S0$_1$(5)	−4.0	−5.0
NGC 7049*	E3	.LAS0..	S0$_3$(4)/Sa	−5.0	−2.0
NGC 7079* [1]	(RL)SB$_a$(s:,bl)0$^+$	.LBS0..	SBa	−1.0	−2.0
NGC 7098*	(R′)SAB$_a$(l,nb)a	RSXT1..		1.0	1.0
NGC 7192*	(L)SA(l)0$^-$	.E+..*.	S0$_2$(0)	−3.0	−4.3
NGC 7213* [1]	SA(r,rl)0^o	.SAS1*.	Sa(rs)	−2.0	1.0
NGC 7217	(R′)SA(l,nl)0/a	RSAR2..	Sb(r)II-III	0.0	2.0
NGC 7332	SB$_x$0^o sp	.L...P/	S0$_{2/3}$(8)	−2.0	−2.0
NGC 7339	SA(s)bc sp	.SXS4*$		4.0	4.0
NGC 7371*	SA<u>B</u>(s)a	RSAR0*.	SBa(r)II	1.0	.0
NGC 7377*	SA(l)0$^-$	.LAS+..	S0$_{2/3}$/Sa pec	−3.0	−1.0
NGC 7457*	SA(s)0$^-$	.LAT-$.	S0$_1$(5)	−3.0	−3.0
NGC 7585*	SA:0/a pec shells/ripples	PLAS+P.	S0$_1$(3)/Sa	0.0	−1.0
NGC 7727*	SAB(s,nr)a pec	.SXS1P.	Sa pec	1.0	1.0
NGC 7742	(L)S<u>A</u>B(r$_1$,r$_2$)0/a	.SAR3..	Sa(r!)	0.0	3.0
NGC 7743*	SAB(s)a	RLBS+..	SBa	1.0	−1.0
NGC 7796* [1]	E$^+$1	.E+....	E1	−4.0	−3.8

*Forms part of the complete magnitude-limited NIRS0S sample.
[1]Photometric (based on decompositions, ELLIPSE fitting or unsharp masking) and visual classifications are not identical.

not have the resolution of the *Hubble Space Telescope*, they are still good enough for detecting nuclear bars, rings and lenses.

5.2 Visual classification

We use classification, based on de Vaucouleurs' revised Hubble–Sandage system (de Vaucouleurs 1959) (see also dVA and Buta 2011), which includes the *stage* (S0$^-$, S0^o, S0$^+$, Sa), *family* (SA, SAB, SB), *variety* (r, rs, s), *outer ring or pseudo-ring* (R, R′), possible *spindle* shape (sp, meaning edge-on or nearly-edge-on orientation), and the presence of *peculiarity* (pec). We use also a notation for shells and ripples. The underline notation (e.g. S<u>A</u>B, SA<u>B</u>,<u>r</u>s, r<u>s</u>) as used by de Vaucouleurs (1963) is used to emphasize the more likely phenomenon in a galaxy. Note that in the atlas images (in Fig. 5), for technical reasons, the underline notation is emphasized by slanted font instead. Following Buta & Crocker (1991) and Buta (1995), we also recognize subcategories of pseudo-rings (R$_1$, R$_1'$, R$_2'$, R$_1$R$_2'$). Representative examples of *stage* and *family* for barred and non-barred atlas galaxies are shown in Fig. 6. de Vaucouleurs' classification does not include the morphology of bars in terms of boxy/peanut/x-shaped structures (B$_x$), which is included in our classification. Bars can also have classical rectangular structures, or ansae at the two ends of the bar (Laurikainen et al. 2007; Martinez-Valpuesta, Knapen & Buta 2007), which ansae types are coded by B$_a$ in our classification. Examples of bar and ring morphologies in S0s are shown in Fig. 7. It is worth noting that the x-shaped structures inside the bars in our study, and in dVA, appear in fairly-face-on galaxies, not in edge-on systems where they are generally reported (see for example IC 5240 and NGC 4429 in Fig. 5).

Nuclear, inner and outer lenses are denoted by 'nl', 'l' and 'L', respectively. Nuclear bars and nuclear rings, denoted as 'nb' and 'nr', have similar sizes as nuclear lenses. In the classification, intermediate types between rings and lenses are also used (nrl, rl, RL). Additionally, a new lens type is introduced which we propose to call 'barlenses' with a notion of 'bl'. These appear in the central regions of many NIRS0S galaxies, but are generally distinct from nuclear lenses by their much larger sizes. From visual appearance, these 'bl' features can be mistaken for large bulges. The appearance of 'bl' is demonstrated for NGC 2983 in Fig. 8, where both the original and the residual images are shown: the residual image is created by subtracting from the original image the bulge+bar model obtained from 2D structural decomposition. A manifestation of 'bl' also appears in NGC 4314 (Fig. 9): the fine-structure in the central regions confirms that the component cannot be a bulge. Also, as the galaxy is in nearly-face-on orientation, the fat bar component cannot be interpreted as a boxy bar structure seen in nearly-edge-on orientation. This needs to be explained by the theoretical models, in which the boxy/peanut structures are generally induced by vertical thickening of the bar (Athanassoula & Misioritis 2002).

Due to our selection criteria, the sample should not contain edge-on galaxies. However, several misclassified galaxies appear in the RC3. We have moved the following galaxies in our sample to the spindle category: ESO 208−21, IC 1392, NGC 2685, 3414, 4220, 4435, 4474, 4546, 5087, 6861 and 7029. On the other hand, the galaxies NGC 4281 and 5353 which were classified as spindle in the RC3 are considered as more face-on systems in this work. Note that the galaxies NGC 4638, 5493 and 7029 have an edge-on disc clearly shorter than the outskirts of the IR spheroidal components, which have boxy outer isophotes (Fig. 5). We use the notation of Kormendy & Bender (1996) for the boxy elliptical parts of these galaxies with bright embedded S0 discs, although these galaxies do not fit very well to the scheme by Kormendy & Bender.

Our classification is similar to that used by Buta et al. (2010), except that lenses are coded in a systematic manner in this work. We have 12 galaxies in common with that sample. As expected, the agreement is generally good, except that in six of the galaxies we detect lenses [NGC 4203, Fig. 14 (shown later); NGC 4245, Fig. 5; NGC 4314, Fig. 9; NGC 4649, Fig. 5; NGC 5377, Fig. 7;

Table 4. Photometric classification, if not the same as visual classification in Table 3.

Galaxy (1)	Type (2.2 μm) (2)	T (2.2 μm) (3)
IC 4214	$(R_1)S\underline{A}B(\underline{r}l,nr,nb)0^+$	−1
IC 4991	$SA0^-$	−3
IC 5267	(RL)SA(l,nr)0/a	0
ESO 337−10	$SA0^-$	−3
NGC 0484	$SA(nb)0^-$	−3
NGC 0507	$(L)SAB(nb)0^-$	−3
NGC 1022	SAB(r'l,nb,bl)a	1
NGC 1079	$(RL)SAB_a(rs,nb,bl)0^+$	−1
NGC 1344	$SA(l)0^-$	−3
NGC 1350	$(R'_1)SAB_a(\underline{r}s,nb,bl)a$	1
NGC 1400	$SA0^-$	−3
NGC 2292	$SA0^-$	−3
NGC 2681	(RL)SAB(rs,ob,nr,nb)0/a	0
NGC 2782	SA(r,nr,nb)a pec	1
NGC 2902	$SA(\underline{r}l,nb)0^+$	−1
NGC 3166	$SA\underline{B}_a(\underline{r}l,nl,nb)a$	−1
NGC 3665	E2(d)	−5
NGC 3706	$SA(nd)0^o$	−2
NGC 3941	$(R'L)SB_a(s,bl,nb)0^o$	−2
NGC 3945	$(R)SB_a(rl,nl,nb,bl)0^+$	−1
NGC 4105	$SA0^-$	−3
NGC 4106	SAB(s,nl,nb)a	
NGC 4150	$(L)SA(l,nl,nr)0^-$	−3
NGC 4281	$SA0^-$	−3
NGC 4406	$SA0^-$	−3
NGC 4435	$SB0^o$ sp	−2
NGC 4459	$SA(l)0^-$	−3
NGC 4503	$S\underline{A}B(s,nd,bl)0^o$	−2
NGC 4552	$SA(l)0^-$	−3
NGC 4696	$S0^-$	−3
NGC 4754	$(L)SB_a(s,nb,bl)0^-$	−3
NGC 4976	$SA0^-$	−3
NGC 4984	$(R)SAB_a(l,nrl,nb)0^o$	−2
NGC 5273	$SA(s,l)0^o$	−2
NGC 5328	$(L)SAB(nl,bl,nb)0^o$	
NGC 5377	$(R_1)SA\underline{B}_x(rl,nl,nr)0/a$	0
NGC 5485	$SA(l)0^-$	−3
NGC 5631	$SA(l)0^-$	−3
NGC 6407	$SA0^-$	−3
NGC 6654	$(R')SB_a(s,nb,nl)a$	1
NGC 7079	$(RL)SB_a(s:,nb,bl)0^+$	−1
NGC 7213	$SA(r,rl,l)0^o$	−2
NGC 7796	$SA0^-$	−3

NGC 5846, Fig. 5], which were not recognized by Buta et al. Also, for NGC 5353 (Fig. 5) we recognize an x-shaped bar which was not included in the classification by Buta et al. On the other hand, for NGC 4369 (Fig. 5), Buta et al. detect an outer ring, which we do not see in the K_s-band image, most probably because the image used by us is not as deep as the *Spitzer* image at 3.6 μm of Buta et al.

Compared with the optical classification in the RC3, the Hubble stage differs for some individual galaxies. However, deviations appear in both directions, so that there is no systematic shift in the mean Hubble stage ($\langle T\rangle = -1.57$ and -1.51 in the near-IR and optical, respectively). The scatter plot of the optical and near-IR types is shown in Fig. 10. Both Eskridge et al. (2002) and Buta et al. (2010) found that intermediate-type (S0/a-Sc) galaxies are on average one stage earlier in the IR than in the optical. The reason why we do not see such a shift is partly because we study early-type galaxies which have only a small amount of dust, whereas the samples by Eskridge et al. and Buta et al. are more concentrated on dusty spirals. Another reason is that some of the galaxies in our sample were shifted towards an earlier stage, which is partly compensated by shifting some ellipticals that were misclassified in the RC3 into S0s in our classification.

5.3 Photometric classification

By photometric classification, we mean including faint structure components, even if they were not obvious in visual classification, for example, because they were outshone by luminous bulges. Also, galaxies that are late-type ellipticals (E^+) in visual classification can turn out to be early-type S0s in photometric classification if exponential outer discs are detected from surface brightness profiles. Our classification is based on morphology alone and does not include any kinematic observations or parameters measured from the images [ellipticities, bulge-to-total flux ratios (B/T) or bar strengths]. Also, no assumptions on the formative processes of galaxies were made, for example, by assigning features like shells/ripples, assumed to be merger-built structures, to elliptical galaxies alone. The photometric classification is given only if it deviates from the visual classification.

5.3.1 Subtle features not identified visually

In order to identify faint structures, we use (1) unsharp masks (see Section 4.1); or (2) residuals from structural decompositions. We use 2D multicomponent decompositions obtained previously for the atlas galaxies by Laurikainen et al. (2005, 2006, 2010). The decompositions were made by fitting a Sérsic function for the bulge, an exponential function for the disc and a Ferrers function for the bar. In some of the galaxies, more than one bar was fitted. Lenses were fitted either by Ferrers or Sérsic functions. Faint structures are visible in the residual images after subtracting a bulge model. Such structures can be bars, rings, inner discs or dust lanes. Lenses were identified directly from the images or from the surface brightness profiles: they were included to the parameter fitting of the structure components and therefore generally do not appear in the residual images.

The identification of lenses is an important part of our classification and the main lens types are shown in Fig. 11. For the galaxies in that figure, the structural decompositions are also shown, taken from Laurikainen et al. (2010). Prominent lenses, like the one in NGC 2902, are directly visible in the images. Faint or very extended lenses and ring/lens systems may not be immediately obvious in the images, but can be identified as broad bumps or exponential subsections in the surface brightness profiles (e.g. Laurikainen et al. 2010).

NGC 1533 (Fig. 11) is a good example of a galaxy having an outer ring/lens structure. In the surface brightness profile, it is manifested as a Sérsic profile with the n parameter smaller than 1. In NGC 2902 [see Figs 6 and 11], the inner ring/lens (rl) feature is manifested in a similar manner, causing a bump in the surface brightness profile. In NGC 524 [see Figs 11 and 15 (shown later)], the lenses are weaker and appear as exponential subsections in the surface brightness profile. NGC 524 is one of the best examples of a largely face-on (L)SA(l,nl) system, others being NGC 5846 (Fig. 5) and 5898 (see Fig. 5), with related examples being NGC 1411 (see Fig. 16 shown later) and 7192 (see Fig. 15 shown later). Our image of NGC 1411 is not deep enough to detect the outer lens, seen in the dVA image in the optical region. In the decomposition of NGC 524, the inner

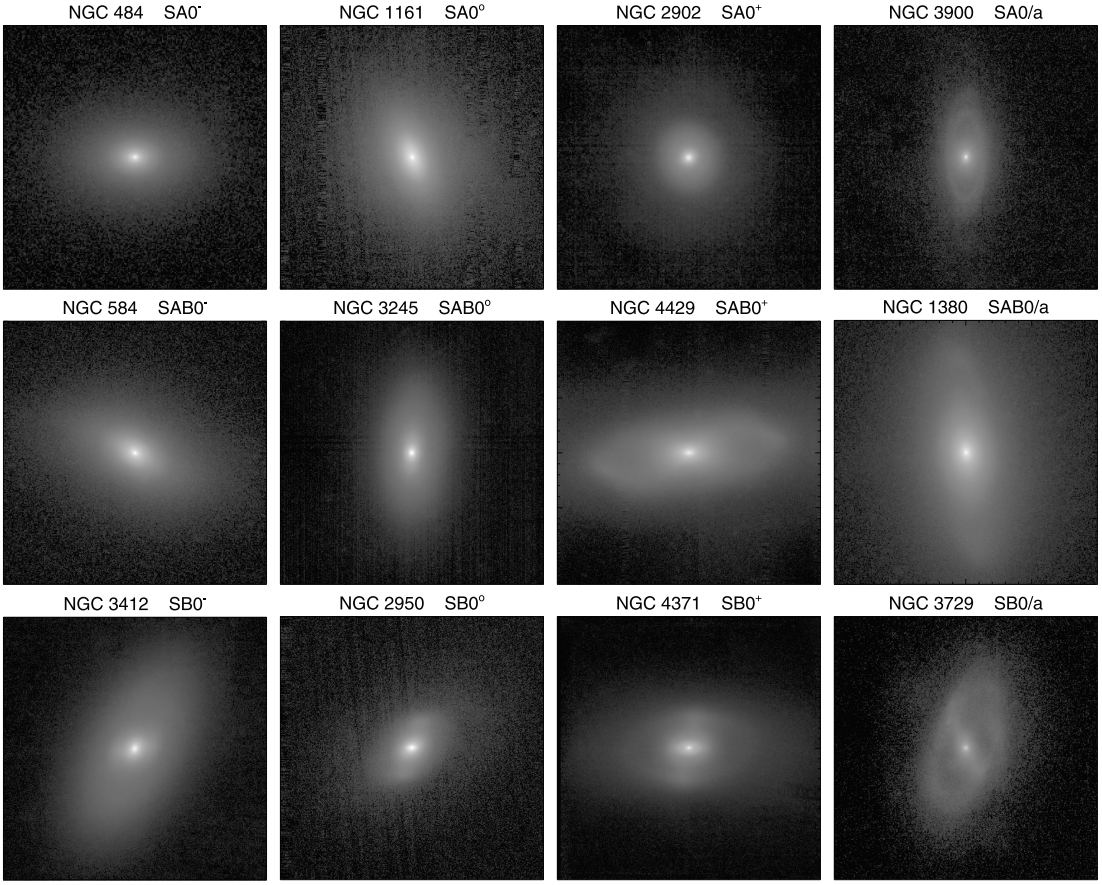

Figure 6. Examples of *stage* ($S0^-$, $S0^o$, $S0^+$) and *family* (A, SA, B) in the classification are shown. In this and in the following figures, the images are sky subtracted and they are shown in a magnitude scale.

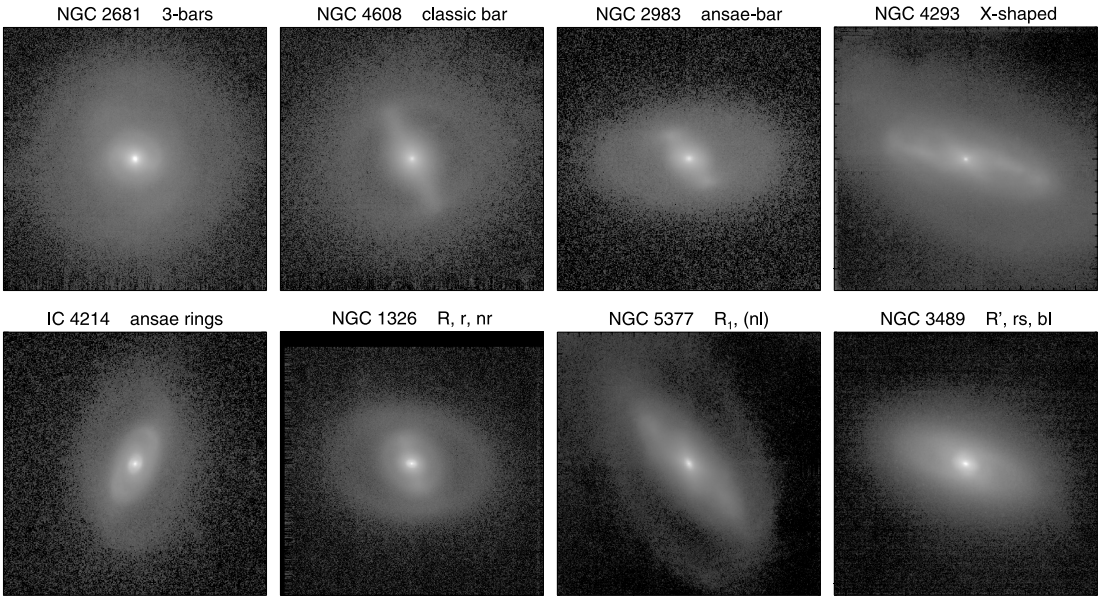

Figure 7. Examples of bars and rings. The left-hand upper panel (NGC 2681) shows an example of a galaxy having three bars. The largest bar is manifested as two weak ansae in the direction of 45° counter-clockwise from the north, whereas the main bar appears nearly horizontal. The nuclear bar is visible only in the atlas image shown in Fig. 5.

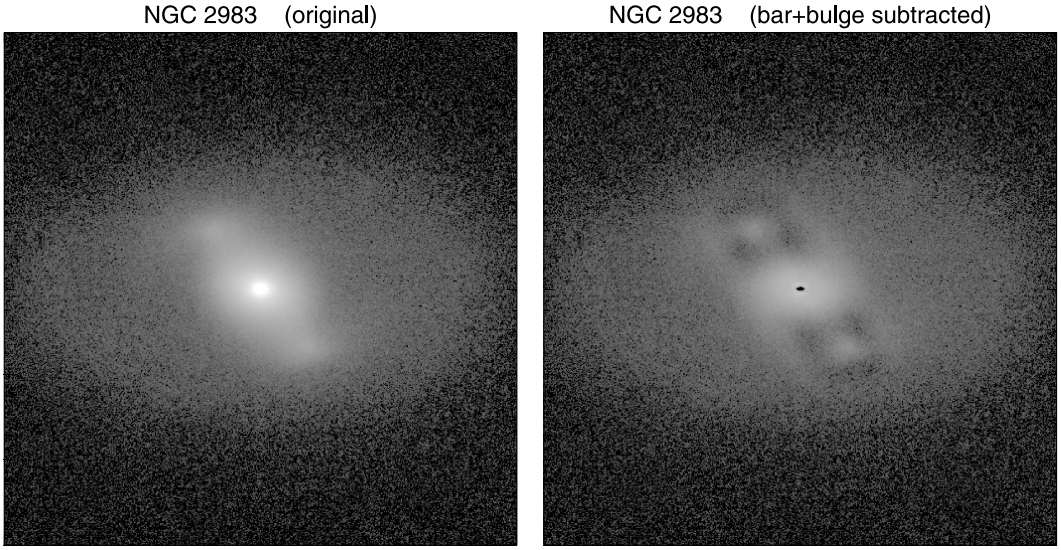

Figure 8. An illustration of barlens (bl) in NGC 2983. The left-hand panel shows the original image and the right-hand panel shows the residual image after subtracting the bar+bulge decomposition model taken from Laurikainen et al. (2010). Barlens is a nearly-spherical lens inside the bar. The two blops (=ansae) at the two ends of the bar are real, but the ring-like structure surrounding the bar is an artefact due to the fact that the bar model is only an approximation of the true surface brightness distribution of the bar.

(l) and nuclear (nl) lenses are fitted by Ferrers functions. NGC 2983 [Figs 11, 14 and 16 (shown later)] is an example of a barred galaxy having an outer lens (L), and also a barlens (bl).

In Fig. 12, images and structural decompositions are shown for NGC 4459 and 4696. In visual classification, these galaxies are ellipticals, but the surface brightness profiles show perfect exponential shapes, which changes the classification into S0. For these galaxies, we have also $B - K$ colour maps (Salo et al., in preparation), where the lenses can be identified as colour changes in the interface regions between lenses and discs.

In our classification, we do not code ovals as a distinct morphological feature, because they are often difficult to distinguish from lenses. Ovals are global deviations from an axisymmetric shape in galactic discs (see Kormendy & Kennicutt 2004; Buta 2011). In isophotal and Fourier analysis, they appear in a similar manner to bars (with higher Fourier modes, see Laurikainen et al. 2007), but with lower ellipticities. In contrast to lenses, they have less shallow surface brightness distributions.

5.3.2 Comparison with Kormendy et al. (2009)

We have five galaxies in common with the sample of Kormendy et al. (2009), who studied mainly ellipticals and Sph-type spheroidals, but whose sample also includes some bright S0s. The common galaxies are NGC 4382, 4472, 4552 and 4649 (Fig. 5), and NGC 4459 (Fig. 12), which were classified as ellipticals (mainly E2) by Kormendy et al., and as S0s by us. They are S0s in the classification by Sandage & Tammann (1981) also. For the last four galaxies, the decompositions by Laurikainen et al. (2010) have shown that the galaxies can be fitted by a Sérsic bulge and an exponential disc. In NGC 4649, a lens was also identified by us. Except for NGC 4459, Kormendy et al. report these galaxies as ellipticals that miss light in the nuclear regions.

NGC 4382 is peculiar and therefore difficult to classify. Kormendy et al. showed that the galaxy has extra light at intermediate radii above a single Sérsic fit, and also distorted isophotes. However, in their view, the extra light cannot be associated with a large-scale disc as is typical for S0s. The galaxy has shells/ripples, which is why Kormendy et al. interpreted it as a merger remnant that has not yet fully settled into an equilibrium. The reason why we consider it to be a disc galaxy and not an elliptical is the detection of dispersed spiral arm segments, but the exponential nature of the outer profile is not clear. However, there are other S0s with shells/ripples which do have clear extended exponential discs. Such galaxies are, for example, NGC 2782 and 7585 (Fig. 5).

6 DIMENSIONS OF THE STRUCTURES

The dimensions, orientations (PA) and minor-to-major-axis ratios (q) of the structure components, in our classification were measured and are given for rings and lenses in Table 5, and for bars in Table 6. The dimensions of the structure components are semi-major-axis lengths. To measure the rings and lenses, the following strategy was used: after displaying the image rebinned by a factor of 2, the classified features were mapped visually, at least three times in succession. If a feature was a clear ring, the cursor was used with the IRAF routine TVMARK to outline the ridge-line. If the feature was a lens, oval or a bar, the edge was mapped instead. After obtaining x, y coordinates of the feature's location mapped in azimuth, an ELLIPSE-fitting program was used to fit the points to get the central coordinates, the PA of the major-axis, the major- and minor-axis radii and the axial ratio. As an illustration of our strategy, the fitted ellipses for four features superimposed on the galaxy image are shown for NGC 1543 in Fig. 13. For this particular galaxy, the nuclear bar is also shown. Similar figures for the complete sample are available in electronic form at the NIRS0S website.[6] as Supporting Information with the online version of the article, and at http://cdsarc.u-strasbg.fr/cats.

For measuring bar lengths, three methods were used: (1) they were estimated visually by marking the outskirts of the bar and

[6] http://www.oulu.fi/astronomy/NIRS0S_pub/nirsos_dimensions.html

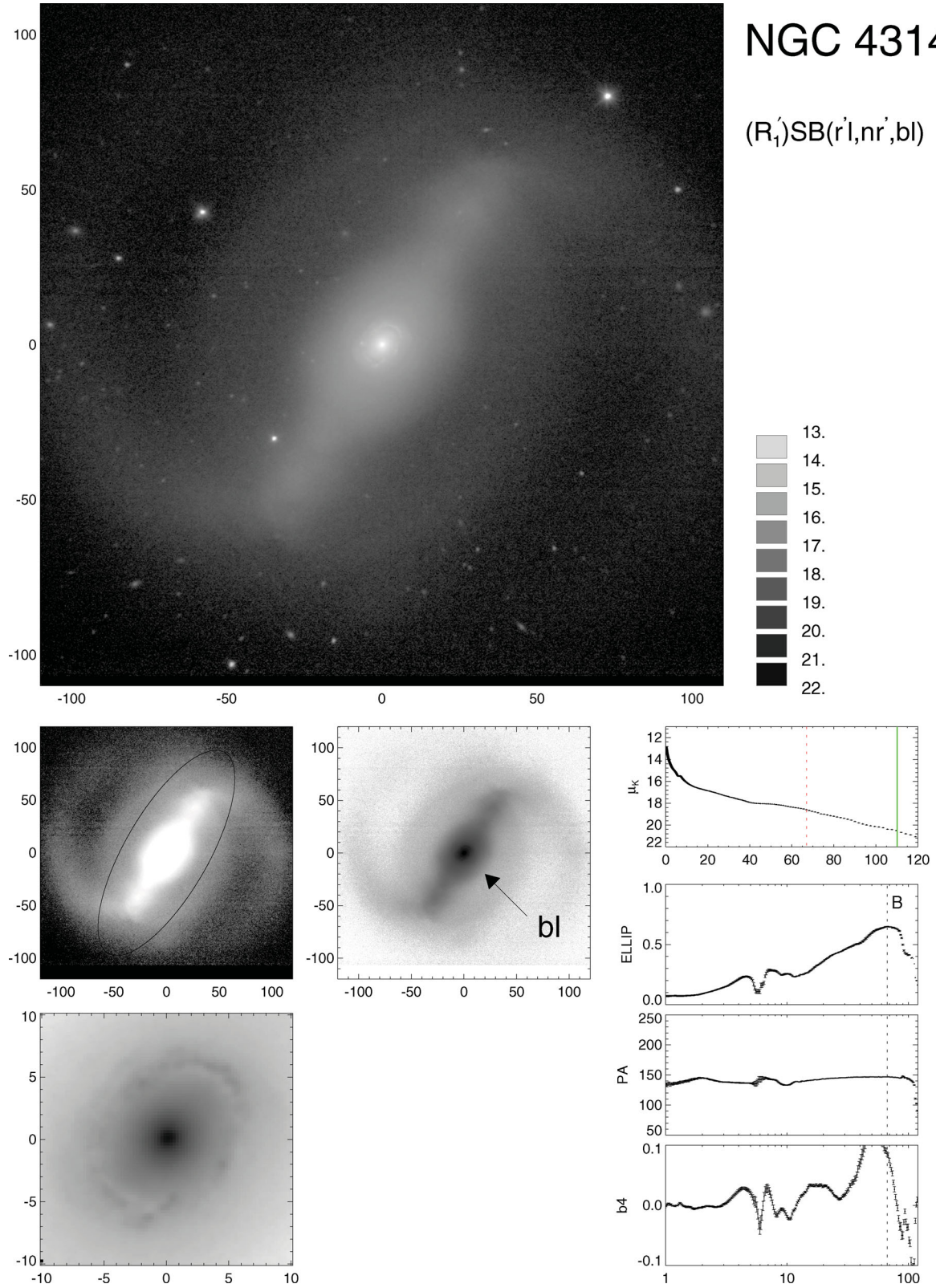

Figure 9. An illustration of barlens (bl) in an Sa-type spiral, NGC 4314. Barlens is a large component inside the bar, having a nuclear ring inside. The small panels are the same as in Fig. 5.

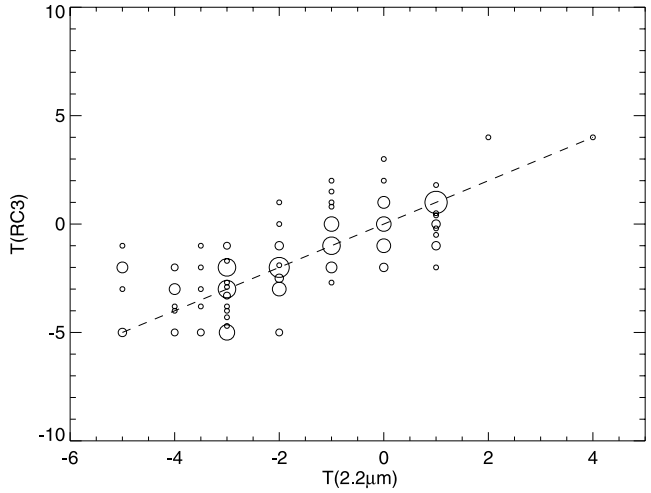

Figure 10. The scatter plot of the optical and the near-IR classifications, taken from RC3 and this study, respectively. The size of the symbol indicates the number of galaxies represented by the symbol. The dashed line corresponds to $T(\mathrm{RC3}) = T(2.2\ \mu\mathrm{m})$.

drawing an ellipsoid to that distance ($r_{\rm vis}$ in Table 6). A line was also drawn along the bar major-axis which gave a visual estimate of the bar orientation; (2) radial profiles of the ellipticities were used: bar length was taken to be the radial distance where the maximum ellipticity in the bar region appeared (following e.g. Wozniak & Pierce 1991; Wozniak et al. 1995; $r_{\rm ell}$ in Table 6); and (3) as a third estimate, the bar length was taken to be (Erwin & Sparke 2003)

$$r_{\rm L} = r_{\rm ell} + (r_{\rm ellmin} - r_{\rm ell})/2,$$

where $r_{\rm ellmin}$ is the radial distance where the first minimum appears after the ellipticity maximum in the bar region. In galaxies with complicated morphological structures, no minimum appears after the maximum ellipticity; in those cases, no $r_{\rm L}$ is given. $r_{\rm ell}$ was not given if the ellipticity maximum was very broad and also when the bar orientation in respect of the disc orientation was not favourable. This is the case, for example, for NGC 3384 (Figs 5 and 13 in electronic form) having a bar, which is also inside a lens, perpendicular to the disc. As a consequence, there is a minimum in the ellipticity profile and in the *b*4 profile at the edge of the bar, and a maximum in the PA (which also means that the method based on detecting maxima in the ellipticity profile misses bars in unfavourable orientation). Another similar case is NGC 4546 (Fig. 5, electronic Fig. 13). If the bars are very weak and appear only in the unsharp masks or in the residual images, only visual estimation of the length can be given. Typically, $r_{\rm vis}$ is close to $r_{\rm ell}$, whereas $r_{\rm L}$ gives an upper limit for bar length. The standard deviations given in column 7 of Table 6 were calculated for $r_{\rm vis}$ and $r_{\rm ell}$. The bar orientation is generally the PA near the ellipticity maximum in the bar region, but for very weak bars, bars seen inside prominent lenses or in unfavourable viewing angle, the PA from ellipse fitting could not be used. For those galaxies, visually estimated bar orientation is given. Visually estimated orientation and those obtained from ellipse fitting generally agree well, the variations typically being around 2°.

7 DISCUSSION

It has been suggested that galactic discs are primary components of galaxy formation and that their surface brightness distribution reflects the specific angular momentum distribution of protogalaxies (e.g. Fall & Efstathiou 1980; Dutton & van den Bosch 2009). There can also be angular momentum exchange between materials at different radii, in which case the exponential surface brightness distribution is a result of disc viscosity (Lin & Pringle 1987). Bosma (1983) suggested that lenses might be primary components formed soon after the disc formation: the outer edges of lenses may have formed when the initial amount of gas suddenly dropped and star formation abruptly ceased. Lenses may also form by disc instabilities in a similar manner to bars (Athanassoula & Sellwood 1983).

On the other hand, in the hierarchical picture of galaxy formation, present-day galactic discs are merger-built structures, which have been significantly restructured in galaxy collisions (White & Rees 1978; Kauffmann et al. 1999). It has been suggested that even up to ∼50 per cent of all spiral discs might come from disc rebuilding from recent mergers, the other half of the discs being formed in some earlier mergers (Hammer et al. 2009). If S0s are descendants of these spirals, it needs to be understood how the multicomponent bar/lens structures that we find in up to 25 per cent of the S0s were formed and maintained. The statistics and a more thorough discussion of possible formative processes of lenses will appear in forthcoming papers. Here we give only tentative examples of possible morphological sequences of lens formation and discuss possible candidates of $S0_c$ galaxies.

7.1 Morphological evidence of lens formation?

1. *Lenses might be highly evolved star-forming zones or highly evolved stellar rings* (Fig. 14a). The upper panels show the full images, whereas the lower panels show the inner regions of the residual images, obtained after subtracting the bulge models from the original images, for NGC 3998 and 4203. In this scenario, gas is used by star formation in the disc, leading to a dynamical heating so that the spiral arms disappear, first in the outer disc (NGC 7371). However, in the presence of a weak bar, some of the material in the spiral arms may be trapped into the resonances of the bar before all the gas is consumed. Consequently, a ring or a double ring may form outside the bar (NGC 3998). When the rest of the gas is consumed and the inner disc is dynamically heated, the rings are expected to lose their identity and a lens forms (NGC 4203). Note that in NGC 4203 the lens clearly has a larger radius than the bar. In Laurikainen et al. (2009), NGC 3998 was interpreted as a possible candidate of bar destruction in a spiral galaxy that was formerly barred.

2. The sequence NGC 5953 -> NGC 7742 -> NGC 7213 (Fig. 14b) is *similar to the sequence above, except that the galaxies have no bars*. NGC 5953 has prominent flocculent spiral arms in the inner part of the disc. If there is enough gas in these spiral arms, a starburst may occur, leading to a rapid increase in the stellar mass, which may take the form of a lens with the dimension of the current extension of the spiral arms. As an intermediate stage, the spirals may take the form of rings, which is clear in NGC 7742 (the ring in this galaxy is counter-rotating; de Zeeuw et al. 2002) and to some extent also in NGC 7213.

3. *Lenses might be triggered by bars*, which is illustrated in Fig. 14(c). Bars are known to excite resonance rings, which can be full classical rings or R′-type rings, of which NGC 6654 is a good example. When the gas is consumed, the disc is dynamically heated, and the ring in NGC 6654 may evolve into a lens, similar to that surrounding the bar of NGC 2983. An alternative progenitor type of NGC 2983 could be NGC 1326 (see Fig. 7), which has a

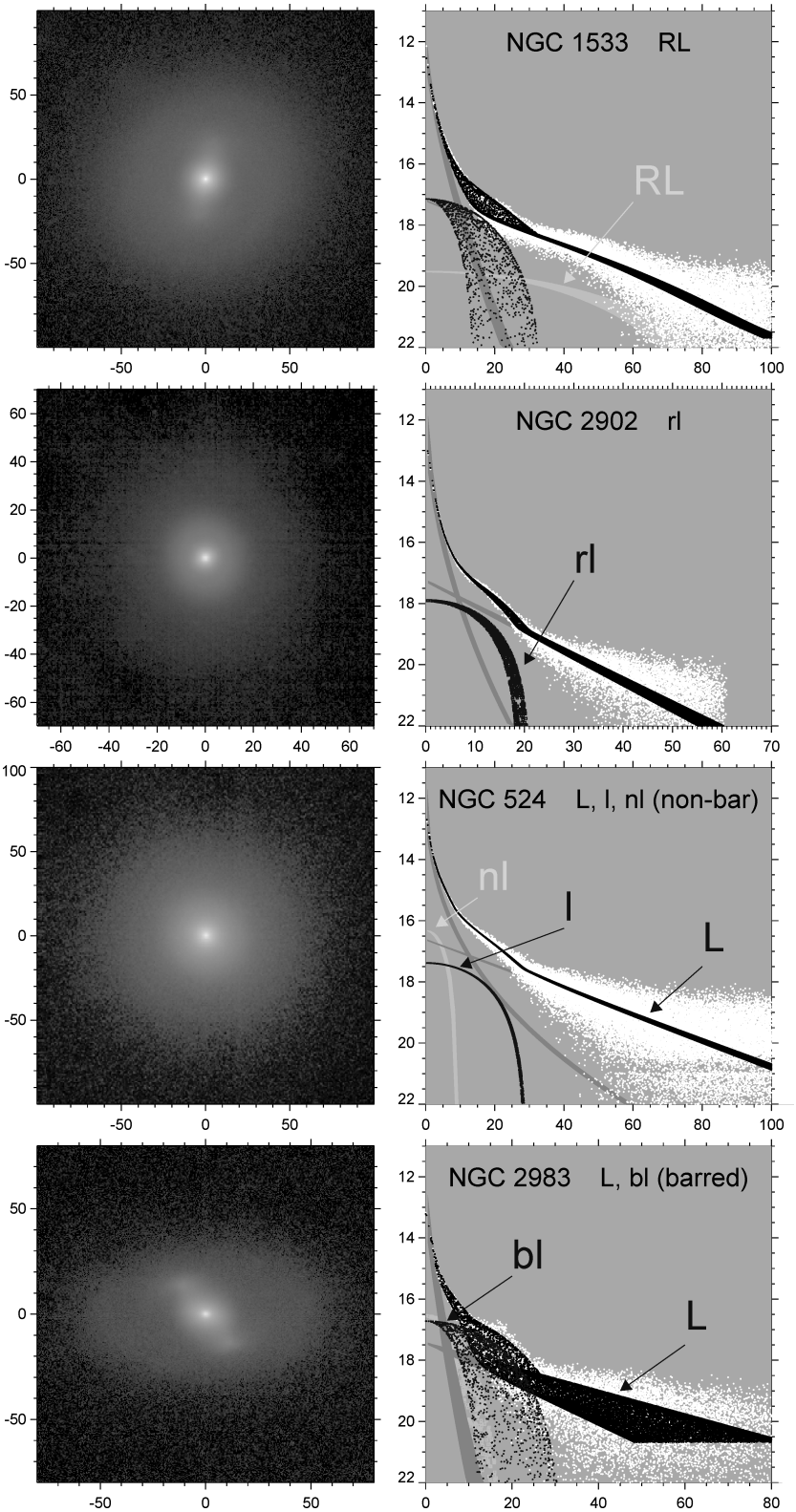

Figure 11. Examples of different type of lenses. The left-hand panels show the images and the right-hand panels show the 2D multicomponent decompositions from Laurikainen et al. (2010), explained in more detail in the text. In the decomposition plots, the white dots show the data points of the 2D surface brightness distribution (brightness of each pixel as a function of the sky-plane radius from the galaxy centre), and the black and grey colours show the model components. The uppermost black dots show the total model.

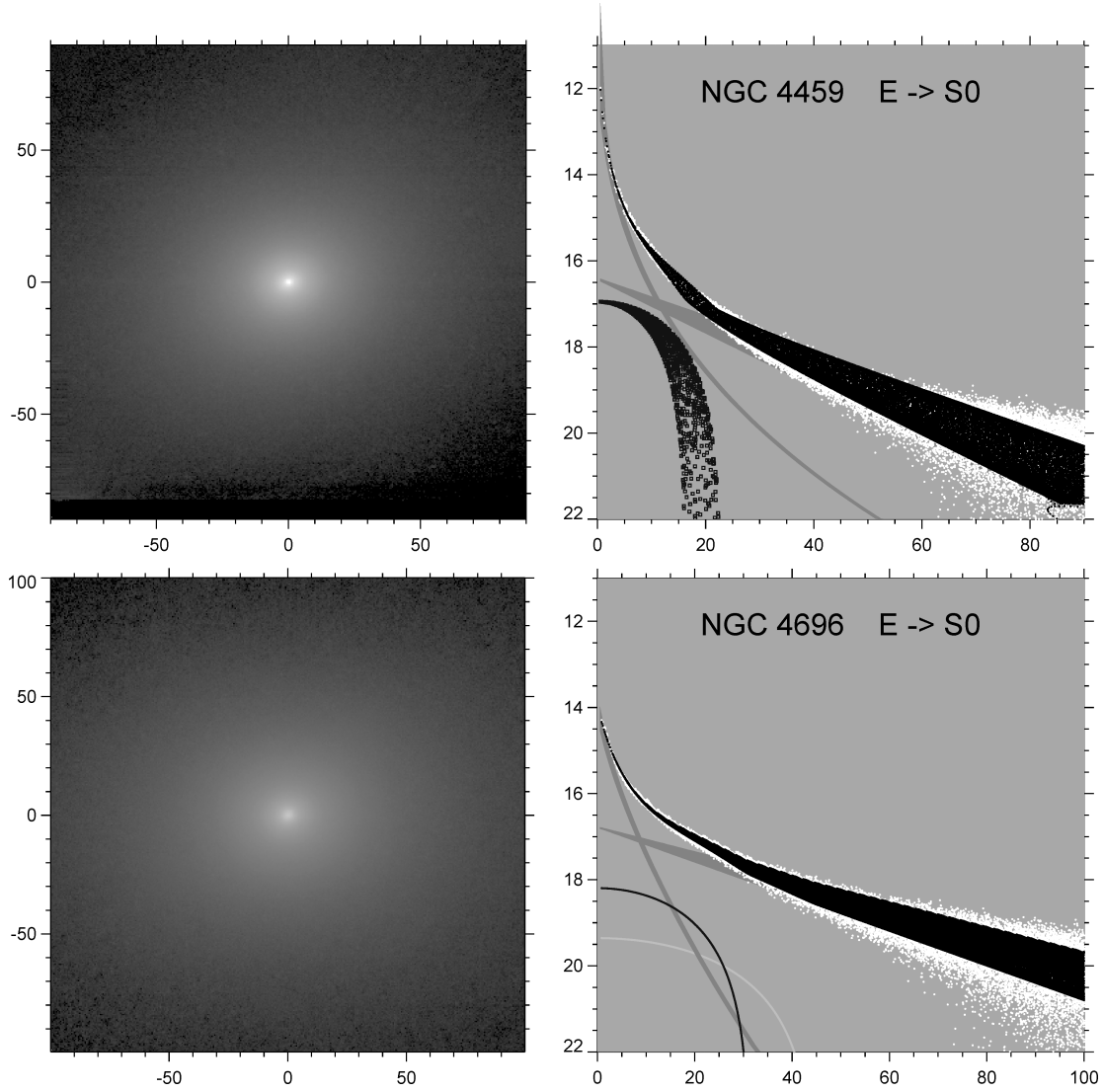

Figure 12. Two examples in which photometric classification moves an elliptical galaxy to an S0 stage. Both galaxies have exponential outer surface brightness profiles, and also evidence of lenses, manifested as exponential subsections in the brightness profile. In the decomposition plots, the meaning of the dots and lines is the same as in Fig. 10.

prominent dispersed ring surrounding the bar. When evolved over time, the ring may evolve into a lens.

Several stripping mechanisms in spiral galaxies are suggested leading to significant decay of star formation and heating of the disc, which is required while transferring spiral galaxies into S0s. According to numerical simulations (Bekki & Couch 2011), reduced star formation is particularly important among barred interacting galaxies: galaxy interactions trigger gas infall in the bar, leading to repetitive starbursts in the spiral galaxy disc, followed by subsequent fading. However, there exist also non-barred S0s having significant star formation in their inner rings, of which NGC 4138 is an example (Pogge & Eskridge 1993; see also Grouchy et al. 2010). It is possible that galaxy interactions/mergers play an important role also in the formation of these galaxies, in the sense that gas-rich small companions might be swallowed by the more massive spiral galaxies. If the galaxy had an inner ring, the gas might have fallen into the potential well of the ring leading to a starburst in the ring. NGC 4138 has also a counter-rotating component (Jore, Broeils & Haynes 1996; see also discussion in Comerón et al. 2010), which supports the merger hypothesis, or alternatively, star-forming rings were formed in a process, where vertical satellite collision triggers the star-forming ring (Mapelli et al. 2008).

7.2 Prototypical multiple bar/lens structures

The galaxies NGC 1543, 6782 and 3081 are *prototypical examples of double barred galaxies* (Fig. 15a). The scales in the upper panels are selected to illustrate the main bars and lenses, whereas the lower panels show the nuclear bars and lenses in the same galaxies. NGC 1543 has two bars and lenses surrounding the bars, extending to the same radius as the bar. Intuitively, it seems plausible that the lenses were triggered by the bars. NGC 6782 also has two bars; a ring/lens surrounds the main bar and a nuclear ring surrounds the nuclear bar. It is possible that the galaxy also has a weak lens inside the nuclear ring, but that is difficult to verify. NGC 3081 has two weak bars, but in this galaxy, the nuclear and inner rings at the outskirts of the two bars are the dominant features. NGC 1317

Table 5. Ring and lens dimensions.

Galaxy	Feature type	Major-axis radius (arcsec)	q	PA (°)
(1)	(2)	(3)	(4)	(5)
IC 4214	R_1	59.3 ± 0.04	0.590 ± .001	179.8 ± 0.06
IC 4214	rl	28.1 ± 0.04	0.483 ± .001	159.9 ± 0.05
IC 4214	nr	6.4 ± 0.01	0.674 ± .001	156.6 ± 0.15
IC 5240	r	38.9 ± 0.03	0.651 ± .001	107.0 ± 0.06
IC 5267	l	44.7 ± 0.10	0.740 ± .002	142.3 ± 0.20
IC 5267	RL	78.0 ± 0.05	0.771 ± .001	134.6 ± 0.07
IC 5328	l	18.5 ± 0.09	0.817 ± .005	41.0 ± 0.74
NGC 0474	RL	66.6 ± 0.13	0.944 ± .002	7.6 ± 1.40
NGC 0507	L	39.4 ± 0.10	0.865 ± .003	43.2 ± 0.57
NGC 0524	l	24.8 ± 0.10	0.963 ± .005	36.4 ± 3.83
NGC 0524	nl	6.5 ± 0.02	0.962 ± .004	41.7 ± 2.78
NGC 0524	L	57.1 ± 0.12	0.988 ± .003	165.5 ± 7.48
NGC 0584	l	17.5 ± 0.22	0.583 ± .008	57.4 ± 0.56
NGC 0718	rs	19.9 ± 0.11	0.630 ± .004	147.1 ± 0.34
NGC 0718	R′	43.2 ± 0.24	0.783 ± .005	28.0 ± 0.75
NGC 0718	nl	3.1 ± 0.01	0.914 ± .005	17.5 ± 1.64
NGC 0936	bl	25.0 ± 0.08	0.845 ± .003	142.2 ± 0.58
NGC 0936	rs	45.2 ± 0.06	0.786 ± .001	129.4 ± 0.16
NGC 1022	r′l	27.8 ± 0.06	0.861 ± .002	35.3 ± 0.50
NGC 1022	bl	9.1 ± 0.06	0.772 ± .006	131.2 ± 0.72
NGC 1079	rs	41.6 ± 0.08	0.560 ± .001	86.9 ± 0.14
NGC 1079	bl	17.5 ± 0.04	0.694 ± .002	91.4 ± 0.26
NGC 1079	RL	111.8 ± 0.11	0.583 ± .001	78.6 ± 0.06
NGC 1161	l	9.8 ± 0.01	0.577 ± .001	20.5 ± 0.06
NGC 1201	bl	16.8 ± 0.03	0.700 ± .002	5.9 ± 0.19
NGC 1201	r′l	32.8 ± 0.06	0.595 ± .001	12.2 ± 0.14
NGC 1302	rl	34.0 ± 0.05	0.968 ± .002	65.2 ± 1.95
NGC 1317	nr_1	12.3 ± 0.01	0.834 ± .001	57.1 ± 0.15
NGC 1317	nr_2	15.2 ± 0.01	0.930 ± .001	144.1 ± 0.25
NGC 1317	nl	6.7 ± 0.01	0.905 ± .002	67.5 ± 0.53
NGC 1317	r′l	58.0 ± 0.03	0.950 ± .001	81.6 ± 0.48
NGC 1326	nr	5.7 ± 0.01	0.743 ± .001	84.6 ± 0.15
NGC 1326	r	33.5 ± 0.03	0.807 ± .001	38.8 ± 0.14
NGC 1326	R	84.5 ± 0.03	0.645 ± .000	83.4 ± 0.04
NGC 1326	bl	20.2 ± 0.02	0.830 ± .001	67.0 ± 0.21
NGC 1350	rs	65.9 ± 0.06	0.542 ± .001	18.9 ± 0.04
NGC 1350	R′	157.9 ± 0.07	0.501 ± .000	0.2 ± 0.03
NGC 1350	bl	32.0 ± 0.07	0.626 ± .002	9.1 ± 0.19
NGC 1371	l	92.9 ± 0.11	0.669 ± .001	128.4 ± 0.07
NGC 1371	RL	129.8 ± 0.14	0.633 ± .001	133.3 ± 0.05
NGC 1371	rs	38.0 ± 0.08	0.696 ± .002	121.0 ± 0.17
NGC 1387	nrl	8.3 ± 0.01	0.986 ± .001	43.4 ± 2.04
NGC 1389	l	18.8 ± 0.02	0.765 ± .001	11.2 ± 0.17
NGC 1411	nl	12.3 ± 0.02	0.784 ± .001	9.4 ± 0.23
NGC 1411	l	46.1 ± 0.05	0.670 ± .001	6.3 ± 0.10
NGC 1415	nr	5.9 ± 0.03	0.404 ± .002	150.1 ± 0.08
NGC 1415	r′l	47.9 ± 0.22	0.399 ± .002	145.1 ± 0.07
NGC 1415	RL	91.8 ± 0.50	0.508 ± .003	145.0 ± 0.16
NGC 1440	L	43.7 ± 0.03	0.753 ± .001	19.9 ± 0.10
NGC 1440	rs	24.7 ± 0.07	0.765 ± .002	33.8 ± 0.32
NGC 1440	bl	10.0 ± 0.02	0.804 ± .002	48.4 ± 0.29
NGC 1452	r	48.7 ± 0.04	0.596 ± .001	109.7 ± 0.05
NGC 1452	bl	18.3 ± 0.01	0.887 ± .001	103.2 ± 0.32
NGC 1452	R′	76.8 ± 0.14	0.554 ± .001	114.2 ± 0.09
NGC 1512	nr	8.3 ± 0.01	0.784 ± .001	79.4 ± 0.15
NGC 1512	rs	71.0 ± 0.12	0.820 ± .002	53.4 ± 0.28
NGC 1512	bl	41.3 ± 0.13	0.626 ± .002	52.9 ± 0.17
NGC 1533	RL	56.9 ± 0.05	0.870 ± .001	134.0 ± 0.20
NGC 1533	bl	14.7 ± 0.02	0.962 ± .002	78.9 ± 1.59
NGC 1537	rl	7.9 ± 0.02	0.511 ± .001	81.1 ± 0.13
NGC 1543	R	159.9 ± 0.12	0.942 ± .001	2.9 ± 0.60

Table 5 – *continued*

Galaxy	Feature type	Major-axis radius (arcsec)	q	PA (°)
(1)	(2)	(3)	(4)	(5)
NGC 1543	l	92.7 ± 0.07	0.753 ± .001	100.2 ± 0.12
NGC 1543	nl	10.7 ± 0.01	0.955 ± .001	99.1 ± 1.04
NGC 1553	rl	36.4 ± 0.03	0.577 ± .001	150.4 ± 0.04
NGC 1553	nl	8.5 ± 0.02	0.604 ± .002	153.0 ± 0.16
NGC 1574	L	108.7 ± 0.03	0.979 ± .000	66.2 ± 0.61
NGC 1574	l	22.1 ± 0.03	0.991 ± .002	29.8 ± 6.00
NGC 1617	R′	95.8 ± 0.19	0.467 ± .001	108.9 ± 0.07
NGC 1617	rs	60.0 ± 0.34	0.411 ± .003	106.3 ± 0.20
NGC 2196	l	23.7 ± 0.07	0.734 ± .002	45.1 ± 0.24
NGC 2217	R	96.9 ± 0.07	0.884 ± .001	22.8 ± 0.22
NGC 2217	$\underline{\text{rs}}$	42.6 ± 0.04	0.898 ± .001	127.7 ± 0.30
NGC 2217	nl	9.1 ± 0.02	0.994 ± .003	59.4 ± 16.55
NGC 2273	R	61.4 ± 0.12	0.528 ± .001	56.4 ± 0.06
NGC 2273	rs	21.0 ± 0.02	0.792 ± .001	81.9 ± 0.14
NGC 2273	bl	12.4 ± 0.02	0.878 ± .002	71.4 ± 0.49
NGC 2293	bl	17.3 ± 0.02	0.794 ± .001	89.6 ± 0.23
NGC 2300	R′L	48.3 ± 0.05	0.898 ± .001	65.3 ± 0.35
NGC 2380	l	24.7 ± 0.04	0.964 ± .002	98.1 ± 2.07
NGC 2380	nl	8.4 ± 0.02	0.967 ± .004	85.7 ± 3.92
NGC 2460	rs	8.1 ± 0.02	0.703 ± .002	11.4 ± 0.27
NGC 2523	r	28.9 ± 0.03	0.763 ± .001	61.0 ± 0.11
NGC 2681	$\underline{\text{rs}}$	18.7 ± 0.02	0.957 ± .001	79.8 ± 0.86
NGC 2681	RL	77.1 ± 0.05	0.945 ± .001	100.8 ± 0.54
NGC 2681	ob	41.9 ± 0.06	0.798 ± .001	34.1 ± 0.20
NGC 2781	RL	87.4 ± 0.17	0.470 ± .001	73.3 ± 0.07
NGC 2781	rl	32.7 ± 0.03	0.468 ± .000	78.9 ± 0.04
NGC 2781	nr	7.4 ± 0.01	0.578 ± .001	75.5 ± 0.13
NGC 2782	r	29.8 ± 0.03	0.972 ± .001	77.9 ± 1.35
NGC 2782	nr	5.6 ± 0.01	0.464 ± .001	87.7 ± 0.11
NGC 2787	nrl	45.5 ± 0.08	0.531 ± .001	104.8 ± 0.09
NGC 2787	bl	21.3 ± 0.06	0.507 ± .002	106.3 ± 0.14
NGC 2859	R	107.9 ± 0.13	0.701 ± .001	83.2 ± 0.15
NGC 2859	$\underline{\text{rl}}$	39.3 ± 0.03	0.875 ± .001	84.8 ± 0.28
NGC 2859	nl	6.7 ± 0.01	0.946 ± .002	82.8 ± 1.52
NGC 2859	bl	20.6 ± 0.02	0.974 ± .001	110.3 ± 1.56
NGC 2880	r	13.6 ± 0.05	0.622 ± .003	149.0 ± 0.20
NGC 2902	$\underline{\text{rl}}$	13.8 ± 0.02	0.924 ± .001	9.4 ± 0.70
NGC 2950	l	35.6 ± 0.09	0.630 ± .002	126.6 ± 0.13
NGC 2950	nrl	5.2 ± 0.02	0.693 ± .003	130.8 ± 0.28
NGC 2983	L	51.7 ± 0.04	0.598 ± .001	88.4 ± 0.06
NGC 2983	bl	14.4 ± 0.02	0.747 ± .002	89.6 ± 0.26
NGC 3032	rl_1	8.4 ± 0.01	0.900 ± .002	80.5 ± 0.55
NGC 3032	rl_2	17.0 ± 0.01	0.886 ± .001	101.3 ± 0.25
NGC 3081	R_1	71.5 ± 0.07	0.813 ± .001	128.2 ± 0.14
NGC 3081	r	33.0 ± 0.02	0.687 ± .001	72.5 ± 0.06
NGC 3081	nr	6.0 ± 0.01	0.750 ± .002	104.4 ± 0.26
NGC 3166	$\underline{\text{rl}}$	29.9 ± 0.03	0.671 ± .001	89.9 ± 0.13
NGC 3166	nl	5.9 ± 0.03	0.504 ± .003	87.6 ± 0.27
NGC 3245	L	59.2 ± 0.07	0.514 ± .001	177.4 ± 0.07
NGC 3245	rs	15.3 ± 0.03	0.481 ± .001	177.8 ± 0.08
NGC 3245	nl	6.0 ± 0.01	0.636 ± .002	175.6 ± 0.17
NGC 3358	R_2'	87.7 ± 0.20	0.486 ± .001	139.4 ± 0.05
NGC 3358	rl	24.8 ± 0.08	0.540 ± .002	139.5 ± 0.10
NGC 3384	L	115.4 ± 0.13	0.483 ± .001	51.8 ± 0.03
NGC 3384	l	19.9 ± 0.02	0.905 ± .001	51.6 ± 0.41
NGC 3384	bl	9.5 ± 0.01	0.863 ± .001	49.9 ± 0.25
NGC 3412	L	77.2 ± 0.18	0.518 ± .001	147.4 ± 0.07
NGC 3489	RL	55.4 ± 0.14	0.348 ± .001	69.2 ± 0.05
NGC 3489	r	20.2 ± 0.03	0.721 ± .001	62.8 ± 0.15
NGC 3489	bl	11.9 ± 0.08	0.546 ± .004	79.3 ± 0.37
NGC 3516	R	29.0 ± 0.03	0.753 ± .001	56.9 ± 0.13

Table 5 – *continued*

Galaxy	Feature type	Major-axis radius (arcsec)	q	PA (°)
(1)	(2)	(3)	(4)	(5)
NGC 3516	l	16.8 ± 0.02	0.829 ± .001	25.7 ± 0.19
NGC 3607	L	49.4 ± 0.07	0.962 ± .002	117.8 ± 1.52
NGC 3626	R	44.5 ± 0.04	0.666 ± .001	151.8 ± 0.07
NGC 3626	rl	18.6 ± 0.04	0.610 ± .002	172.9 ± 0.17
NGC 3626	nrl	4.1 ± 0.02	0.905 ± .006	161.5 ± 2.01
NGC 3718	rs	88.4 ± 0.11	0.736 ± .001	156.0 ± 0.14
NGC 3718	l	60.8 ± 0.07	0.823 ± .001	168.2 ± 0.27
NGC 3718	nl	14.6 ± 0.02	0.973 ± .002	119.1 ± 2.14
NGC 3729	r	38.3 ± 0.13	0.462 ± .002	159.8 ± 0.12
NGC 3892	L	83.1 ± 0.04	0.922 ± .001	27.8 ± 0.23
NGC 3892	rs	37.6 ± 0.04	0.800 ± .001	95.3 ± 0.22
NGC 3900	r	32.2 ± 0.03	0.402 ± .000	178.0 ± 0.04
NGC 3941	R′L	44.9 ± 0.07	0.599 ± .001	7.3 ± 0.11
NGC 3941	bl	18.1 ± 0.07	0.659 ± .003	5.5 ± 0.35
NGC 3945	R	121.2 ± 0.11	0.569 ± .001	160.0 ± 0.05
NGC 3945	rl	46.4 ± 0.05	0.680 ± .001	157.3 ± 0.08
NGC 3945	bl	25.6 ± 0.02	0.917 ± .001	157.3 ± 0.42
NGC 3945	nl	11.5 ± 0.03	0.555 ± .002	156.2 ± 0.14
NGC 3998	rl	37.3 ± 0.06	0.826 ± .002	125.6 ± 0.27
NGC 4106	nl	6.5 ± 0.01	0.831 ± .002	84.2 ± 0.48
NGC 4138	r	20.8 ± 0.03	0.574 ± .001	153.7 ± 0.07
NGC 4143	L	63.7 ± 0.13	0.592 ± .001	144.6 ± 0.09
NGC 4143	R′L	39.0 ± 0.22	0.466 ± .003	145.3 ± 0.13
NGC 4143	bl	6.2 ± 0.01	0.771 ± .002	145.0 ± 0.25
NGC 4150	L	36.5 ± 0.13	0.627 ± .002	144.3 ± 0.18
NGC 4150	nl	3.0 ± 0.02	0.794 ± .005	143.4 ± 0.72
NGC 4203	l	20.8 ± 0.08	0.879 ± .004	1.6 ± 1.26
NGC 4203	L	70.7 ± 0.08	0.978 ± .002	30.5 ± 2.04
NGC 4203	rl	33.3 ± 0.04	0.974 ± .002	35.9 ± 1.89
NGC 4203	R′L	57.5 ± 0.05	0.807 ± .001	6.7 ± 0.17
NGC 4220	RL	85.9 ± 0.75	0.313 ± .003	138.2 ± 0.06
NGC 4220	r	33.3 ± 0.51	0.216 ± .003	137.8 ± 0.05
NGC 4245	RL	84.3 ± 0.08	0.772 ± .001	0.7 ± 0.16
NGC 4245	r	36.9 ± 0.04	0.749 ± .001	152.4 ± 0.13
NGC 4245	nr	4.6 ± 0.01	0.766 ± .002	174.9 ± 0.28
NGC 4245	bl	18.7 ± 0.04	0.775 ± .002	154.2 ± 0.27
NGC 4262	OOL	49.9 ± 0.02	0.861 ± .000	133.3 ± 0.09
NGC 4262	IOL	29.6 ± 0.02	0.841 ± .001	142.2 ± 0.12
NGC 4262	nl	3.7 ± 0.02	0.773 ± .005	149.4 ± 0.72
NGC 4262	bl	8.5 ± 0.03	0.941 ± .004	117.3 ± 2.16
NGC 4267	L	83.8 ± 0.06	0.949 ± .001	124.1 ± 0.54
NGC 4293	RL	124.4 ± 0.14	0.549 ± .001	64.1 ± 0.05
NGC 4314	R'_1	108.5 ± 0.07	0.858 ± .001	67.5 ± 0.16
NGC 4314	r′l	66.4 ± 0.11	0.786 ± .002	159.3 ± 0.27
NGC 4314	bl	30.4 ± 0.04	0.797 ± .001	145.9 ± 0.16
NGC 4314	nr’	7.1 ± 0.01	0.719 ± .002	135.6 ± 0.16
NGC 4339	l	16.7 ± 0.03	0.910 ± .002	20.7 ± 0.86
NGC 4339	r	27.9 ± 0.04	0.917 ± .002	21.6 ± 0.64
NGC 4340	r	65.9 ± 0.05	0.552 ± .000	99.8 ± 0.04
NGC 4340	bl	25.6 ± 0.07	0.579 ± .002	104.4 ± 0.17
NGC 4340	nr	7.3 ± 0.04	0.662 ± .004	110.7 ± 0.39
NGC 4369	rs	9.5 ± 0.02	0.908 ± .003	65.7 ± 0.87
NGC 4371	r	57.1 ± 0.05	0.553 ± .001	91.2 ± 0.07
NGC 4371	nr	10.9 ± 0.03	0.474 ± .002	89.1 ± 0.16
NGC 4378	R′	90.6 ± 0.04	0.829 ± .000	2.5 ± 0.10
NGC 4378	l	45.3 ± 0.03	0.829 ± .001	159.4 ± 0.15
NGC 4429	r	80.5 ± 0.08	0.368 ± .000	96.8 ± 0.04
NGC 4429	nl	4.4 ± 0.02	0.587 ± .003	91.2 ± 0.28
NGC 4457	R	72.8 ± 0.05	0.945 ± .001	101.7 ± 0.48
NGC 4457	l	49.0 ± 0.08	0.751 ± .002	73.9 ± 0.22
NGC 4457	nl	4.1 ± 0.01	0.768 ± .003	81.3 ± 0.46

Table 5 – *continued*

Galaxy	Feature type	Major-axis radius (arcsec)	q	PA (°)
(1)	(2)	(3)	(4)	(5)
NGC 4477	RL	62.1 ± 0.02	0.926 ± .000	64.3 ± 0.19
NGC 4477	r?	39.3 ± 0.03	0.853 ± .001	29.4 ± 0.20
NGC 4503	bl	25.3 ± 0.08	0.423 ± .002	0.5 ± 0.13
NGC 4531	rs	9.7 ± 0.04	0.642 ± .003	133.7 ± 0.19
NGC 4531	RL	53.5 ± 0.08	0.652 ± .001	152.4 ± 0.11
NGC 4596	RL	105.0 ± 0.07	0.809 ± .001	128.0 ± 0.10
NGC 4596	rs	56.1 ± 0.04	0.718 ± .001	97.0 ± 0.09
NGC 4596	bl	28.2 ± 0.06	0.906 ± .003	92.0 ± 0.93
NGC 4608	r	49.3 ± 0.02	0.921 ± .001	101.7 ± 0.25
NGC 4608	bl	26.3 ± 0.04	0.933 ± .002	88.0 ± 1.01
NGC 4612	RL	76.8 ± 0.09	0.663 ± .001	145.1 ± 0.08
NGC 4612	l	40.1 ± 0.08	0.701 ± .002	147.6 ± 0.17
NGC 4643	rs	51.6 ± 0.05	0.905 ± .001	61.3 ± 0.37
NGC 4643	bl	25.6 ± 0.05	0.945 ± .003	75.3 ± 1.55
NGC 4643	nrl	3.2 ± 0.01	0.799 ± .004	39.2 ± 0.62
NGC 4643	L	94.3 ± 0.16	0.822 ± .002	50.9 ± 0.27
NGC 4649	l	22.8 ± 0.03	0.843 ± .002	117.4 ± 0.32
NGC 4665	R′L	78.2 ± 0.09	0.891 ± .001	100.3 ± 0.42
NGC 4754	L	127.9 ± 0.32	0.467 ± .001	21.3 ± 0.09
NGC 4754	bl	22.1 ± 0.09	0.756 ± .003	37.0 ± 0.39
NGC 4772	R’	113.8 ± 0.15	0.514 ± .001	145.2 ± 0.04
NGC 4772	r	70.4 ± 0.47	0.280 ± .002	145.8 ± 0.05
NGC 4880	R’	60.2 ± 0.05	0.769 ± .001	156.5 ± 0.12
NGC 4984	R	94.5 ± 0.15	0.611 ± .001	13.8 ± 0.12
NGC 4984	l	49.0 ± 0.06	0.843 ± .001	40.1 ± 0.22
NGC 4984	nrl	4.7 ± 0.02	0.746 ± .004	33.4 ± 0.49
NGC 5026	L	105.4 ± 0.33	0.540 ± .002	64.0 ± 0.13
NGC 5026	rs	35.9 ± 0.09	0.577 ± .001	51.6 ± 0.09
NGC 5026	bl	18.5 ± 0.06	0.730 ± .003	52.9 ± 0.30
NGC 5026	nl	3.1 ± 0.02	0.679 ± .006	49.0 ± 0.51
NGC 5101	OOR	160.1 ± 0.07	0.886 ± .000	148.7 ± 0.12
NGC 5101	IOR	104.1 ± 0.10	0.805 ± .001	166.0 ± 0.18
NGC 5101	rs	52.1 ± 0.03	0.823 ± .001	115.6 ± 0.10
NGC 5101	nl	5.1 ± 0.01	0.972 ± .004	42.0 ± 3.65
NGC 5101	bl	30.5 ± 0.07	0.975 ± .003	86.1 ± 3.64
NGC 5121	RL	34.2 ± 0.02	0.830 ± .001	23.8 ± 0.12
NGC 5121	rl	11.9 ± 0.02	0.703 ± .001	24.7 ± 0.12
NGC 5333	RL	21.9 ± 0.06	0.556 ± .002	50.4 ± 0.09
NGC 5333	rl	8.4 ± 0.05	0.521 ± .003	43.5 ± 0.16
NGC 5365	RL	93.8 ± 0.07	0.537 ± .001	4.5 ± 0.05
NGC 5365	rs	32.7 ± 0.04	0.907 ± .002	18.2 ± 0.56
NGC 5365	nr	6.1 ± 0.03	0.460 ± .003	4.2 ± 0.23
NGC 5377	R_1	113.4 ± 0.13	0.554 ± .001	24.0 ± 0.05
NGC 5377	nl	4.2 ± 0.03	0.587 ± .004	27.7 ± 0.31
NGC 5377	rl	66.6 ± 0.25	0.388 ± .001	36.0 ± 0.05
NGC 5419	nl	10.0 ± 0.03	0.824 ± .004	89.1 ± 0.85
NGC 5448	R’	102.9 ± 0.19	0.406 ± .001	113.9 ± 0.04
NGC 5448	rs	49.1 ± 0.22	0.390 ± .002	110.2 ± 0.11
NGC 5448	nl	3.6 ± 0.02	0.554 ± .003	117.3 ± 0.19
NGC 5473	L	43.6 ± 0.08	0.755 ± .002	151.7 ± 0.21
NGC 5638	l	6.3 ± 0.03	0.902 ± .006	127.5 ± 1.77
NGC 5701	R’	100.1 ± 0.11	0.837 ± .001	80.8 ± 0.26
NGC 5701	rl	40.6 ± 0.04	0.866 ± .001	171.8 ± 0.29
NGC 5701	bl	21.1 ± 0.09	0.975 ± .005	172.7 ± 6.15
NGC 5728	R_1	102.0 ± 0.05	0.719 ± .000	177.9 ± 0.06
NGC 5728	rs	54.8 ± 0.12	0.522 ± .001	32.4 ± 0.07
NGC 5728	nr	4.7 ± 0.01	0.763 ± .002	6.3 ± 0.37
NGC 5750	RL	82.5 ± 0.14	0.475 ± .001	69.0 ± 0.06
NGC 5750	l	55.5 ± 0.09	0.527 ± .001	66.9 ± 0.07
NGC 5750	r	34.7 ± 0.07	0.499 ± .001	63.1 ± 0.07
NGC 5750	bl	15.5 ± 0.10	0.487 ± .003	57.9 ± 0.18

Table 5 – *continued*

Galaxy	Feature type	Major-axis radius (arcsec)	q	PA (°)
(1)	(2)	(3)	(4)	(5)
NGC 5838	L	91.6 ± 0.45	0.347 ± .002	40.5 ± 0.05
NGC 5838	nl	3.8 ± 0.02	0.782 ± .005	27.6 ± 0.67
NGC 5846	nl	2.1 ± 0.02	0.943 ± .012	25.1 ± 6.44
NGC 5846	l	10.6 ± 0.01	0.975 ± .001	85.9 ± 1.44
NGC 5846	L	29.7 ± 0.03	0.978 ± .001	66.8 ± 1.98
NGC 5898	L	64.9 ± 0.05	0.939 ± .001	55.5 ± 0.51
NGC 5898	l	21.3 ± 0.03	0.990 ± .002	37.2 ± 5.69
NGC 5898	nl	6.8 ± 0.02	0.957 ± .004	101.3 ± 3.29
NGC 5953	rs	6.2 ± 0.01	0.980 ± .001	69.5 ± 2.24
NGC 6012	l	50.8 ± 0.05	0.686 ± .001	165.4 ± 0.10
NGC 6012	x1r	21.9 ± 0.50	0.254 ± .006	151.4 ± 0.16
NGC 6340	nl	4.9 ± 0.01	0.924 ± .001	101.1 ± 0.63
NGC 6340	l	19.0 ± 0.04	0.940 ± .003	105.0 ± 1.61
NGC 6340	RL	32.2 ± 0.05	0.887 ± .002	107.2 ± 0.49
NGC 6438	l	15.7 ± 0.05	0.927 ± .004	175.2 ± 1.79
NGC 6646	R’	33.7 ± 0.03	0.734 ± .001	86.8 ± 0.12
NGC 6646	rs	19.4 ± 0.04	0.763 ± .002	77.5 ± 0.34
NGC 6654	R′	65.2 ± 0.06	0.647 ± .001	178.6 ± 0.09
NGC 6684	R′L	84.4 ± 0.09	0.634 ± .001	32.7 ± 0.06
NGC 6684	rs	34.4 ± 0.03	0.814 ± .001	19.8 ± 0.14
NGC 6703	RL	40.0 ± 0.04	0.982 ± .001	131.0 ± 2.20
NGC 6782	R	52.1 ± 0.04	0.837 ± .001	67.5 ± 0.14
NGC 6782	rl	25.1 ± 0.02	0.687 ± .001	1.7 ± 0.11
NGC 6782	nr’	4.9 ± 0.01	0.920 ± .002	14.3 ± 0.72
NGC 6782	bl	13.1 ± 0.03	0.833 ± .002	1.9 ± 0.49
NGC 6958	l	29.7 ± 0.04	0.967 ± .002	107.7 ± 1.96
NGC 7079	RL	46.0 ± 0.06	0.565 ± .001	80.7 ± 0.09
NGC 7079	bl	11.8 ± 0.02	0.527 ± .001	89.7 ± 0.11
NGC 7098	R’	107.8 ± 0.06	0.581 ± .000	78.5 ± 0.04
NGC 7098	l	67.5 ± 0.07	0.581 ± .001	65.6 ± 0.05
NGC 7192	l	12.0 ± 0.02	0.966 ± .002	80.2 ± 1.80
NGC 7192	L	40.9 ± 0.03	0.956 ± .001	69.0 ± 0.63
NGC 7213	r	25.4 ± 0.02	0.947 ± .001	52.2 ± 0.63
NGC 7213	rl	13.4 ± 0.01	0.966 ± .001	75.2 ± 0.54
NGC 7217	R’	86.4 ± 0.06	0.844 ± .001	93.7 ± 0.19
NGC 7217	l	35.9 ± 0.03	0.858 ± .001	82.1 ± 0.21
NGC 7217	nl	15.0 ± 0.06	0.858 ± .005	84.6 ± 1.17
NGC 7377	l	7.3 ± 0.01	0.789 ± .002	101.3 ± 0.33
NGC 7727	nr	9.2 ± 0.03	0.291 ± .001	86.7 ± 0.10
NGC 7742	L	23.0 ± 0.02	0.967 ± .001	89.2 ± 1.06
NGC 7742	r_1	10.3 ± 0.01	0.981 ± .001	91.4 ± 1.49
NGC 7742	r_2	7.3 ± 0.01	0.969 ± .001	134.6 ± 1.05

is also double-barred. We find two nearly orthogonal nuclear rings with a nuclear bar and nuclear lens inside these features.

In Fig. 15(b), *prototypical examples of multiple lenses in non-barred galaxies* are shown. The lenses can be intermediate types between rings and lenses as in NGC 3032, or full lenses as in NGC 524 and 7192. As we previously noted, NGC 524 is an example of a non-barred S0 galaxy having a series of circular lenses, the three lenses being clearly visible in this case. Depending on the prominence of the lenses, the galaxies are classified as either $S0^o$ or $S0^-$. These kinds of galaxies illustrate interesting borderline cases between S0s and ellipticals: if the lenses are weak, the galaxies can be easily misclassified as elliptical galaxies, because their surface brightness profiles are fairly similar. For a full discussion of their nature, kinematic observations are also needed.

There are many questions related to multiple lenses in S0s that need to be answered. For example, (1) are lenses primarily formed soon after the disc formation or are they rather bar-related products of secular evolution in galaxies? (2) if produced mainly by secular evolution, are lenses former bars dissolved into lenses, or more likely structures triggered by bars, for example via ring formation? (3) what are the possible secular evolutionary processes producing the multiple lenses in non-barred galaxies? and, finally, (4) how can the multiple bar/lens systems be maintained in the current hierarchical picture of galaxy formation? We discuss these issues in a forthcoming paper.

7.3 $S0_c$ galaxies?

Candidates of $S0_c$-type galaxies, which group of galaxies were suggested by van den Bergh (1976), were searched from the NIRS0S sample. The appearance of this kind of galaxies having discs with no spiral arms, but B/T as small as typically found in Sc-type spirals,

Table 6. Bar dimensions: major-axis radius (r_{vis}, r_{ell} r_L, explained in Section 6), orientation (PA) and minor-to-major-axis ratio (q). STdev is the estimated standard deviation of r_{vis} and r_{ell}.

Galaxy	Bar type	PA (°)	r_{vis} (arcsec)	r_{ell} (arcsec)	r_L (arcsec)	STdev (arcsec)	q
(1)	(2)	(3)	(4)	(5)	(6)	(7)	(8)
IC 4214	nb	89.3	4.1	3.9	4.3	0.1	0.750
	$\underline{A}$B	161.7	30.8	26.2	30.5	2.3	0.468
IC 5240	B_x	93.4	34.1	38.6		2.2	0.269
IC 5328	$\underline{A}B_a$	41.0	50.4	42.5	51.2	3.0	0.495
NGC 474	AB	28.6	18.0	18.0		0.0	0.750
NGC 484	nb	89.3	2.5	2.4	3.0	0.1	0.757
NGC 507	nb	20.0	4.0	4.6	10.3	0.3	0.757
	AB	58.9	20.7	17.5	19.3	1.6	0.624
NGC 584	AB	58.3	17.6			2.0	0.625
NGC 718	AB	155.5	20.0	17.5	25.8	1.3	0.572
NGC 936	B	80.3	38.2	37.5	51.9	0.3	0.520
NGC 1022	nb	45.0	1.2				
	AB	116.2	17.8	17.5	25.8	0.1	0.565
NGC 1079	nb	80.0	1.5	1.5			0.78
	AB_a	119.6	33.4	31.2	40.7	1.1	0.501
NGC 1201	nb	3.0	5.0	5.0		0.0	0.65
	AB_a	15.0	25.0				0.556
NGC 1302	AB	171.4	29.5	25.6	37.7	1.9	0.660
NGC 1317	nb	56.2	6.4	6.3	8.7	0.1	0.533
	AB	150.7	47.2	42.2	51.9	2.5	0.732
NGC 1326	nb	87.2	5.4	3.9	7.0	0.7	0.646
	AB_a	24.5	35.7	34.9		0.4	0.590
NGC 1350	nb	15.0	3.0				
	AB_a	33.4	58.0	54.3	60.2	1.8	0.421
NGC 1371	AB	119.6	20.8	21.7	26.9	0.5	0.539
NGC 1380	AB	5.8	78.1	70.0	95.0	4.0	0.457
NGC 1387	B	109.3	21.5	23.8	33.0	1.1	0.676
NGC 1389	nb	37.6	4.5	3.4	6.4	0.6	0.623
	AB	0.0	2.0				
NGC 1415	AB_a	132.7	27.4	35.0		4.0	0.427
NGC 1440	B	52.1	20.8	19.3	25.1	0.8	0.541
NGC 1452	B_a	34.1	28.1	25.6	31.6	1.2	0.516
NGC 1512	B_a	45.9	62.5	76.4	87.0	6.9	0.350
NGC 1533	B	165.8	20.2	21.2	29.3	0.5	0.603
NGC 1537	B	89.3	23.9	20.7	37.7	1.6	0.525
NGC 1543	nb	35.1*	10.3	8.2	10.1	1.0	0.717
	B	92.1	76.6	66.8	85.2	4.9	0.510
NGC 1553	nb	3.6*	7.9	8.5	15.5	0.3	0.613
NGC 1574	B	147.2	15.1	14.8	21.8	0.2	0.705
NGC 1617	AB_a	98.9	46.6	58.7	68.4	6.1	0.444
NGC 2217	nb	138.9	7.7	7.5	9.6	0.1	0.818
	B	111.4	41.6	39.5	46.3	1.0	0.548
NGC 2273	nb	54.6*	3.9	2.1	4.3	0.9	0.680
	AB	115.5*	16.1	17.4	20.4	0.7	0.592
NGC 2293	AB_a	134.4*	25.3	25.4		0.1	0.446
NGC 2460	$\underline{A}$B	7.9	5.0	4.2	5.2	0.4	0.731
NGC 2523	B	116.2	22.4	22.9	28.2	0.3	0.361
NGC 2549	B_x	178.3	8.4	7.4	10.2	0.5	0.452
NGC 2655	$\underline{A}$B	86.5					0.659
NGC 2681	nb	16.2	3.0	1.8	3.2	0.6	0.870
	AB	70.0	17.5	17.5	21.6	0.0	0.696
	ob	35.5	43.0	50.0			0.771
NGC 2782	nb	97.6	5.9	2.3	4.8	1.8	0.668
NGC 2787	B_a	155.4*	28.3	28.2		0.1	0.638
NGC 2859	nb	72.5*	4.0	3.9	7.8	0.0	0.733
	AB_a	158.3	36.9	34.0	40.9	1.4	0.617
NGC 2880	B	88.6*	9.0	8.5	9.0	0.3	0.796
NGC 2902	nb	119.9*	4.5	4.9	6.8	2.0	0.939
NGC 2950	nb	96.9	4.9	3.1	4.6	2.2	0.718
	B_a	152.7	22.9	23.3	28.7	0.2	0.572

Table 6 – *continued*

Galaxy	Bar type	PA (°)	r_{vis} (arcsec)	r_{ell} (arcsec)	r_L (arcsec)	STdev (arcsec)	q
(1)	(2)	(3)	(4)	(5)	(6)	(7)	(8)
NGC 2983	B_a	41.0	19.3	19.2	21.3	0.0	0.543
NGC 3081	nb	117.6	5.7	5.6	7.8	0.0	0.511
	AB	75.5	30.7	34.3	40.0	1.8	0.382
NGC 3100	$\underline{A}B$	163.8	27.0	31.7		2.3	0.651
NGC 3166	nb	86.5	2.3	3.1	6.8	1.1	0.560
	$A\underline{B}_a$	166.5	20.9	18.8	20.6	1.0	0.832
NGC 3169	nb	49.3	7.7	7.2	11.4	1.2	0.631
NGC 3227	AB_x	149.3	59.2	53.9	66.7	7.6	0.391
NGC 3245	AB_a	175.5					0.501
NGC 3358	AB_a	161.7	18.2	20.0		1.0	0.579
NGC 3384	nb	47.2	3.5	2.8	9.1	2.9	0.582
	B	135.0*	17.5				
NGC 3412	B_a	113.4	16.2	15.4	17.0	0.4	0.736
NGC 3489	B	20.8*	8.3	6.6	10.3	1.3	0.666
NGC 3516	B_a	168.6	11.8	10.9	14.2	0.5	0.680
NGC 3626	nb	164.5	2.5	2.3	3.8	1.0	0.602
	$\underline{A}B_a$	170.7	20.4	19.2	28.4	0.6	0.459
NGC 3718	AB						
NGC 3729	B	32.8*	20.8	21.2	24.7	0.2	0.355
NGC 3892	B	99.6	29.4	33.3	42.4	1.9	0.515
NGC 3941	nb	18.9	3.3	3.1	3.6	0.6	0.809
	B_a	160.5*	20.8	22.7		1.0	0.526
NGC 3945	nb	156.9	9.8	9.6	13.4	0.1	0.642
	B_a	72.1	35.7	33.3	36.8	1.2	0.700
NGC 3998	nb	129.3	6.9	7.9	9.3	0.5	0.785
NGC 4073	$\underline{A}B$	100.3	10.9	9.5	14.1	0.7	0.639
NGC 4106	nb	20.0*	6.0	5.0		0.5	0.625
	AB	170.0*	21.3	23.7	27.0	1.2	0.787
NGC 4143	nb	135.0	2.0				
	AB_a	155.5	19.1	20.5		0.7	0.578
NGC 4203	$\underline{A}B_a$	10.0	14.3	12.8	20.8	1.2	0.753
NGC 4220	AB_x	133.4	31.6	34.7	39.5	1.6	0.289
NGC 4245	B	136.2	34.9	36.5	47.6	0.8	0.477
NGC 4262	B_a	19.6	12.6	12.8	16.7	0.1	0.647
NGC 4267	AB	27.9	16.7	17.9	22.8	0.6	0.786
NGC 4293	B_x	76.2	74.2	74.0		0.0	0.244
NGC 4314	B	145.8	67.3	64.7	95.5	1.3	0.351
NGC 4340	nb	8.3*	4.2	3.8	4.2	0.2	0.903
	B_a	37.6	37.9	37.5	43.9	0.2	0.602
NGC 4369	B	156.2	5.6	4.6	11.0	0.5	0.373
NGC 4371	B_a	157.6	34.9	33.8	38.4	0.5	0.736
NGC 4424	B	107.2	7.7	7.2	13.0	2.2	0.211
NGC 4429	B_x	98.9	72.5	78.3	91.2	3.0	0.338
NGC 4457	nb	72.7	4.0	3.4	6.1	0.6	0.813
	AB	69.3	40.5	30.2	37.2	5.1	0.625
NGC 4477	B	8.4*	29.4	29.0		0.2	0.621
NGC 4503	$\underline{A}B$	25.0					
NGC 4546	AB	20.9*	5.0				
NGC 4596	B	74.1	53.8	53.5	65.9	0.2	0.463
NGC 4608	B	25.8	43.8	43.8	52.8	0.0	0.493
NGC 4612	$\underline{A}B_a$	101.7	17.5	17.9	22.2	0.2	0.757
NGC 4643	B	131.4	48.1	45.2	59.2	1.5	0.527
NGC 4665	B	1.9*	48.3	43.8	69.0	1.6	0.486
NGC 4691	B	89.3	17.9	14.0	21.0	1.9	0.289
NGC 4694	nb	145.2	3.2	2.5	3.4	0.9	0.455
NGC 4754	nb	18.9	8.1	6.7	9.6	0.7	0.754
	B_a	131.5*	25.0	22.7	25.1	1.2	0.765
NGC 4880	$\underline{A}B$	168.6	8.4	8.1	16.6	0.1	0.571
NGC 4984	nb	61.7	4.0	4.2	8.7	0.4	0.817
	AB_a	90.7	30.5	28.2	44.3	1.2	0.697

Table 6 – *continued*

Galaxy	Bar type	PA (°)	r_{vis} (arcsec)	r_{ell} (arcsec)	r_{L} (arcsec)	STdev (arcsec)	q
(1)	(2)	(3)	(4)	(5)	(6)	(7)	(8)
NGC 5026	B	170.5*	22.2	24.8	31.7	1.3	0.617
NGC 5101	B	118.9	51.0	48.3	59.4	1.4	0.474
NGC 5206	B	24.5	95.1	95.0		0.0	
NGC 5333	nb	156.5*	2.6	2.0		0.3	0.698
NGC 5353	B_x	144.5	20.8	18.0		1.4	0.426
NGC 5365	nb	45.9*	4.8	5.7	10.9	0.5	0.685
	B_a	112.0	29.1	26.2	30.5	1.5	0.740
NGC 5377	$\underline{AB}_x$	45.2	65.9	57.7	67.5	6.1	0.341
NGC 5448	AB_x	94.8	40.2	36.5	42.9	1.8	0.311
NGC 5473	B	83.1	15.6	13.9	14.5	0.8	0.767
NGC 5701	B	176.9	38.7	39.9	46.6	0.6	0.571
NGC 5728	nb	85.2	4.0	3.2	3.7	0.4	0.597
	B	31.4	52.9	56.0	73.1	1.6	0.323
NGC 5750	$\underline{AB}_a$	112.1	20.0	21.6	23.8	1.9	0.589
NGC 5838	nb	39.6	3.5	3.0		0.2	0.75
	AB	50.7	12.1	12.8	13.4	0.9	0.714
NGC 6012	B	154.8	18.2	22.9	41.3	2.2	0.386
NGC 6438	$\underline{AB}$	171.4	4.4	3.2	7.4	0.6	0.711
NGC 6646	AB	51.4	14.5	16.5	22.8	1.4	0.675
NGC 6654	nb	135.0*	4.4	2.6	3.6	0.9	0.860
	B_a	12.7	25.9	25.6	33.4	0.1	0.465
NGC 6684	nb	60.3	3.5	2.9	4.9	0.3	0.689
	AB	151.4	24.5	28.8	31.8	2.1	0.693
NGC 6782	nb	149.3	4.3	3.5	4.1	0.4	0.577
	AB	178.9	25.11	26.2	26.2	0.5	0.483
NGC 7079	nb	131.7*	4.5	2.4	3.3	1.0	0.827
	B_a	53.4	14.9	14.8	18.2	0.0	0.588
NGC 7098	nb	79.0*	7.8	9.2	10.7	0.7	0.684
	AB_a	50.0	43.2	42.0	51.8	0.6	0.454
NGC 7332	B_x		32.4	30.1	35.2	1.2	0.324
NGC 7371	$\underline{AB}$	163.1	9.5	9.2	10.7	0.2	0.729
NGC 7743	AB	94.8	19.0	21.4	22.3	1.2	0.640

*Visually estimated.

was noted by Erwin et al. (2003) and Laurikainen et al. (2006, 2010). In Fig. 16, we show representative examples of these galaxies. Using the structure decompositions of Laurikainen et al. (2010), and allowing for $B/T \leq 0.1$, 14 S0s were found. This limit was selected because it is the mean B/T value for Sc-type spirals, based on the decompositions for spirals made in a similar manner to that for the NIRS0S galaxies. The bulge flux is taken to be that fitted by a Sersíc function, whereas the disc flux is a sum of all the disc components, including bars and lenses. All the galaxies in Fig. 16 have a small bulge manifested as a narrow peak in the surface brightness profile and a prominent extended disc. These galaxies have similar or at most only slightly fainter total absolute K-band magnitudes (for the nine galaxies in the figure $\langle M_K \rangle = -23.6$ mag, whereas for the 14 galaxies $\langle M_K \rangle = -23.9$) than the S0 galaxies in general ($\langle M_K \rangle \sim= -24.0$). The absolute magnitudes were calculated using the K-band magnitudes from the 2MASS, corrected for Galactic extinction taken from the NED, based on the maps of Schlegel, Finkbeiner & Davis (1998), and using galaxy distances from the Catalog of Nearby Galaxies by Tully (1988). A Hubble constant of $H_0 = 75\,\mathrm{km\,s^{-1}\,Mpc^{-1}}$ is used.

Of the non-barred galaxies (see Fig. 16), NGC 4138 and 5273 have very narrow peaks in the surface brightness profiles, and either ring or subtle spiral features, which might be manifestations of an earlier spiral stage of these galaxies. NGC 1411 has more mass in the central regions, due to a very prominent lens. The three barred galaxies, NGC 3081, 4429 and 4220 have obviously very small bulges embedded in large discs. The last three galaxies, NGC 2983, 3892 and 5838, are examples of barred galaxies having prominent barlenses, the small bulges embedded inside these lenses. Our example galaxies can be former Sc-type spirals in which gas is either stripped or consumed by star formation, as originally suggested by Baade (1963) and van den Bergh (1976): due to dynamical heating of the disc, the spiral arms have disappeared, but the other disc structures like bars, lenses and rings are still visible, in a similar manner to that in spirals.

8 CONCLUSIONS

The NIRS0S atlas of 206 early-type disc galaxies is presented in the K_s band, including 160 S0-S0/a galaxies. In order to discuss the borderline of S0s with ellipticals and spirals, late-type ellipticals classified as S0s in the RSA and Sa spirals were also included in the sample. A subsample of 185 galaxies forms a magnitude-limited sample, having total magnitudes of $B_T \leq 12.5$ mag and inclinations less than 65°. The obtained images are deep, typically reaching a surface brightness level of 23.5 mag arcsec^{-2} (exceptions are galaxies having too small FOV). A subarcsecond pixel scale (∼0.25 arcsec) was used and the observations were generally carried out in good seeing conditions (FWHM ∼ 1 arcsec). The flux-calibrated images are shown in many different scales, optimized to show the

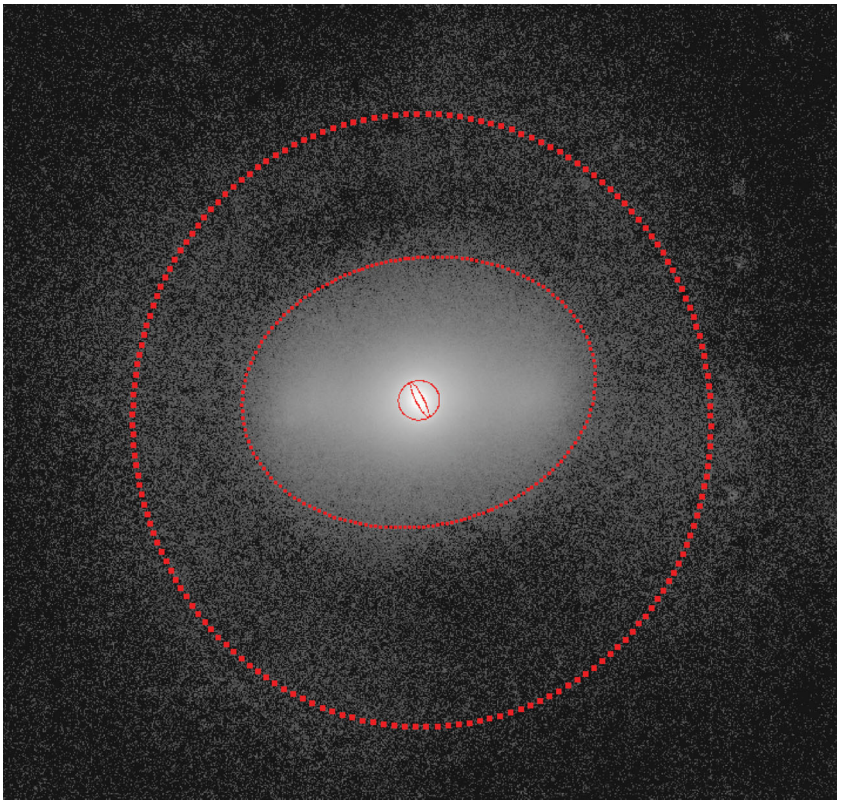

Figure 13. An illustration of our strategy for measuring the dimensions of the structures: the fitted ellipsoids of the identified structures are shown for NGC 1543. From outside towards inside, the ellipsoids are for: the outer ring (R), the lens and the bar (l,B) and the nuclear lens (nl). Also the nuclear bar (nb) is fitted, though it has the same dimension as the nuclear lens (plots for all galaxies are available at the NIRS0S website (http://www.oulu.fi/astronomy/NIRS0S_pub/nirsos_dimensions.html).

multicomponent nature of many of the galaxies. In the atlas panels, the radial profiles of the PA, ellipticity and deviation of the isophotes from perfect ellipticities ($b4$) are also shown.

A detailed morphological classification was made using the criteria of de Vaucouleurs (1959). Special attention was paid to the recognition of lenses in NIRS0S galaxies, which has been done in a more systematic manner than in any of the previous studies. Lenses are coded in a similar manner to that followed while nuclear, inner and outer rings were previously coded by Buta et al. (2010). A new lens type called a 'barlens' was also introduced, referring to the intermediate-sized, bulge-looking component that seems prominent in many early-type barred galaxies, presumably forming part of the bar itself. When elongated along the bar, it has the appearance of the so-called 'boxy bar'. Bar morphology is included in the classification: ansae morphology was detected in 33 bars, and x-shaped bar structures in nine non-edge-on galaxies.

Besides visual classifications, we also present photometric classifications, which means that exponential outer discs or faint inner structures were considered even if they were not directly visible in the images. The faint structures were identified from unsharp masked or residual images after subtracting a bulge model taken from the structural decompositions of Laurikainen et al. (2010). Our visual and photometric classifications deviate for 42 galaxies: for example, 15 faint bars, outshone by bulges in visual classification, were detected, and seven elliptical galaxies were moved into the S0 stage. However, the mean Hubble stage in our visual classification in the near-IR is the same as that in the RC3, determined in the optical wavelength range.

We confirm the previous result by Laurikainen et al. (2009) that most early-type disc galaxies have lenses, which we find to be the case in both barred (61 per cent) and non-barred (38 per cent) galaxies. Most importantly, we find that up to 25 per cent of the atlas galaxies, including the S0-S0/a galaxies, have multiple lenses. However, only six galaxies (4 per cent) have shells or ripples, which are expected to be direct manifestations of recent mergers. The detection of multiple lenses in a large number of S0-S0/a galaxies is a challenge to the hierarchical formative processes of galaxies: it needs to be explained how such lens systems were formed and survived in the merger events that galaxies might have suffered several times in their lifetimes. We discuss tentative morphological sequences of possible formative processes of lenses. Possible candidates of $S0_c$ galaxies are shown, which galaxies are expected to be former Sc-type spirals stripped of gas.

ACKNOWLEDGMENTS

We acknowledge the allocation of significant observing time to this project during 2003–09, based on observations made with several telescopes. These include the NTT, operated at the ESO at La Silla in Chile. The ESO is supported by 15 countries: Austria, Belgium, Brazil, the Czech Republic, Denmark, France, Finland, Germany, Italy, the Netherlands, Portugal, Spain, Sweden, Switzerland and the United Kingdom. Also included are the WHT, TNG and NOT, operated on the island of La Palma by, respectively, the Isaac Newton Group of Telescopes, the Fundación Galileo Galilei of the Istituto Nazionale di Astrofisica (INAF), and jointly by Denmark,

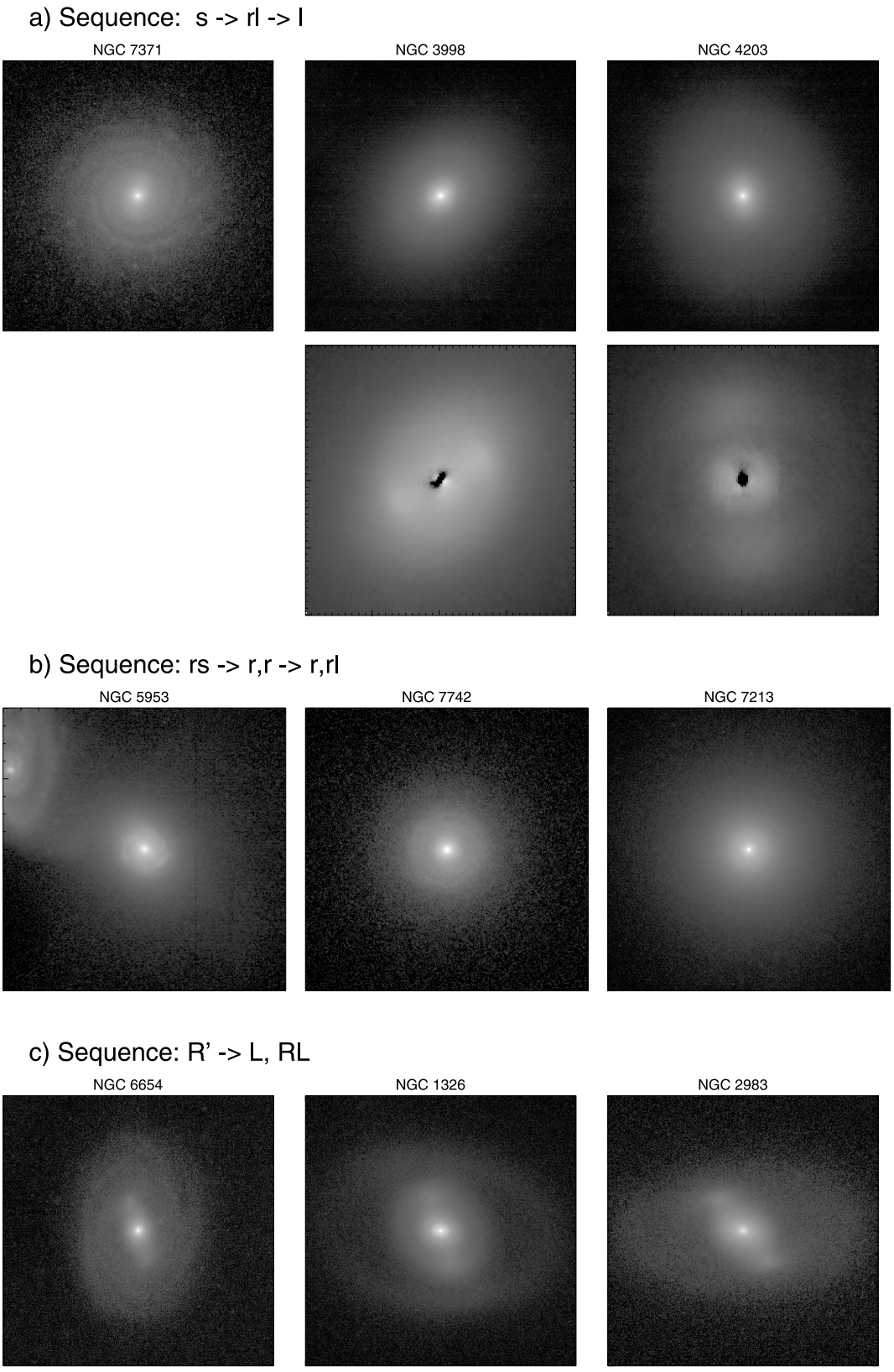

Figure 14. Examples of possible formative sequences of lenses. In (a), the two lower panels show the inner parts of the galaxies NGC 3998 and 4203: in these figures, the bulge models obtained from the decompositions are subtracted from the original images.

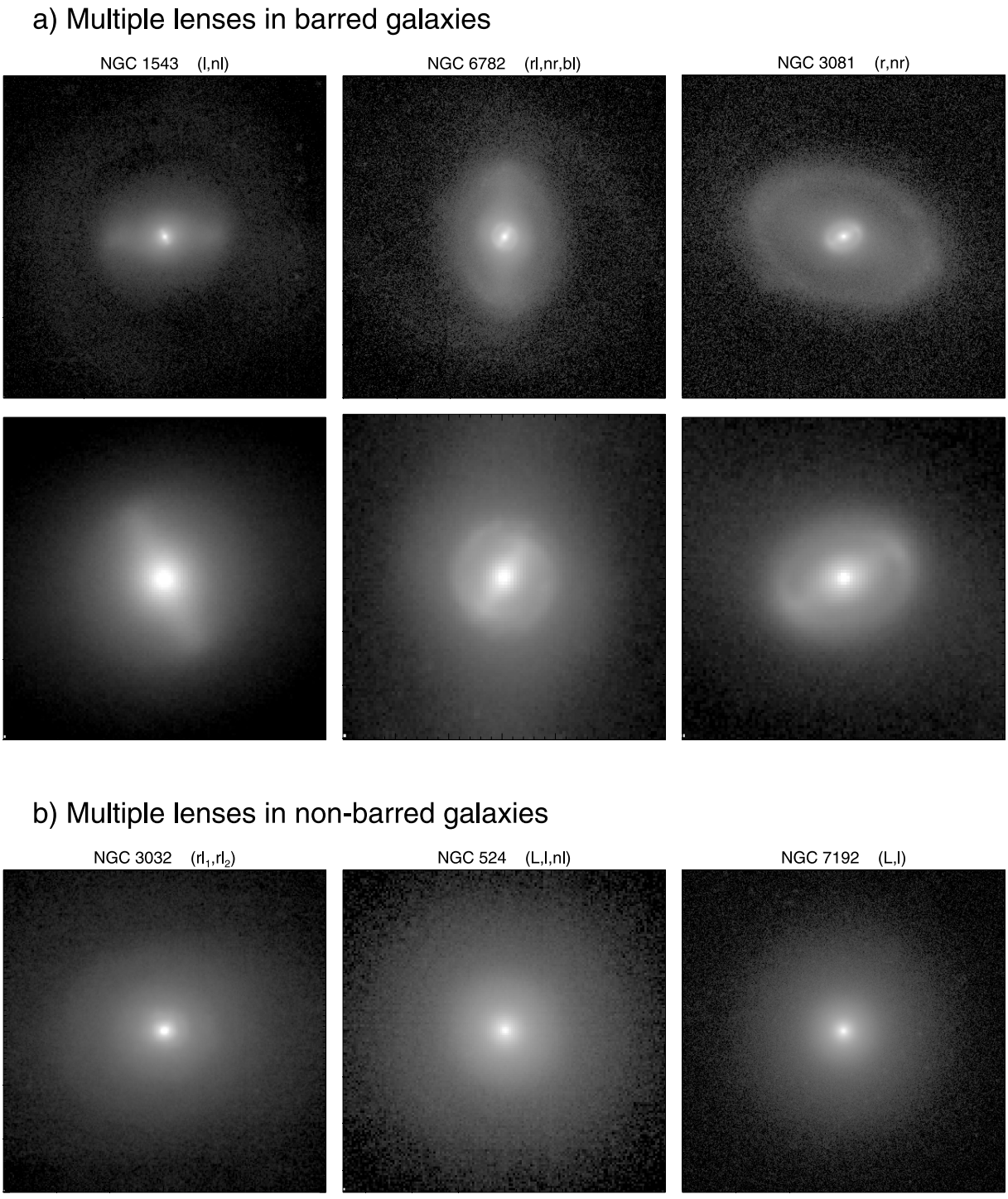

Figure 15. Examples of multiple lenses. (a) Three barred galaxies are shown: the upper panels illustrate the lenses surrounding the primary bars and the lower panels illustrate those surrounding the nuclear bars (only the central regions of the galaxies are shown). For NGC 1543 and 6782, the lenses are clear. However, for NGC 3081, the nuclear and inner rings are very prominent and the two bars extremely weak, so that no lenses are coded to the classification. (b) Typical examples of multiple lenses in non-barred galaxies.

Finland, Iceland, Norway and Sweden, in the Spanish Observatorio del Roque de los Muchachos of the Instituto de Astrofísica de Canarias. Included are also the 4-m telescope operated at the CTIO in La Serena, Chile, and Flamingos (FLMN) operated at the KPNO in Tucson, Arizona. We also acknowledge the participation of Jarkko Laine, Sebastien Comerón, Sami Airaksinen, Tom Speltincx, Leena Pelttari and Timothy Brockett in making the observations. This publication makes use of data products from the 2MASS, which is a joint project of the University of Massachusetts and the Infrared Processing and Analysis Center/California

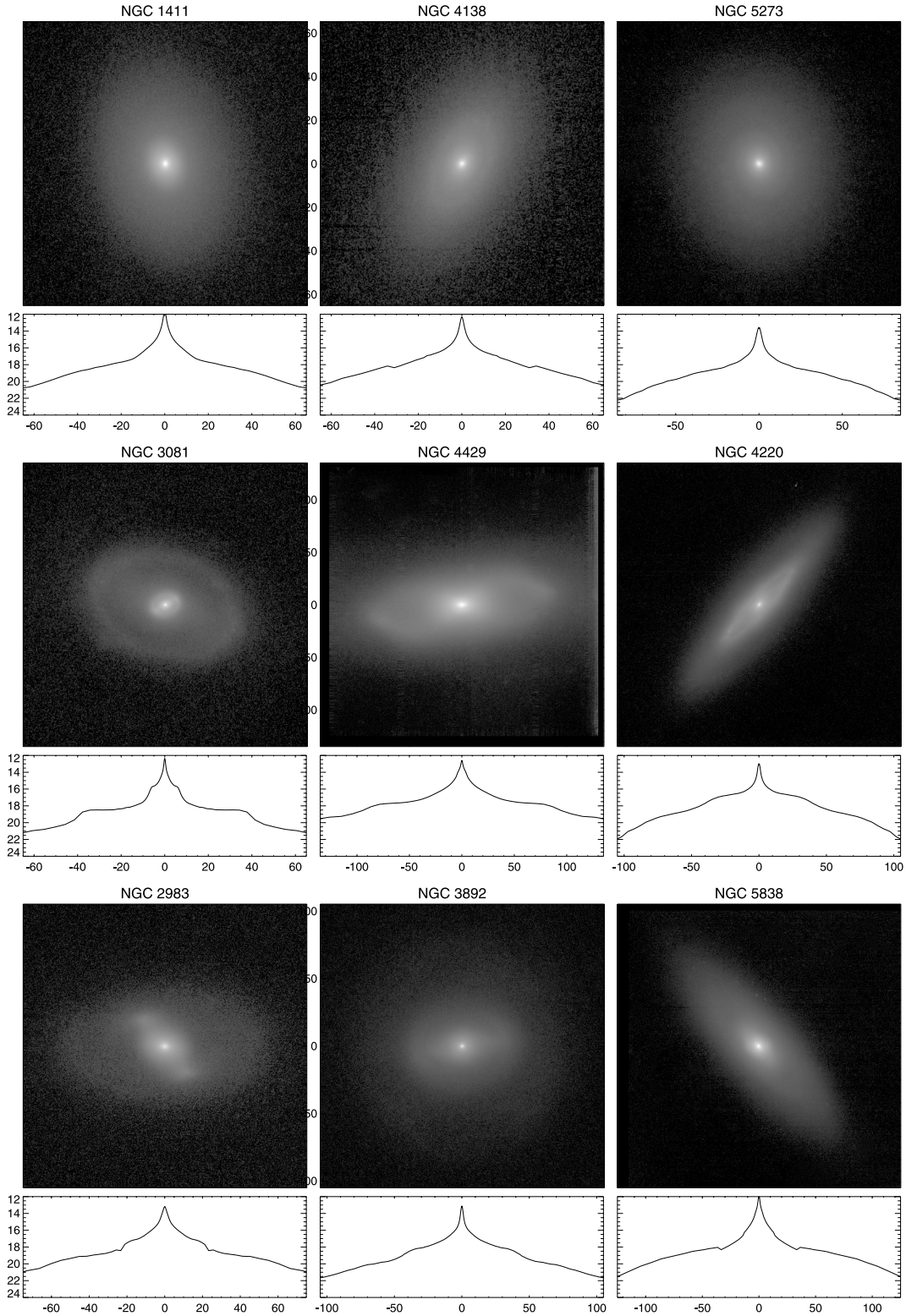

Figure 16. Candidates of $S0_c$-type galaxies, showing no spiral arms and B/T as small as typically found for Sc-type spirals. For each galaxy are shown the flux-calibrated cleaned image and the azimuthally averaged surface brightness profile. The radial scale is in arcsec.

Institute of Technology, funded by the National Aeronautics and Space Administration and the National Science Foundation. This research has also made use of the IRSA, which is operated by the Jet Propulsion Laboratory, California Institute of Technology, under contract with the National Aeronautics and Space Administration. We acknowledge the financial support by the Academy of Finland. RB acknowledges the support of NSF grant AST 050-7140 for part of this work.

REFERENCES

Athanassoula E., 2003, MNRAS, 341, 1179
Athanassoula E., Misioritis A., 2002, MNRAS, 330, 35
Athanassoula E., Sellwood J. A., 1983, in Athanassoula E., ed., Proc. IAU Symp. 100, Internal Kinematics and Dynamics of Galaxies. Reidel, Dordrecht, p. 203
Athanassoula E., Romero-Gómez M., Bosma A., Masdemont J. J., 2010, MNRAS, 407, 1433
Baade W., 1963, in Payne-Gaposchin C., ed., Evolution of Stars and Galaxies. Harvard Univ. Press, Cambridge, p. 232
Bekki K., Couch W. J., 2011, MNRAS, 415, 1783
Bender R., 1988, A&A, 202, L7
Bender R., Surma P., Dobereiner S., Möllenhoff C., Madeijsky R., 1989, A&A, 217, 35
Bosma A., 1983, in Athanassoula E., ed., Proc. IAU Symp. 100, Internal Kinematics and Dynamics of Galaxies. Reidel, Dordrecht, p. 253
Bureau M., Freeman K. C., 1999, AJ, 118, 126
Buta R., 1995, ApJS, 96, 39
Buta R. J., 2011, in Keel W. C., ed., Planets, Stars, and Systems Vol. 6. Springer-Verlag, Berlin (arXiv:1102.0550)
Buta R., Block D. L., 2001, ApJ, 550, 243
Buta R., Crocker D. A., 1991, AJ, 102, 1715
Buta R., Laurikainen E., Salo H., Block D. L., Knapen J. H., 2006, AJ, 132, 1859
Buta R. J., Corwin H. G., Odewahn S. C., 2007, The de Vaucouleurs Atlas of Galaxies. Cambridge Univ. Press, Cambridge (dVA)
Buta R. et al., 2010, ApJS, 190, 147
Comerón n. S., Knapen J. H., Beckman E., Laurikainen E., Salo H., Martinez-Valpuesta I., Buta R., 2010, MNRAS, 402, 2462
de Vaucouleurs G., 1959, Handbuch der Physics, 53, 275
de Vaucouleurs G., 1963, ApJS, 8, 31
de Vaucouleurs G., de Vaucouleurs A., Corwin H. G., Buta R., Paturel G., Fouqué P., 1991, Third Reference Catalogue of Bright Galaxies. Springer, New York
de Zeeuw T. et al., 2002, MNRAS, 329, 513
Djorgovski S., Carvalho R., Shlosman I., Schombert J., 1992, in Longo G., Capaccioli M., Busarello G., eds, Morphological and Physical Classification of Galaxies. Kluwer, Dordrecht, p. 427
Dressler A., Sandage A., 1983, ApJ, 265, 664
Dutton A. A., van den Bosch F. C., 2009, MNRAS, 396, 141
Emsellem E. et al., 2007, MNRAS, 379, 401
Erwin P., Sparke L., 2003, ApJS, 146, 299
Erwin P., Beltrán J. C., Graham A. W., Beckman J. E., 2003, ApJ, 597, 929
Eskridge P. et al., 2002, ApJS, 143, 73
Fall S. M., Efstathiou G., 1980, MNRAS, 193, 189
Grouchy R. B., Buta R., Salo H., Laurikainen E., 2010, AJ, 139, 2465
Hammer F., Flores H., Puech M., Yang Y. B., Athanassoula E., Rodrigues M., Delgado R., 2009, A&A, 507, 1313
Hubble E., 1936, Realm of Nebulae. Yale Univ. Press, New Haven
Jarrett T. H., Chester T., Cutri R., Schneider S., Skrutskie M., Huchra J. P., 2000, AJ, 119, 2498
Jedrzejewski R. I., 1987, MNRAS, 226, 747
Jore K. P., Broeils A. H., Haynes M. P., 1996, AJ, 112, 2
Kauffman G., Colberg J. M., Jorg M., Antonaldo D., White S. D. M., 1999, MNRAS, 303, 188
Kennicutt R. C., 2003, PASP, 115, 928
Kennicutt R., 2007, BAAS, 211, 9502
King I., 1992, in Longo G., Capaccioli M., Busarello G., eds, Morphological and Physical Classification of Galaxies, Kluwer, Dordrecht, p. 371
Kormendy J., 1979, ApJ, 227, 714
Kormendy J., Bender R., 1996, ApJ, 464, L119
Kormendy J., Kennicutt R. C., 2004, ARA&A, 42, 603
Kormendy J., Fisher D. B., Cornell M. E., Bender R., 2009, ApJS, 182, 216
Kuijken K., Merrifield M. R., 1995, ApJ, 443, L13
Laurikainen E., Salo H., Buta R., 2005, MNRAS, 362, 1319
Laurikainen E., Salo H., Buta R., Knapen J., Speltincx T., Block D. L., 2006, AJ, 132, 2634
Laurikainen E., Salo H., Buta R., Knapen J. H., 2007, MNRAS, 381, 401
Laurikainen E., Salo H., Buta R., Knapen J. H., 2009, ApJ, 692, L34
Laurikainen E., Salo H., Buta R., Knapen J. H., Comern S., 2010, MNRAS, 405, 1089
Lin D. N. C., Pringle J. E., 1987, ApJ, 320, L87
Lundmark K., 1926, Medd. Astron. Obs. Uppsala, No 30
Malin D. F., Carter D., 1980, ApJ, 274, 534
Mapelli M., Moore B., Ripamonti E., Mayer L., Colpi M., Giordano L., 2008, MNRAS, 383, 1223
Martinez-Valpuesta I., Knapen J. H., Buta R., 2007, AJ, 134, 1863
Persson S. E., Murphy D. C., Krzeminski W., Roth M., Rieke M. J., 1998, AJ, 116, 2475
Pogge R. S., Eskridge P. B., 1993, AJ, 106, 1405
Reynolds J.-H., 1927, Observatory, 50, 185
Romero-Gómez M., Masdemont J. J., Athanassoula E., García-Gómez C., 2006, A&A, 453, 39
Sandage A., 1962, Hubble Atlas of Galaxies. Carnegie Institution, Washington
Sandage A., Bedke J., 1994, The Carnegie Atlas of Galaxies. Carnegie Institution, Washington
Sandage A., Tammann G. A., 1981, Revised Shapley-Ames Catalogue of Bright Galaxies. Carnegie Institution, Washington
Sandage A., Freeman K. C., Stokes N. R., 1970, ApJ, 160, 831
Schlegel D. J., Finkbeiner D. P., Davis M., 1998, MNRAS, ApJ, 500, 525
Schweizer F., Whitmore B. C., Rubin V. C., 1983, AJ, 88, 909
Sheth K. et al., 2010, PASP, 122, 1397
Skrutskie M. F. et al., 1997, in Garzon F. et al., eds, The Impact of Large Scale Near IR Sky Surveys. Kluwer, Dordrecht, p. 25
Skrutskie M. F. et al., 2006, AJ, 131, 1163
Tully R. B., 1988, The Nearly Galaxy Catalog. Cambridge Univ. Press, Cambridge
van den Bergh S., 1976, ApJ, 206, 883
White S. D. M., Rees M. J., 1978, MNRAS, 183, 341
Wozniak H., Pierce M. J., 1991, A&AS, 88, 325
Wozniak H., Friedli D., Martinet L., Martin P., Bratschi P., 1995, A&AS, 111, 115

SUPPORTING INFORMATION

Additional Supporting Information may be found in the online version of this article:

Figure 5. Atlas images.

Please note: Wiley-Blackwell are not responsible for the content or functionality of any supporting materials supplied by the authors. Any queries (other than missing material) should be directed to the corresponding author for the article.

This paper has been typeset from a TEX/LATEX file prepared by the author.